

# On the plasma and electrode erosion processes in spark discharge nanoparticle generators

Ph.D. Dissertation

**Attila Kohut**

Supervisor:

**Dr. Zsolt Geretovszky**

*associate professor*



Doctoral School of Physics  
Department of Optics and Quantum Electronics  
Faculty of Science and Informatics  
University of Szeged

Szeged  
2017

# Table of contents

List of abbreviations.....	4
1. Introduction.....	5
1.1 Motivation and aims.....	5
1.2 Generation of nanoparticles.....	7
1.3 The electric spark discharge.....	11
1.3.1 Classification of gas discharges.....	11
1.3.2 Microsecond-long, atmospheric pressure oscillatory spark discharges.....	13
1.4 Spark discharge nanoparticle generation.....	16
1.4.1 General concept.....	16
1.4.2 Nanoparticles generated in the SDG.....	18
2. Experimental setup.....	24
2.1 Setup of SDGs.....	24
3. Results and discussion.....	27
3.1 Electrical properties of the spark.....	27
3.1.1 Main electrical characteristics.....	27
3.1.2 Effect of SDG control parameters.....	32
3.2 Morphology of the spark plasma.....	34
3.2.1 Experimental.....	34
3.2.2 The evolution of plasma morphology.....	34
3.2.3 Effect of the gap size on plasma morphology.....	39
3.3 Spectrally resolved optical emission of the spark plasma.....	41
3.3.1 Experimental.....	41
3.3.2 Temporally and spatially resolved emission spectrum of the spark plasma.....	42
3.3.3 Effect of control parameters on the emission spectra.....	47
3.4 OES-based diagnostics of the spark plasma.....	50
3.4.1 Methods.....	50
3.4.2 Properties of the spark plasma.....	53
3.5 Morphology of the electrode surface after sparking.....	60
3.5.1 Experimental.....	60
3.5.2 Surface of the electrodes after sparking.....	61
3.5.3 Formation of morphological features on the electrode surface.....	66
3.5.4 Energy demand of crater formation.....	70
3.6 Implications on the generated nanoparticles.....	73

3.6.1	Experimental .....	73
3.6.2	Electrode erosion.....	75
3.6.3	Particle formation.....	79
3.6.4	Effect of control parameters on the generated aggregates .....	82
4.	Summary .....	86
5.	Magyar nyelvű összefoglaló.....	89
5.1	Bevezetés .....	89
5.2	Szikrakisüléses nanorészecske generálás.....	92
5.3	Kísérleti módszerek .....	93
5.4	Eredmények.....	96
	Publications.....	99
	Acknowledgements.....	100
	References .....	101

## List of abbreviations

0D: zero-dimensional

1D: one-dimensional

2D: two-dimensional

AFM: atomic force microscopy

AMS: aerosol mass spectrometer

APM: aerosol particle mass analyzer

CLSM: confocal laser scanning microscopy

CPC: condensation particle counter

DC: direct current

DMA: differential mobility analyzer

ENP: engineered nanoparticle

FWHM: full width at half maximum

GSD: geometric standard deviation

ICCD: intensified charged-coupled device

ICP: inductively coupled plasma

LTE: local thermodynamic equilibrium

MFC: mass flow controller

NIST: National Institute of Standards and Technology

NP: nanoparticle

OES: optical emission spectroscopy

OM: optical microscopy

RF: radio frequency

SDG: spark discharge generator

SMPS: scanning mobility particle sizer

SRR: spark repetition rate

TEM: transmission electron microscopy

WD: working distance

# 1. Introduction

## 1.1 Motivation and aims

Today nanotechnology is undoubtedly one of the most important fields of science and technology. Its significance is well reflected by the fact that it probably doesn't have to be introduced. Most people have heard about "nano" as one of those mysterious things that will save and destroy humanity at the same time. As usually, reality lies somewhere between these two extremes. The ability to manipulate materials on the nanometer scale surely gave us such tools in countless fields of life that were hardly imaginable a few decades ago. The potential for targeted delivery and controlled release of drugs within the human body [1], enhancing the development of energy, food and water supply [2], the fabrication of lightweight yet strong materials [3] or the efficiency-increase of solar cells and batteries [4] are just a few examples that nanotechnology can offer. Although numerous achievements of nanotechnology and nanoscience have already reached the industrial level and hence became part of everyday life, many breakthrough applications still exist only within the walls of laboratories. Several criteria have to be met until a new technology can break out from the lab, including the supply of affordable base material. The basic building blocks of nanotechnology are the nanostructures, which can be either nanometer thick layers, nanorods or nanowires, or nanoparticles, which are usually referred to as 2D, 1D and 0D nanostructures, respectively [5]. The mass-production of such nanostructures by environmentally friendly and cheap means is a crucial technological bottleneck if nanotechnology-based product development should continue to advance. In the present work I focus on some of the fundamental aspects of spark discharge nanoparticle generation, one of the most promising techniques which are capable of producing nanoparticles (NPs) with controlled properties even on the industrial level.

NPs can be generated by several different strategies, involving chemical reactions, physical means or mechanical transformations [6]. Chemical synthesis methods are dating back to the middle of the nineteenth century and very popular due to their capability for producing NPs of various compositions with well-controlled shapes and sizes [7]. Chemical routes however always involve chemical precursors, reagents and often large amounts of solvents, which inherently increase the potential of contamination, which can be a game killer at the nanoscale, since impurities can severely alter the properties of nanostructures [8]. Physical methods offer a suitable alternative to chemical means, by exhibiting inherent advantages over competing methods, such as continuous generation, high purity of the NPs, smaller amount of waste and more straightforward scalability [9]. The most popular among physical generation techniques is flame pyrolysis, which is an established and feasible method for industrial scale production of metal-oxide particles [10], but unsuitable for the production of pure metal particles. Metal NPs are often formed by material evaporation in an inert gas followed by subsequent nucleation and condensation [11]. Evaporation can be achieved in several ways, e.g. using a

conventional furnace [12], glowing wires [13], or laser ablation [14]. These methods are, however, not energy efficient and their upscaling for mass-production is also problematic. The most energy efficient and demonstrably up-scalable method for the evaporation of conducting materials is spark discharge generation [15,16].

The spark discharge generator (SDG) has an appealingly simple layout that consists of a leak-tight chamber, housing two electrodes that are separated by a small gap. For creating a spark discharge in between the electrodes, a self-pulsed circuit is typically used, consisting of a capacitor fed by a high voltage DC power supply that is connected to the electrode gap. Each spark is initiated when the gaseous ambient in between the electrodes breaks down, i.e. via the formation of a conducting channel (spark channel) between the two electrodes. The spark plasma erodes the electrode material which results in the formation of an atomic vapor plume in the spark gap. Due to adiabatic expansion and mixing with the carrier gas the atoms cool down and eventually form nanoparticles after nucleation, condensation, coalescence and coagulation [17].

The potential of spark discharge for mass-production of NPs is only partly based on its relative simplicity. More importantly, the generation process could be easily and controllably scaled up by placing several electrode pairs in parallel at low cost and with minimal impact on the environment. In the BUONAPART-E project, 21 partners from both industry and academia worked on this upscaling approach including our research group at the Department of Optics and Quantum Electronics at the University of Szeged [16]. During the four-year collaboration with researchers from all over Europe we have investigated several fundamental aspects of spark-based nanoparticle generation and also solved numerous technical challenges along the way. Our team had the opportunity to study the fundamental processes taking place in an SDG, in particular those of which occur in the spark plasma and on the electrodes' surfaces.

Although the main principles of the SDG has been around us since the invention of the spark plug of a gasoline engine, the first use as an intentional NP generator dates to 1988 [15], when Andreas Schmidt-Ott and his colleagues published their first results. Although the design of the SDG is now commercially available [18], and used by several groups [19–25], the very fundamentals of the processes leading to particle formation is not yet fully understood. One reason for this knowledge gap lies in the difficulty of investigating the stages of the inherently multi scale nanoparticle formation process, especially its initial, early phase. Traditionally, there are two main approaches in aerosol science, through which gas-borne particles are characterized. One of this is NP collection (e.g. sampling on various substrates by using electrostatic precipitators, impactors, etc.) followed by off-line electron microscopic analysis. In the other approach, aerosol instrumentation capable of in-flight measurements is used, such as the scanning mobility particle sizer (SMPS), aerosol particle mass analyzer (APM), aerosol mass spectrometer (AMS). However, all of these apparatuses are only applicable further downstream of the spark gap, and none can acquire fundamental information in the vicinity of the primary NP formation zone. Invasive methods, such as proximity particle sampling (i.e. close to the

spark gap) have been attempted for bridging this knowledge gap [26]. However, proximity sampling always provides integrated information on the early stages of particle formation and the flow field and hence the generation process itself is altered by the sampling process. Another great challenge of the investigation of particle formation in an SDG starting from the initiation of a spark up until the formation of nano-agglomerates, lays in the multi-scale nature of the process. Particle formation takes place on the second or sub-second timescale, compared to which the duration of the spark stage (which is on the microsecond timescale) is negligible. However, each spark has a distinct temporal evolution comprising vivid physical phenomena, which affects the electrode erosion and hence the resulting NPs.

The above examples show that the structure of an SDG sets certain limits to the applicable experimental techniques. The common SDG design cannot be altered too much for the sake of experimenting on the plasma, because that would surely alter the NP formation process as well. This limits the potential measurement methods to those which are able to acquire relevant information on the processes taking place in the SDG with disturbing them the least. Keeping these constraints in mind, the core of the investigations presented in this dissertation employ non-invasive, *in situ* methods, namely temporally and spatially resolved optical emission spectroscopy (OES) and imaging, complemented with the continuous measurement of the electrical signals (i.e. voltage and current) of the discharge for gaining information on the processes preceding particle formation in the spark without disturbing the examined processes by any means. These techniques allow for the *operando* investigation of the spark plasma with a temporal resolution on the nanosecond time-scale. Optical and electrical methods are complemented with the *in situ* and *ex situ* characterization of the generated particles, and the *ex situ* characterization of the morphology of electrode surfaces subjected to sparking. These experimental techniques allowed me to address the challenge of understanding the peculiarities of the spark based NP formation process from several different viewpoints. Each method was used for gaining insight into the characteristics of the spark plasma and its effect on the electrode material. More specifically, it was aimed to describe the spark plasma, i.e. the source of NP generation, in terms of its composition, concentration, temperature, emission and morphology as a function of time, space and key control parameters. I also aimed to complement these results with investigating the electrode erosion process, including the erosion mechanisms and the role of the electrical parameters of the discharge loop. The careful selection of the above toolbox and the information acquired with them led us to the better understanding of the processes taking place in the spark, and ultimately led to a more deliberate control over the nanoparticle generation in SDGs.

## **1.2 Generation of nanoparticles**

When one needs to review all the methods through which nanoparticles can be generated, probably the most rewarding strategy could be to start with those processes in which NPs are not generated. Even if this statement is a bit of exaggeration, one can certainly state

that NPs can be produced in a great number of ways. In fact, various types of “NP generators” are constantly surrounding us in the form of gasoline engines of vehicles [27], practically any kind of combustion sources [28], constructions and demolitions or even smoking cigarettes [29], only to name a few. Moreover, independently of the anthropogenic sources, NPs have always been existed in the environment due to their natural formation mechanisms [30]. It is common in the examples mentioned above that NPs are produced unintentionally, unregulated, without control on the final physical and chemical properties. It is therefore clear that they are of minor interest in industrial or laboratory applications where NPs of well controlled properties are usually needed. For the sake of clear distinction NPs synthesized on purpose, aiming to control their composition, shape, size, surface functionality, etc. are usually called engineered nanoparticles (ENPs) [31]. ENPs can be generated via various techniques which can most generally be classified upon the direction of their synthesis route (top-down and bottom-up approaches), the medium in which the synthesis takes place (gas, liquid and solid phase processes), or the nature of the underlying mechanisms (physical, chemical, mechanical synthesis). Some aspects of classification of ENPs are shown in **Figure 1.2.1**, while their most important synthesis techniques will be discussed in the following paragraphs.

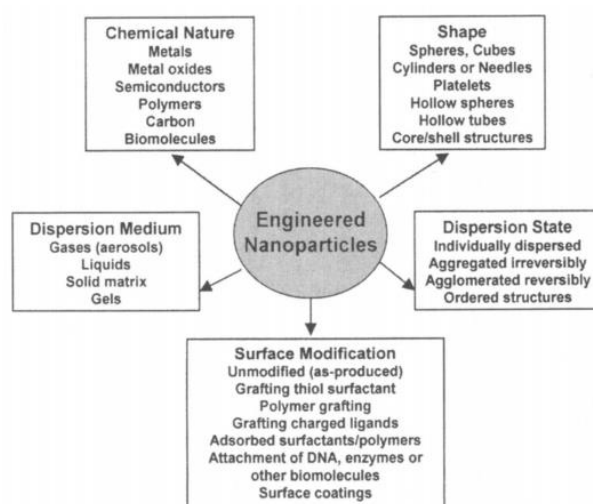


**Figure 1.2.1** Some aspects of classification of engineered nanoparticles [31].

A traditional way of producing fine particles (even in the nanometer range) is size reduction of bulk material via bead milling or grinding. It is a top-down, solid phase, mechanical method in which solid bulk precursors are grinded by beads of a defined size. The average size of the produced fine particles will be about 1/1000 the size of the beads. The smallest bead size commercially used is about 200-300  $\mu\text{m}$  which in turn means that particles of 200-300 nm diameters can be readily produced via this technique [6].

Chemical synthesis of NPs in liquids dates back to the nineteenth century, when Faraday produced metal NPs by reducing metal salts with a phosphorous and carbon disulfide mixture [32]. Since then reduction techniques are constantly evolving, using various reagents to reduce metal salts into colloids, and have become a popular bottom-up

technique for producing metal NPs. The as-synthesized particles are highly reactive and undergo oxidation or aggregate into larger particles. To prevent this, the process must be complemented by a stabilization step either during or immediately after the synthesis [7]. One example is the Brust-Schiffrin method, which makes possible the simultaneous synthesis and stabilization of metal particles [33]. Another example of the simultaneous synthesis and stabilization of NPs via the reduction method is the case of silver shown in **Figure 1.2.** [34].

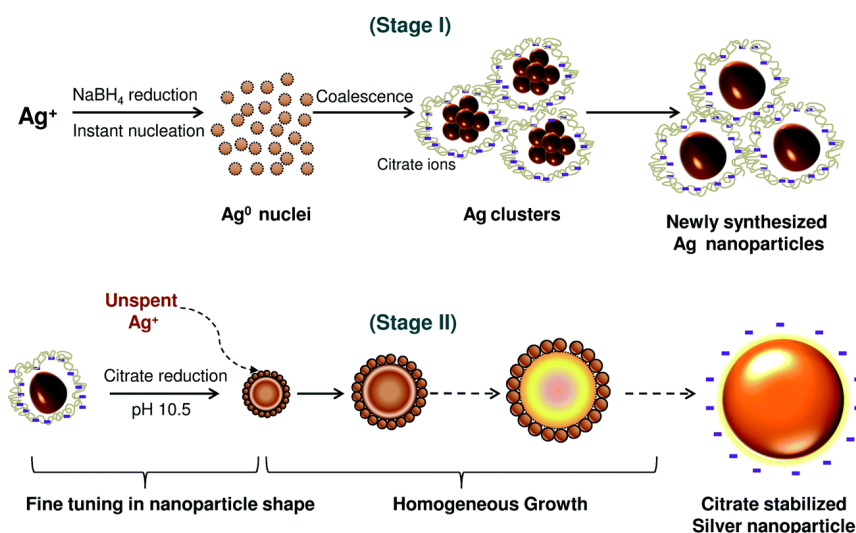


**Figure 1.2.** Example of reduction-based nanoparticle synthesis. Schematic representation of the generation of Ag nanoparticles by a co-reduction process [34].

Another widely used chemical method is the sol-gel technique. The process starts from the liquid solution of organometallic precursors, which form a new phase (sol) via hydrolysis and condensation reactions. After aging and drying a dense gel and eventually a nanopowder forms, which is especially advantageous in producing ceramic particles of high purity and uniform nanostructure at low temperature [35].

As it was exemplified above, liquid phase chemical processes involve various types of chemical precursors and reagents. Moreover, liquid routes are batch processes, which in general require the use of a large amount of solvent. This leads to a great drawback of these techniques, namely contamination. Impurities are always more abundant in liquids than in gases, while surfactants, typically used as stabilizers, also contaminate the produced particles. In contrast to this, physical methods in gases (i.e. via the aerosol route) offer the possibility of generating high purity NPs in a continuous manner with a reduced amount of waste [9]. These properties are of utmost importance when industrial scale quantities have to be produced, which is well reflected by the fact that most of the commercially available single-material NPs are produced by gas phase processes [36].

Via the aerosol route, NPs can be generated either by following top-down or bottom-up approaches (cf. **Figure 1.2.2**). A typical example for the top-down approach goes via the formation of droplets by discretization of a solution, which will crystallize to solid particles when the solvent evaporates. Droplets can be produced e.g. by nebulization, or

electrohydrodynamic atomization. NPs can also be synthesized in the gas phase along the bottom-up route, e.g. by gas-to-particle conversion via nucleation, and growth by condensation and coagulation [9]. The generated NPs are exceptionally pure, while their morphology and size can be well controlled by controlling the cooling of the vapor system [37]. NP generation techniques employing gas-to-particle conversion practically differ in the way how the material is evaporated. Vaporization can be achieved via using e.g. direct heat from combustion (e.g. flame reactors), electrical energy (such as in furnace reactors, or via glowing wire, arc and spark discharges, etc.), the energy of various plasma sources (most frequently by RF, ICP, microwave plasmas), or the energy of a laser pulse [9].

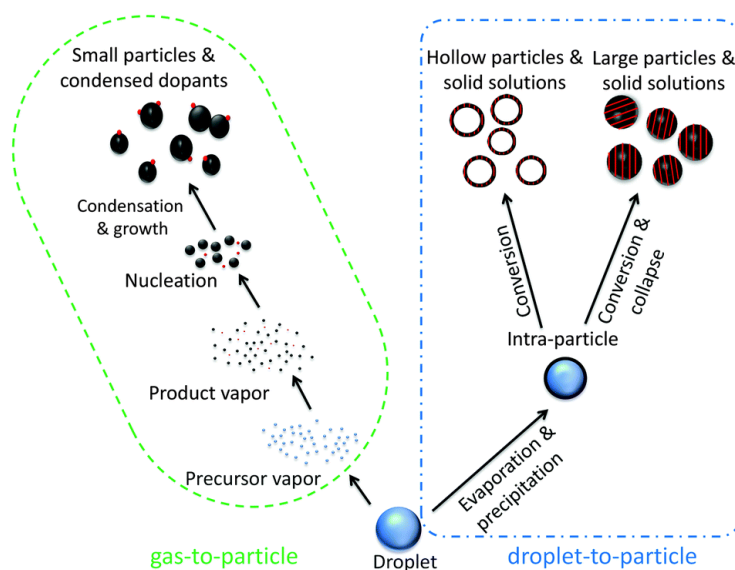


**Figure 1.2.2** Possible particle formation routes via aerosol synthesis [38].

Flame synthesis is an established technique for producing NPs in the gas phase. In fact, about 90% of the commercially available aerosol-based nanoproducts are produced in flame reactors [10]. The solid or liquid precursor material is vaporized in a combustion process (i.e. by using energy of a flame) which results in oxides, forming clusters and growing to nanoparticles. The NPs generated in flame reactors are characterized by high purity, nonporous primary particles, and small sizes with relatively narrow size distribution. Unagglomerated particles as well as multicomponent materials are difficult to produce in flame reactors [39].

Various types of precursors can be effectively vaporized by employing either cold or hot plasmas<sup>1</sup>. Highly monodisperse particles with limited yield were produced by using cold plasmas generated by microwave excitation under reduced pressure [40]. Higher production rate can be achieved with dielectric barrier discharges, also characterized by a

<sup>1</sup> Cold plasmas are characterized by higher electron temperature than the temperature of gas atoms. On the contrary, in hot plasmas local thermodynamic equilibrium exists, i.e. all species are characterized by the same temperature at a given spatial point.

cold plasma, where an electric discharge is formed between two electrodes separated by a dielectric barrier [41]. Under certain conditions, the source vapor used for particle generation was formed via sputtering in a dielectric barrier discharge [42]. Methods based on hot plasmas are usually characterized by higher particle yield as compared to cold plasmas, however the particle sizes are usually also bigger [9]. In addition, due to the higher temperature volatile precursors are not always necessary for the process. In case of inductively coupled plasmas (ICP), for instance, micron-sized solid particles can be effectively evaporated [43]. In contrast to ICP plasma sources, the electrodes are in contact with the forming plasma in case of (transferred) arc discharges. The relatively high current (some tens of amperes), characteristic to arc reactors, results in high temperature which leads to the evaporation of the electrodes or material contained in a crucible (which is a basket-shaped electrode) [44]. The process allows for the generation of a variety of pure metal particles with high yield at relatively low power input [45]. Besides the technical simplicity, an advantage of arc-based methods is that the sources of potential contaminations are limited due to the pure bulk precursors and the electrode material. The purity of the generated nanomaterials can (further) be improved, when no other material, but the electrodes, serving as precursors, and the carrier gas are present during the generation process. This scheme is realized in spark discharge NP generators (SDG) [15]. In SDGs bipolar sparks are ignited between two electrodes placed in a controlled gaseous environment, which results in the erosion of the electrode material. By employing leak-tight generator chambers and purified carrier gas, exceptionally pure particles are obtained in SDGs [46,47]. Moreover, by employing different electrode materials or alloyed electrodes, material can efficiently be mixed on the atomic scale allowing for the production of unique nanomaterials which are e.g. macroscopically immiscible [17]. Spark-based NP synthesis also has the potential for scaling up, i.e. its production rate can be increased to industrial level, which further increases the interest towards the technique [47]. The concept of spark discharge NP generation along with its main properties will be discussed in detail in the following sections, after briefly introducing the concept of electric discharges and the underlying fundamental process of electric breakdown.

### **1.3 The electric spark discharge**

#### **1.3.1 Classification of gas discharges**

Observation of gas discharges dates back to hundreds or even thousands of years, most likely starting by the admiration of lightning in the sky. We could also mention St. Elmo's fire, a phenomenon well known by sailors long ago. Delighting in a fascinating phenomenon obviously doesn't come with the understanding of the underlying processes. One of the earliest scientific explanations on the observed phenomena goes back to the 18<sup>th</sup> century, when B. Franklin experimentally proved that laboratory spark discharges and lightning have a common nature. The development of the field got a boost, when it was realized that the problem of short circuiting between the wires of high-voltage

transmission lines is related to sparks. The phenomenon was termed as the “breakdown” of the insulation of air [48]. The term “gas discharge” originates from the process of discharging a capacitor in a circuit incorporating an electrode gap filled with gas. The breakdown occurs when the voltage between the electrodes is sufficiently high, i.e. the gap becomes conductive due to the formation of ions and electrons, therefore the circuit is closed and the capacitor discharges. The term discharge can be generalized to any process when a gas is ionized by an electric field and electric current flows through this ionized gas [48].

The gas breakdown process is always initiated by charge carriers generated by cosmic rays or natural radioactivity. If an electric field is present, e.g. voltage is applied to electrodes, these electrons and ions will be pulled in the direction of the electrodes of opposing polarity and electric current starts to flow. If the voltage is increased above a certain level, the current rises drastically and light emission can be observed. These phenomena accompany the breakdown process. The basis of breakdown is the avalanche of electrons, which occurs when they can gain as much energy from the electric field as is sufficient for ionizing the gas atoms and thus producing additional electrons. The peculiarities of the electric circuit and the gas ambient determine how the discharge proceeds after breakdown. The main discharge types which can form are *glow*, *arc*, *spark*, and *corona* discharges [48]. Gas discharges result in the formation of a plasma, i.e. an ionized gas which is macroscopically neutral<sup>2</sup> [48]. It should be noted, that the term plasma – attributed to Langmuir – was introduced in connection with gas discharges. It was originally used to describe the region of a gas discharge that is not influenced by the electrodes or the walls of the discharge tube [49].

*Glow discharges* are usually produced at low pressure and characterized by relatively high voltage, low current and very weakly ionized plasma. Glow discharge plasmas are far from thermodynamic equilibrium since the electron temperature is much higher than that of the gas species. The most typical example of equilibrium gas discharge plasmas is produced by an *arc discharge*. An arc forms between two electrodes when high current is allowed to flow in the gap at relatively low voltage. At atmospheric pressure the gas temperature approx. equals to the electron temperature meaning that the arc plasma is in (local) thermodynamic equilibrium [48]. Due to the high current, arc plasma releases large thermal power which can result in the melting of the electrodes. In contrast to arc and glow, which are quasi steady, self-sustaining discharges, *sparks* are transient processes. Sparking occurs when the voltage between two electrodes reaches the breakdown voltage of the electrode gap and a conducting channel bridges the electrodes. Due to the high conductivity of the spark plasma the voltage sharply drops and the discharge ceases. This self-initiated, transient behavior is aptly described by the colloquial phrase “a spark jumps” from one electrode to another [48]. Spark formation is a complex phenomenon

---

<sup>2</sup> Strictly speaking, the following criteria have to be met for calling a macroscopically neutral, ionized gas plasma: the plasma oscillation frequency should be much higher than the frequency of particle collisions and the Debye length should be much smaller than the characteristic length of the system [49].

which can be described by different mechanisms depending on the discharge conditions. In general, at small gaps and/or low pressures (about  $<1$  cm at atmospheric pressure) the breakdown mechanism can be described by the multiplication of avalanches, or the so called Townsend mechanism. In order to explain the experimental results obtained at longer gaps and/or high pressure the theory of streamers was introduced by Loeb, Meek and Raether. The streamer is a thin ionized channel traveling through the gap, following the trace of a primary avalanche [50]. Main features of electric circuits producing either spark or arc discharges are schematically depicted in **Figure 1.3.1**.

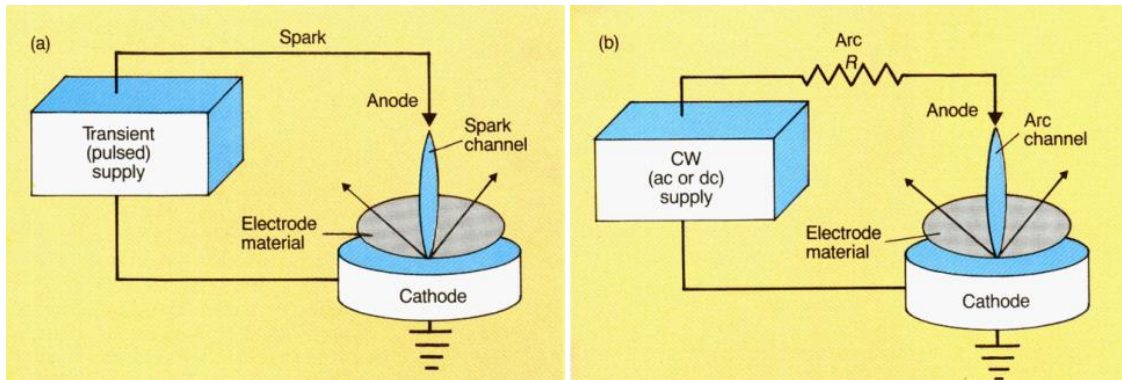


**Figure 1.3.1** Schematic representation of the electric circuits used for producing spark (a) and arc (b) discharge plasmas [51].

The characteristics of a spark discharge can be very different, depending on the properties of the discharge circuit. An important distinction between different types of sparks can be made via the presence or absence of thermodynamic equilibrium in the discharge plasma. The spark plasma can be non-thermal or thermal, depending on the types of sparks initiated. An example of spark discharges associated with non-thermal plasmas are the so called *transition sparks*. Transition sparks are produced by repetitively discharging a  $\sim$ pF capacitance in a high-resistance (in the order of megaohms) circuit, which results in a train of  $<100$  ns long sparks, far from thermodynamic equilibrium [52]. In contrast to transition sparks, which are typically characterized by small discharge gap and very short duration, sparks can also be initiated between electrodes of great distances (even in the order of meters), having considerably longer characteristic duration. These *long sparks*, however, are also considered to be non-thermal, i.e. far from thermodynamic equilibrium [49]. Spark plasmas, reaching local thermodynamic equilibrium, can also be produced. Such spark discharges can be initiated under atmospheric pressure by discharging a capacitor (with a capacitance typically in the range of 1-20 nF) in a discharge loop consisting of a small gap (typically in the order of millimeters) and having low resistance and inductance. The resulting sparks are several microsecond long, characterized by high current (in the range of hundreds of amperes), and a bipolar, oscillatory nature [53]. This type of discharges, i.e. *microsecond-long, oscillatory sparks* will be discussed in detail in the next section

### 1.3.2 Microsecond-long, atmospheric pressure oscillatory spark discharges

The wide range of applications in which electrical spark discharges are used, initiated numerous investigations aiming for describing the properties of the spark and correlating them with the (physical) processes taking place in the discharge gap (e.g. [50,54–56]). A remarkable example is spectrochemistry, in which great efforts were made towards the description of processes taking place in the so called *analytical spark discharges*. In this particular application spark plasmas are used for sampling and exciting the components of a sample to be analyzed, which was thoroughly studied by several researchers for more than one hundred years [51,57–60]. Spark discharges used for spectroanalytical purposes are produced by discharging a capacitor over an electrode gap under atmospheric pressure, connected in series with further resistive and inductive components of the electric circuit, as shown in **Figure 1.3.2**. Thus, the discharge loop can be considered to be a serial RLC circuit [53]. When the resistance and the inductance of the circuit are sufficiently small the resulting oscillatory discharge exhibits an underdamped character, exhibiting a fairly high instantaneous current. Although the exact properties of the discharge depend on the  $R$ ,  $L$  and  $C$  values of the circuit, the typical duration of these sparks are in the microsecond range. The temporal evolution of such high-current, microsecond-long sparks are generally divided into four stages: *i*) pre-breakdown, *ii*) breakdown, *iii*) arc, and *iv*) afterglow stages [53,61]. This classification assumes that the temporal starting point of the spark is the moment of application of the high voltage, provided by the capacitor, to the gap.

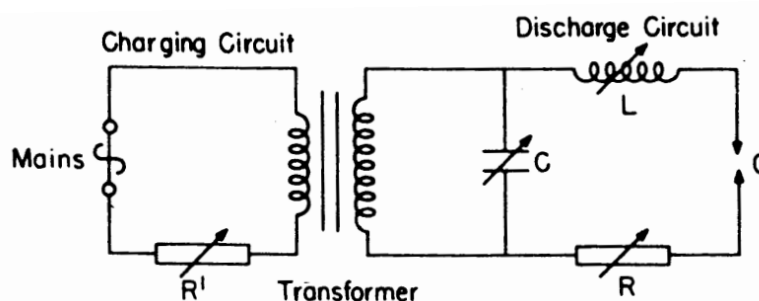


**Figure 1.3.2** Classical electric circuit of a plasma source used for spectroanalytical measurements producing microsecond-long, high current spark discharges. The capacitor ( $C$ ) is connected to the charging circuit via a transformer. The discharge takes place in the analytical spark gap ( $G$ ) as a result of discharging the capacitor via the resistance ( $R$ ) and inductance ( $L$ ) of the discharge circuit [53].

During the *pre-breakdown* stage, the electrons, emitted from the cathode or formed in the gas due to environmental ionizing radiation, gain sufficient energy to produce collisional ionization. The result is an electron avalanche and the eventual “breaking down” of the gap. If the electric field of the space charge of the primary electron avalanche is sufficiently high, a thin conducting channel (streamer) is formed, which bridges the electrodes [48]. Depending on the size of the electrode gap, the (chemical) nature of the gaseous atmosphere, the electrode configuration and a few other discharge parameters,

the breakdown can be driven by the Townsend mechanism of avalanche multiplication, and not by streamers [48]. It is hard to make a clear distinction between the pre-breakdown stage and the following *breakdown stage*, but from the point of view of light emission, both stages are characterized by the emission of the gas ambient. When sparks are initiated in air (or other molecular gas) the emission spectrum of the spark is dominated by molecular bands during the pre-breakdown stage, which is gradually replaced by the emission of ions of the gas along with intense continuous radiation [53]. The breakdown completes when a conducting channel bridges the electrodes allowing high current to flow through the gap. The temporal length of the breakdown depends on the inductance of the discharge circuit. The smaller the inductance, the shorter the duration of the breakdown [61]. The discharge enters the *arc stage* when electric current starts to flow between the electrodes, which eventually results in the erosion of the electrode material. This stage usually commences in less than 1  $\mu\text{s}$  [62]. As a consequence of the intense energy release into the gap (due to the high current), the electrode material might melt and evaporate, and the gap will no longer contain the atomic and ionic species of the ambient gas only, but also the species of the electrode material. The arc stage is characterized by concomitant light emission of the species of the gaseous ambient and the electrode material. This lasts until the electrical current ceases, i.e. a few or a few tens of microseconds, depending on the electrical parameters of the discharge loop. This stage of the spark got its name due to its resemblance to the arc discharge. Despite its transient nature local thermodynamic equilibrium (LTE) is reached in typically less than a microsecond after the onset of the breakdown in high-current, microsecond-long, atmospheric pressure spark discharges [53,63,64]. The practical consequence of this is that, similarly to arc plasmas, each temporal point of the discharge can be described by a single plasma temperature. As a result of LTE, the population of excited states follows the Boltzmann distribution, while ionization equilibria follow the Saha equation. In this respect high current, microsecond-long oscillatory sparks can be considered to be non-stationary arc discharges [53].

The emission characteristics of the arc stage of analytical spark discharges was investigated in great detail (see e.g. [57]) and peak plasma temperatures as high as 30000-40000 K have been reported [65,66], together with electron concentration in the range of  $10^{17} \text{ cm}^{-3}$  [66]. However, most of the works focusing on plasma properties (instead of the emission characteristics itself) were obtained on unipolar discharges in which the oscillatory nature of the spark is suppressed, due to its beneficial effort for analytical purposes. Bye and Scheeline have investigated the properties of analytical spark plasmas in a series of papers [64,67,68]. They reported an average electron temperature of about  $16500 \pm 450 \text{ K}$  for an analytical spark ignited between Cu and W electrodes in Ar and peak electron concentration of  $2.5 \pm 0.3 \times 10^{17} \text{ cm}^{-3}$  [64].

It is a ubiquitous observation that light emission from the gap does not cease when the electrical current terminates, but the emission from excited atoms can still be observed for a relatively long time afterwards, i.e. in the so-called *afterglow stage* [53]. The

duration of the afterglow is much longer than that of the arc stage, e.g. tens or even hundreds of microseconds long. However, since the afterglow has much less relevance from a spectroanalytical point of view, this stage has been investigated in less detail as compared to the arc stage.

As it was mentioned earlier, the thermal effect of sparking might erode the electrodes and material can be released into the gap. This process can be detrimental in some applications, e.g. in case of spark switches, but it can also be beneficial in others, e.g. in spectroanalytic measurements where electrode erosion is exploited for the vaporization of solid samples. Nanoparticle synthesis by spark discharges is another example of the latter. In addition to the formation of a plasma plume containing species of both the gas atmosphere and electrode material, particles of submicron size have been observed in the vicinity of operating spark sources [62]. Although spectrochemists attempted to use the fine particles in connection with analytical investigations [69], these observations revealed the potential of high current, microsecond-long oscillatory spark discharges in nanoparticle generation.

## 1.4 Spark discharge nanoparticle generation

### 1.4.1 General concept

Spark discharge nanoparticle generation is a bottom-up technique for producing particles in the gas phase. The principle of the technique is similar to that of the other aerosol-based methods (see Section 1.2), but now the initial atomic vapor is generated by means of an electrical spark discharge. To my best knowledge, in 1982 was the first time when the application of sparks for the purpose of nanoparticle production was reported, by Burtscher and Schmidt-Ott [70]. This was followed by a paper in 1988 by Schwyn, Garwin and Schmidt-Ott introducing the spark discharge generator (SDG), the setup consisting of the electric circuit, the discharge chamber and the gas and aerosol management (sub)systems used for assisting nanoparticle production (see **Figure 1.4.1**) [15].

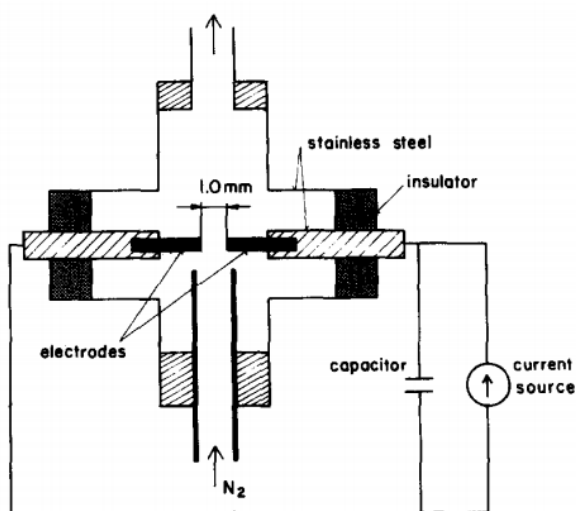


**Figure 1.4.1** Schematic view of the first spark discharge nanoparticle generator [15].

As it was briefly described in Section 1.1, the SDG has a relatively simple design that consists of a leak-tight chamber, housing two electrodes that are separated by a small gap. The electrodes serve as bulk precursors for the particle generation process, which means that the purity of the resulting nanoparticles is limited by the purity of the electrode material and that of the gas atmosphere [17]. A big advantage of the technique is its versatility. Practically any conducting material can be used as electrodes (including metals, alloys, graphite and even semiconductors) allowing for the generation of a wide range of nanoparticles in the same system [46]. It is also possible to produce multicomponent particles and nanostructures by simply using elemental electrodes of different materials, alloys or composite electrodes. It has been demonstrated that the technique allows for even creating mixed nanoparticles from macroscopically immiscible precursor materials [71].

For creating a high voltage spark discharge between the electrodes, a self-pulsed circuit is typically used, consisting of a capacitor or a capacitor bank fed by a high voltage DC power supply (together representing the charging loop), that is connected in parallel to the electrode gap (which forms the discharge loop). The process is unregulated in a sense that every spark is individually self-triggered when the voltage on the capacitor, and hence in the spark gap, reaches the instantaneous breakdown voltage of the gaseous ambient in between the electrodes [11]. Breakdown occurs via the formation of a conducting channel (spark channel) between the two electrodes in which the charge carriers are initially dominated by electrons and ions of the carrier gas. The typical discharge loop of an SDG is similar to the one that is used for spark-based analytical spectrometry. The discharge loop is characterized by low resistance and inductance, resulting in high-current, microsecond-long, oscillatory discharges similar to those described in Section 1.3.2. Therefore even if the colloquial term “single spark” implies simplicity, the process is an oscillatory event, in which the amplitude of the sinusoidal voltage and current signals is damped exponentially and even the polarity varies periodically [72].

The spark discharge nanoparticle generation technique exhibits many similarities, in terms of the produced particles, with other physical methods based on the ablation of bulk precursors. Laser ablation could be mentioned as a typical example, which was shown to produce very similar nanoparticles to that of SDGs [73,74]. The greatest advantage of the spark-based technique over the laser ablation technique is its relative technical simplicity, which also means lower investment costs. SDGs do not require the use of such expensive instruments as lasers, while capable of operating in a quasi-continuous manner (by repetitively charging and discharging the capacitor) with minimizing the produced waste [17]. Additionally, spark-based nanoparticle production is up-scalable. One way of scaling up the production rate goes via the increase of the spark repetition rate. The mass of the produced particles can be linearly increased by increasing the repetition rate of the sparks [46]. However, in the classical SDG design described above, the maximum repetition rate is limited to a few hundreds of Hz by the capacitor charging power supply. This poses a limitation to the maximum achievable particle yield. To overcome this

limitation a novel high frequency power supply was recently developed, designed for SDGs. This power supply extends the applicable spark repetition rate up to about 20 kHz [17]. Another way of scaling up the production rate is the connection and operation of multiple SDGs in parallel, which can further increase the particle yield, potentially even to meet industrial demands [75]. The increased particle concentration in the gas phase usually leads to the formation of nanoparticle aggregates and agglomerates [76], which can be undesirable in certain applications. It was already shown that by adjusting the quenching gas flow rate, spherical particles with diameter of less than 10 nm can be produced in SDGs [47]. However this also means that the higher the particle concentration the larger gas flow rates are needed to prevent aggregation. In practical applications, flow rates cannot be any high, which poses a compromise between moderate yield of small singlets and high yield of larger aggregates.

#### 1.4.2 Nanoparticles generated in the SDG

Due to the complexity of the processes taking place in SDGs, the description of the mechanisms leading to and controlling nanoparticle formation are mainly phenomenological and qualitative. Recently a simple semi-empirical analytical and a numerical model were developed which are aiming for the prediction of the size distribution of singlet particles as a function of process parameters [47,77]. In the following the main steps of particle formation in an SDG are briefly summarized together with the process parameters which were reported to affect the generated particles.

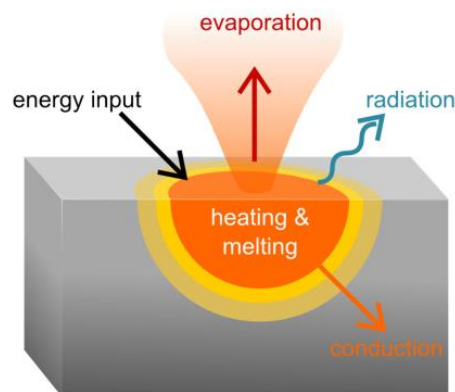


**Figure 1.4.2** Schematic representation of the simplified picture of electrode erosion, called the Jones model [24].

The initial step of particle formation in the SDG is the production of an atomic vapor by means of the erosion of the electrode material [17]. The term erosion or ablation is used partly because the exact process of material removal from the electrode is not fully explored. The surface of the electrodes are heated at the so called “hot spots” where the spark channel interacts with the electrode surfaces and hence the eroded material of the electrodes forms a vapor plume [17,24,46,78]. In addition to this, ions of the carrier gas, as well as those of the anode and the cathode bombard the electrodes that may lead to further removal of electrode material [79]. Recently, it was reported that the

experimentally determined mass-loss of the electrodes can be fairly well explained by a first principle theoretical model which takes into account evaporation only [80]. This suggests that evaporation might be the dominant mechanism of material removal. The evaporation of the electrode material in an SDG is usually described by the simple model assuming a single tiny spot created by the spark plasma channel [17,24,46,77]. By calculating the energy balance, i.e. the energy delivered to the electrode material by the spark channel is equal to the energy output represented by thermal conduction and radiation loss, the evaporated mass from such a spot can be calculated [81]; this is the so-called Jones model (cf. **Figure 1.4.2**). It turned out that when performing such an energy balance calculation there is a difference between the input and output values which can only be taken into account by the introduction of a so called energy efficiency factor, which has a remarkably low value, i.e. in the order of 0.1%. [77]. By incorporating this energy efficiency factor (as well as other experimentally determined parameters), the mass derived from the Jones model gives a reasonably good estimate of the material eroded in an SDG at varying inter-electrode distances [47] and for several electrode materials [24]. However, the highly simplified character of this approach is well reflected by the fact that the Jones model erroneously predicts the relative erosion of certain materials, e.g. gold and silver [46] and neither can explain the requirement of introducing a phenomenological factor (i.e. the energy efficiency factor), nor the origin of its very low value.

The importance of understanding how electrode erosion proceeds partly lies in the fact, that it determines the ultimate yield of the generated particles. Although not all the eroded material will turn into nanoparticles, it is safe to assume that the more material is eroded, the larger the amount of the generated nanoparticles will be. It has been demonstrated that the erosion rate can be tuned via changing the energy stored in the capacitor immediately prior to breakdown [46]. Furthermore, it is a common assumption in the SDG literature that all the energy stored in the capacitor is dissipated in the spark gap, which is well reflected by the fact that the energy stored in the capacitor is usually referred to as “energy per spark” [11,17,77]. Strictly speaking, this is of course not entirely true, as there are always resistive and other parasitic losses in the discharge loop due to imperfect connections, cables, etc., but as long as the resistance of other components in the discharge loop is negligible, as compared to the resistance of the spark gap, this estimation may be useful. I will propose a correct definition of spark energy in the Results and Discussion section and will discuss this issue further, but until then it can be certainly stated that one of the main parameters of the SDG is the spark energy [11,77].

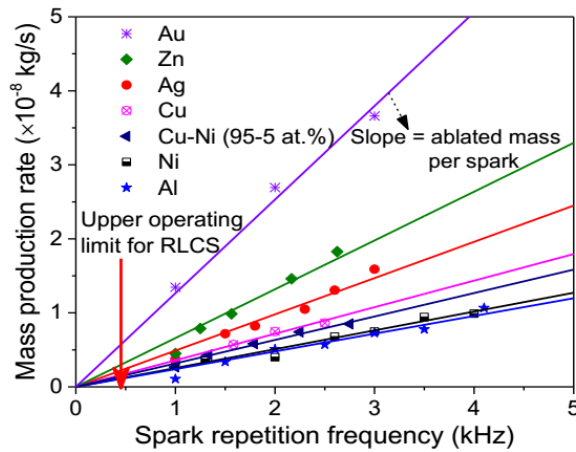


**Figure 1.4.3** Mass production rate for various electrode materials as a function of spark repetition rate in an SDG fed by a high-frequency power supply [75].

The second parameter which greatly affects the nanoparticles generated in the SDG is the spark repetition rate (SRR) [46,47]. By assuming that consecutive sparks erode the electrodes independently from each other, the total erosion rate is expected to scale linearly with the SRR [46]. This was experimentally shown for various electrode materials as shown in **Figure 1.4.3**. The SRR can only be increased up to a certain limit, after which the effect of consecutive sparks cannot be considered independent anymore. However, this limit has not been experimentally reached yet, not even with the state-of-the-art high frequency power supply operating at 20 kHz [75].

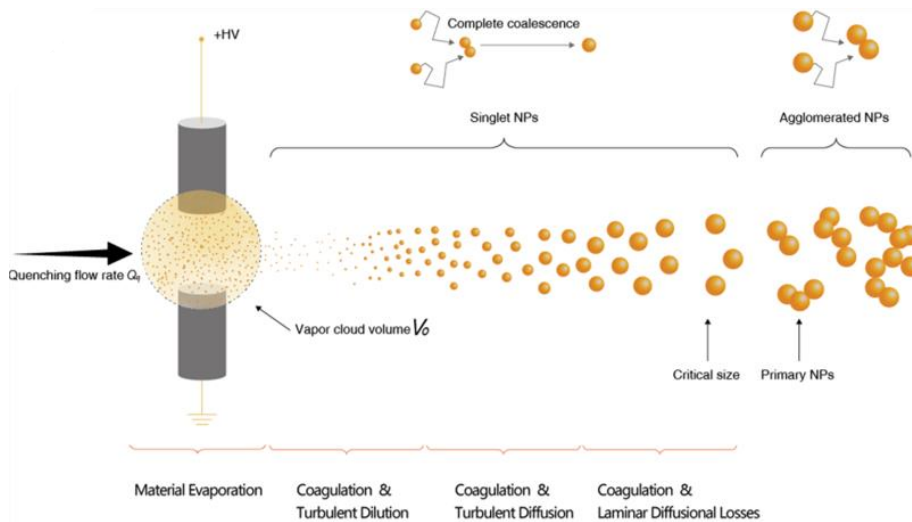


**Figure 1.4.4** Main steps of nanoparticle formation in an SDG [77].

It can be seen, that both spark energy and SRR affects the material erosion rate. While spark energy determines the mass-loss caused by a single spark, SRR sets the number of sparks in unit time and hence the total material removal rate. The eroded mass forms a hot atomic plume which is cooled down to ambient temperature by the carrier or the so called quenching gas flow [77]. This leads us to the third major process parameter of nanoparticle generation in SDGs, namely the flow rate of the (quenching) carrier gas. The

gas flow rate plays an important role in the particle formation process, since it determines the quenching of the vapor. If the quenching is sufficiently high, the vapor reaches a high supersaturation which pushes the critical nucleus size down to the atomic scale in the nucleation phase of the NP formation [77]. After nucleation the particles grow by coagulation, i.e. by particle-particle collisions and sticking. Pure particles having a size of a few nanometers are liquid-like even at low temperatures [82], which facilitates full coalescence and leads to the formation of spherical singlet particles. Full coalescence only takes place up until the particles reach a critical diameter. Nanoparticles having this critical diameter are usually called primary particles [17]. For a given material the critical diameter depends on the temperature, therefore the size of these primary particles can be controlled e.g. through the temperature of the carrier gas [77]. If conditions permit (especially when dilution of the aerosol is not sufficiently high) particle-particle collision of these primary particles will lead to the formation of fractal-like agglomerates or aggregates, which are the typical products of an SDG. The main steps of particle formation are schematically depicted in **Figure 1.4.4**.

By the proper adjustment of the three chief process parameters (i.e. the spark energy, SRR, and gas flow rate) the size of the generated particles can be controlled (cf. **Figure 1.4.5**) ranging from atomic clusters [83], through nanometer-sized spherical singlets [77] to aggregates or agglomerates above 100 nm [84].

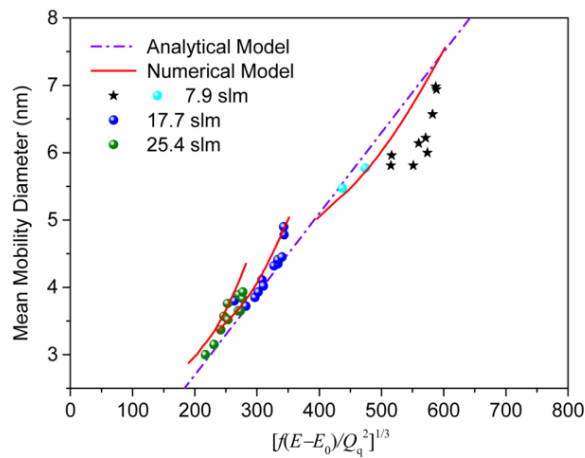


**Figure 1.4.5** Validation of the numerical and analytical models predicting the primary particle sizes generated in an SDG as a function of a parameter derived from spark energy ( $E$ ), SRR ( $f$ ) and quenching rate ( $Q_q$ ) [77].

In addition to the nanoparticles formed via the above described condensation-growth route, it was also reported that much larger, micrometer-sized particles also form in SDGs, as shown in **Figure 1.4.6c** [46,85,86]. These particles have compact, spherical shape suggesting that they form by solidification of molten droplets ejected from the electrodes' surfaces. Although these particles may form a substantial part of the total mass of the generated particles, their number is negligible as compared to the number of the nanoparticles produced [46].

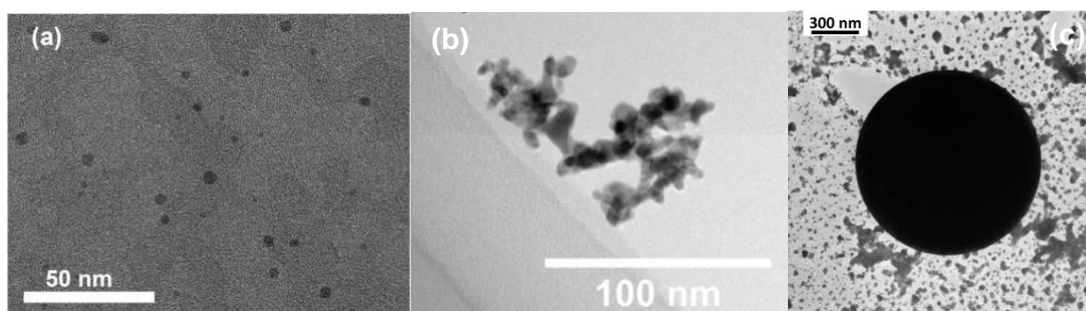


**Figure 1.4.6** **a)** Singlet [75] and **b)** aggregated gold nanoparticles [87] and **c)** a micron-sized solidified gold droplet [46] produced in an SDG.

Transmission electron microscope (TEM) images of typical singlet gold NPs and gold particle aggregates are shown in **Figure 1.4.6a-b**. Although small spherical singlet nanoparticles are proven to be produced [47,77], SDGs are typically used to generate aggregates with sizes in the range of a few tens of nanometers [24,84,87–89]. The size of the nanoparticle aggregates can trivially be controlled via the spark repetition rate, since the higher the number of sparks per second the more material will be produced, which in turn increases the aggregation, condensation or both, resulting in a size distribution with increasing modus and larger width [88]. The effect of material removal rate on the forming NPs is also apparent when electrode materials of different erosion rates are applied. As exemplified in **Figure 1.4.7** for the cases of Ag, Pd, Pt, and Au, the size distribution of the particles produced under identical conditions strongly depends on the electrode material [89]. The tendency shown in **Figure 1.4.7** can be reasonably well explained by the production rate of particles of different materials, which was 0.12, 1.68, 16.00, and 40.30  $\mu\text{g}/\text{min}$  for Ag, Pd, Pt, and Au, respectively in this particular case [89].

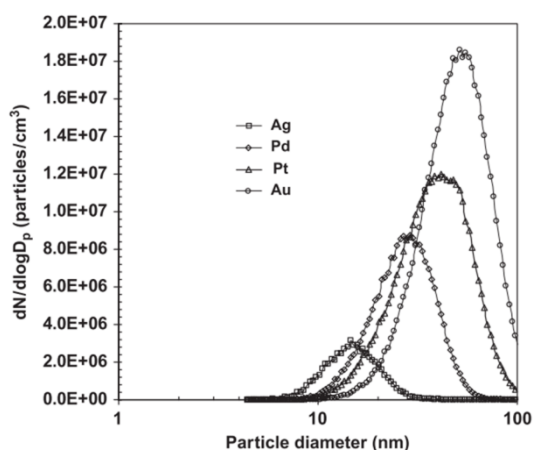


**Figure 1.4.7** Size distribution of Ag, Pd, Pt, and Au nanoparticles aggregates generated in an SDG [89].

It can also be seen in **Figure 1.4.7** that nanoparticle aggregates produced in an SDG typically have a log-normal size-distribution. The characteristic size of these aggregates is usually described either by the most frequent value of the log-normal distribution, i.e. the modal size, or by the (geometric) mean size. The geometric standard deviation (GSD) of

the particle sizes is typically used to describe the polydispersity of the produced particles [90]. The GSD of the NPs shown in **Figure 1.4.7** is in the range of 1.38-1.53 [89], illustrating that polydisperse NP aggregates are typically produced in SDGs.

As it was pointed out earlier, one way to prevent aggregation goes along increasing the flow rate of the carrier gas [46]. Moreover it was reported that the electrode geometry also has an effect on the degree of aggregation. Nanoparticles produced in pin-to-plate or wire-in-hole electrode geometries tend to aggregate much less than particles generated with the conventional rod-to-rod geometry under otherwise identical conditions [91,92]. When aggregation is prevented in an SDG – either via adjusting the gas flow rate or the electrode geometry – the produced particles will preserve their primary size that is typically below 10 nm at room temperature [47]. In several applications spherical particles with larger diameter and narrow size distribution is often desired [93]. In order to meet these demands the aerosol output of SDGs are often complemented with standard aerosol instrumentation such as differential mobility analyzers (DMA) and tube furnaces. DMAs can be used to size select particles based on their electrical mobility, while the selected aggregates can be *in situ* sintered into compact, spherical particles by means of a tube furnace [94].

Nanoparticles produced by SDGs satisfy the needs of a broad range of applications. Spark-produced NPs have already shown their strength in various fields, including solar cell research [95,96], semiconductor science [20,97], environmental research [18,98], sensors [99,100], or even in the textile industry [101]. These examples are, of course, at different technological readiness levels. Some of them are in the stage of proof of concept, like the case of catalytic studies aiming for carbon-monoxide oxidation, where SDG-produced palladium and palladium-silver nanoparticles were shown to have great potential [19,102]. While others already proceeded until small scale production: spark discharge nanoparticle generation shown to have a potential in semiconductor science. Gold seed particles have been successfully produced for the growth of semiconductor nanowires by the Aerotaxy™ method [4,20], which has already reached the production level. One could also mention the hot topic of hydrogen storage for which SDG-borne palladium and magnesium-based NPs were proved to be promising candidates [103,104]. The antibacterial effect of Ag NPs produced in an SDG and deposited onto textiles was tested recently [101]. It has been shown that, when spark-produced Ag NPs are used, an order of magnitude less Ag loading is sufficient to achieve equivalent antimicrobial effect than the NPs generated via wet routes. Moreover, an efficient, single-step, scalable method was also proposed, which could be directly integrated into textile production lines [101]. Last, but not least, certain types of SDGs are commercially available today. These generators are typically used in the field of environmental research. For atmospheric studies soot-like particles are generated by means of spark discharges in order to model e.g. air pollution [18]. The recognition of the technique in environmental studies is well reflected by the fact that SDGs are widely accepted for producing reference soot aerosol particles [105].

## 2. Experimental setup

### 2.1 Setup of SDGs

Several SDG designs exist which may differ in some technical details, but the working principle and the main building blocks are the same. Therefore, in this chapter a general description is given on the SDG setup after which I tabulate the characteristics of the actual SDGs used to obtain the results shown in the present dissertation. Details on additional particular instrumentations and techniques employed for the investigation of different aspects of SDG operation will be given at the beginning of each relevant section.

Common parts of all SDGs are the spark chamber and the electrical circuit which feeds electric power into the spark gap [11]. The spark chamber<sup>3</sup> is a stainless steel, leak-tight chamber equipped with several ports for electrical feedthroughs, gas inlet, aerosol outlet and usually have one or several windows to facilitate optical observation. The electrodes are either vertically or horizontally aligned and the gas flow which continuously flushes the inter-electrode gap can be either upward or downward directed, co-axial or crossed. The distance between the facing surfaces of the electrodes (i.e. the size of the electrode gap) can be controlled by one or more positioners. The flow rate of the carrier gas is usually set by a mass flow controller, and atmospheric pressure is kept inside the chamber.

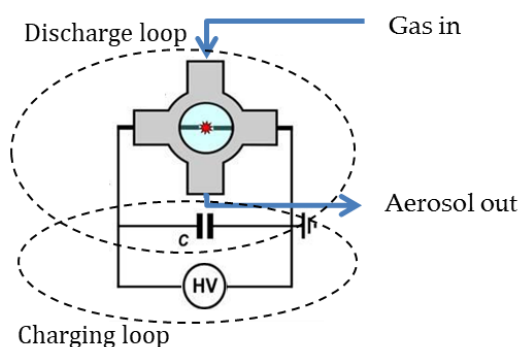


**Figure 2.1.1** Sketch of an SDG.

In my experiments the gap size was adjusted by micrometer screws typically in the range from 0.5 to 4.0 mm. The flow rate of the carrier gas was kept in the range of 1-10 l/min. All of my experiments were carried out at atmospheric pressure which was maintained by a vacuum pump and a needle valve and monitored with a pressure gauge. Cylindrical electrodes of 6.35 mm or 3.00 mm diameter were used in two electrode geometries: flat-end and tipped-end (with a 30° apex angle). In the flat-end geometry, electrode erosion is distributed over a larger area (i.e. the entire front surface of the electrode rods), while on tipped-end electrodes erosion is concentrated around the

---

<sup>3</sup> The chamber geometry used in most of my experiments has been developed for the purposes of the BUONAPART-E project, supported by the 7th Framework Programme of the European Union, specifically optimized for NP production purposes, and was manufactured by Pfeiffer Vacuum GmbH.

electrode tips. Since high throughput of generated NPs needs substantial electrode erosion the flat-end geometry is preferred in SDGs. However, with this electrode geometry, the wandering of consecutive sparks over the electrode surface poses challenges to optical measurements, and even the electrical data are less stable due to the positional variation of the surface quality and the concomitant differences in the breakdown voltage. Hence results obtained with tipped-end electrodes provide more reliable information, and more fundamental insight, while observations obtained with flat-end electrodes have more direct relevance to NP production. Therefore, tipped-end electrodes were used in those measurements where high positional stability was required, and in experiments focusing on electrode erosion and NP generation flat-end electrodes were employed.

Energy is fed into the spark gap by a simple capacitor charging circuit. A monolithic capacitor or a capacitor bank (jointly referred to as capacitor in the rest of the text) with a total capacitance in the nF range is charged by a high voltage capacitor-charging power supply to a maximum voltage of typically about 10 kV using a charging current of a few or a few tens of milliamperes. Since the capacitor and the electrode gap are connected in series (**Figure 2.1.1**), the discharge of the capacitor across the spark gap will commence when the voltage on the capacitor reaches the breakdown voltage of the spark gap. The resulting spark discharge is a bipolar, oscillatory discharge, the damping and the oscillation frequency of which is jointly set by the total capacitance, resistance and inductance of the discharge loop. The discharge of the capacitor via the spark gap is accompanied by the recharging of the capacitor by the charging power supply ("self-pulsed, free running mode"), but since the current in the charging loop is many orders of magnitude smaller than the current in the discharge loop (which is typically a few hundreds of amperes), the two processes can be considered to be practically independent. The repetition of sparking is described by the spark repetition rate, SRR, that can be controlled by changing the charging current and the gap size (via the breakdown voltage), assuming that all other experimental conditions are kept constant.

The main parameters of the different generator setups used in my experiments are tabulated in **Table 2.1**. The names given in **Table 2.1** will be used to refer to a particular SDG later in the text.

**Table 2.1** Main parameters of the SDGs used in my experiments.

Name	<b>SDG A</b>	<b>SDG B</b>	<b>SDG C</b>	<b>SDG D</b>
Capacitance (nF)	8	29	20	15
Power supply	FuG HCK 800-12500	Technix CCR10-P-750	Technix CCR15-P-150	Technix CCR20-N-300
Carrier gas	Ar, N <sub>2</sub>	N <sub>2</sub>	Ar, N <sub>2</sub>	N <sub>2</sub>
Flow geometry	Crossed	Co-axial	Crossed	Crossed
Gas flow rate (slm)	5	1.68	5	2
Electrode diameter (mm)	3	6.35	3	3
Electrode position	Horizontal	Vertical	Horizontal	Horizontal
Electrode tip geometry	Tipped, flat	Tipped, flat	Flat	Flat

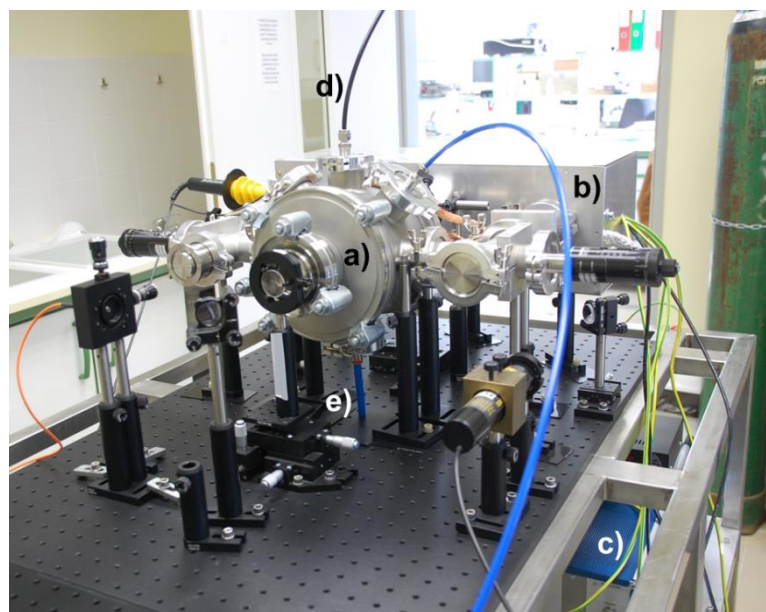


**Figure 2.1.2** Photograph of the SDG A system. The letters indicate the following parts: a) discharge chamber, b) shielding box containing the capacitor, c) high-voltage capacitor charger power supply, d) carrier gas inlet, e) aerosol outlet.

As an illustration, **Figure 2.1.2** shows the core of the SDG A system (without showing the additional instrumentation for e.g. emission spectroscopy, imaging, nanoparticle deposition, or in-flight nanoparticle characterization), which was developed and built in our laboratory. The peculiarity of this particular setup is to facilitate fundamental studies during the normal operation of the generator in a well-controlled manner.

### 3. Results and discussion

#### 3.1 Electrical properties of the spark

##### 3.1.1 Main electrical characteristics

In a typical, unregulated or free-running SDG an oscillatory discharge forms after the breakdown occurs between the electrodes (see Section 2.1). **Figure 3.1.1** exemplifies the typical voltage and current waveforms measured in SDG B with a high voltage probe (Model N2771B, Agilent, 50 MHz) and a calibrated current probe (Model 110, Pearsons, 20 MHz), respectively. The under-damped character of the oscillations is immediately obvious. As it can be seen, the voltage drops abruptly after the breakdown and then it oscillates with an exponentially decaying amplitude, while the current rises fast and oscillates in a similar manner, but with a certain phase shift with respect to the voltage signal. Under the conditions of the discharge shown in **Figure 3.1.1**, decay time (defined as the square of the inverse of the damping coefficient of the current or voltage oscillations) of  $\sim 15 \mu\text{s}$  can be observed. The breakdown voltage is about 5.5 kV and the current peaks at about 300 A. This relatively high peak current is the consequence of the high capacitance, low resistivity and low inductance of the circuit, which are essential for the efficient erosion of the electrodes, when NP production is targeted.

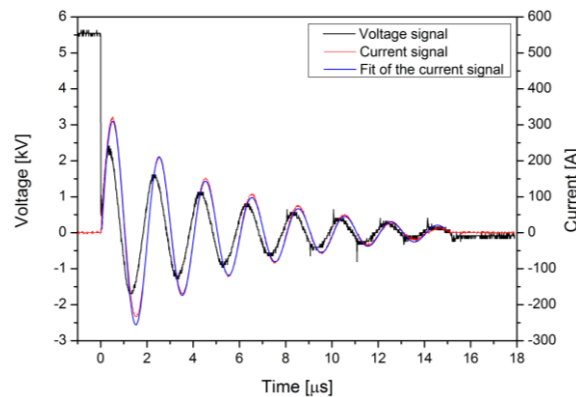


**Figure 3.1.1** Voltage (black), and measured (red) and fitted (blue) current signals for a spark ignited between Cu electrodes, placed 3 mm apart (SDG B).

As the simplest approximation, the discharge loop can be represented as a series RLC circuit [46]. Let's assume that the spark channel is electrically well described by a resistor, which together with the resistances in the discharge circuit represent the total resistance,  $R$  of the system. This resistance is considered to be connected in series with the rest of the discharge circuit, characterized by an equivalent inductance,  $L$  and a capacitance,  $C$  which is determined by the capacitor). Due to the underdamped behavior of the system (c.f. **Figure 3.1.1**) the  $R < 2 \left( \frac{L}{C} \right)^{0.5}$  criterion is held, and the current waveform can be described by the following equation [106]:

$$I(t) = I_0 e^{-\frac{t}{\tau}} \cos(\omega t + \varphi_0) \quad (3.1.1)$$

where

$$\tau = \frac{2L}{R} \quad \text{and} \quad \omega = \sqrt{\frac{1}{LC} - \left(\frac{R}{2L}\right)^2}$$

We estimate the total resistance and inductance of the system by fitting this  $I(t)$  function to the measured current waveforms (see **Figure 3.1.1**). In the particular case shown in **Figure 3.1.1** this fitting procedure resulted in a resistance,  $R$  of ca.  $1.30 \, \Omega$  and inductance,  $L$  of  $3.6 \, \mu\text{H}$ .

It is expected and also documented in the literature [55] that the resistance of a spark discharge changes rapidly during its pre-breakdown and breakdown stages, i.e. prior to the complete breakdown of the gas, due to the coupled effect of the varying electron density and gas temperature. It should be noted though, that my electrical measurements reported in the present dissertation were done after a conducting channel connects the two electrodes, i.e. during the arc stage, in which the spark behaves similar to an arc discharge [53]. Since the resistance of a pulsed arc also changes slightly [107], we attempted to elucidate the time dependence of  $R$  and  $L$  by fitting portions of the entire underdamped oscillations and also by using time-dependent  $R$  and  $L$  values in the fitting process. On one hand, we have not seen systematic variation of these fit parameters within the investigated time range. On the other hand, the above simple electrical model, with its assumption of a constant resistance and inductance, fits neatly the measured current waveforms, which is in accordance with the findings of Greason [108].

It was reported that the spark discharge have an inductive component on the order of  $10 \, \text{nH}$  [109]. Since this value is more than 2 orders of magnitude lower than the total inductance of our discharge circuit, the inductance of the discharge gap can be neglected with respect to the total inductance of the rest of the discharge circuit. More complete electrical models take into account the capacitance of the electrodes and the inductance of the plasma, along with the capacitance, resistance and inductance of the used probes [52]. However, as it was mentioned before, the large capacitance of the capacitor bank and the large inductance of the cables with respect to those of the spark justify our above presented simplifications during the high current conductive (i.e. arc) stage of the spark discharge.

As it was mentioned before, the total resistance of the circuit is the sum of the resistive components of the discharge loop and the resistance of the spark plasma. It is not straightforward to separate these components and measure or calculate the resistance of the spark only. In certain cases, the resistance of the discharge loop can be experimentally determined [110], which however requires the modification of the electrical circuit, in a way not feasible when a common SDG is used.

There is a consensus in the literature of SDGs that there are two main process parameters which affect the NP output of the generator and defined by the electrical circuit: *i*) the spark energy and *ii*) the spark repetition rate (SRR) [17,46,77,84]. The spark energy is the energy dissipated in the electrode gap and hence the one that promotes the material erosion process. In the literature of spark-based NP generation, this quantity is assumed to be equal to the energy stored in the capacitor prior to breakdown (see e.g. the most recent review by Pfeiffer *et al* [17]):

$$E_{stored} = \frac{1}{2} C U_{bd}^2 \quad (3.1.2)$$

where  $C$  is the capacitance and  $U_{bd}$  is the breakdown voltage. The inherent problem with the above definition is that it assumes that all the energy stored in the capacitor is dissipated in the gap without any losses in the discharge circuit. It is immediately clear, that in general this simplification cannot be true due to e.g. parasitic losses, radiation losses or incomplete discharge of the capacitor. A more realistic approach could be the calculation of the spark energy from the instantaneous current,  $I(t)$  measured in the discharge loop. For this, one can use the instantaneous power, defined as

$$P(t) = U(t)I(t) = I^2(t)R_{spark} \quad (3.1.3)$$

and integrate it over time:

$$E(w) = \int_0^w P(t)dt = R_{spark} \int_0^w I^2(t)dt \quad (3.1.4)$$

where  $R_{spark}$  is the resistance of the spark channel and  $w$  sets the time until which one is interested in the energy dissipated in the spark gap. If  $w = \frac{1}{SRR}$  one may obtain the total time-integrated energy of a single spark, or *spark energy* for short. As it was mentioned earlier, the determination of  $R_{spark}$  is challenging in a traditional SDG setup, the one also used here, without the significant modification of the discharge chamber and the spark gap. Therefore, as a first approximation I assume that the resistance of the discharge loop is negligible as compared to the resistance of the spark itself, meaning that  $R_{spark} \approx R$ . This assumption can be justified by comparing the  $R$  values obtained from **Equation 3.1.1** with typical  $R_{spark}$  values estimated from theoretical models. Different time dependent calculations of the arc's electrical resistance, based on the temporal evolution of the current, can be found in the scientific literature [107]. Due to the similarity of the spark discharge to an electric arc in the time domain under study, these models can be used to estimate  $R_{spark}$ . I took the expression given in [111] (based on a model developed by Rompe and Weizel) as an example and the one calculated by Barannik *et al* [107]. Although these expressions were meant for unipolar current peaks with higher intensity (up to several kiloamps), one can use them to estimate the resistance at the first peak of the current waveform ( $\sim 0.5 \mu s$ ). These expressions give resistances in the range of 0.9-1.3  $\Omega$  [111] and 1.3-1.9  $\Omega$  [107] for the conditions studied here. The  $R$  values derived from the current waveform measured in the SDG under the same conditions are found to be in the range of 1.30  $\Omega$ -1.65  $\Omega$ . These values match fairly well the resistances estimated from the theoretical models, meaning that the assumption of  $R_{spark} \approx R$  is justified under the present conditions.

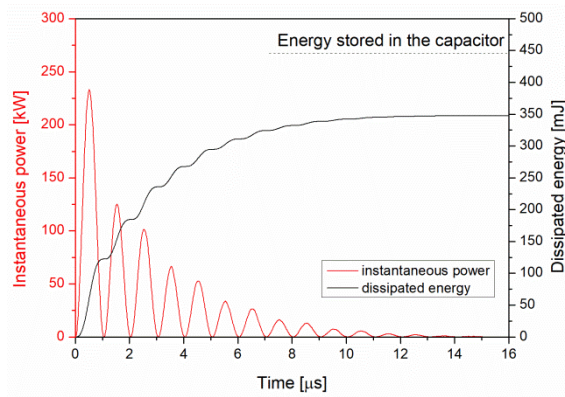


**Figure 3.1.2** The instantaneous power (red) and the dissipated energy (black) in the spark gap, calculated from the  $I(t)$  waveform (SDG B).

The instantaneous power and the temporal evolution of the dissipated energy calculated from **Equations 3.1.3 and 3.1.4**, respectively are shown in **Figure 3.1.2**. As can be seen the total dissipated energy is lower than the energy stored in the capacitor, which might be due to the above mentioned effects outside the spark gap, like parasitic losses in the discharge circuit or the energy needed to ionize the gas atoms forming the channel. It is also possible that the capacitor bank is not fully discharged during the spark, or some energy is dissipated in the spark gap during the post discharge phase. I have also calculated the energy dissipated in the gap from the current waveforms measured at different gap sizes by using **Equation 3.1.4**. For the range of experimental settings used, the spark energy calculation resulted in an average value of about 80% of the stored energy. The scatter of the obtained values is within the uncertainty of the applied method, so the ratio between the energy dissipated in the gap and stored in the capacitor can be considered to be constant for a given SDG setup. The approx. constant ratio between the stored energy and the dissipated energy explains the experimental evidence that the variation of the stored energy describes reasonably well the variation of the material erosion in a given SDG [46].

For gaining a better understanding of spark energy, one needs to investigate a more general case i.e. when the resistance of the discharge loop is not negligible.

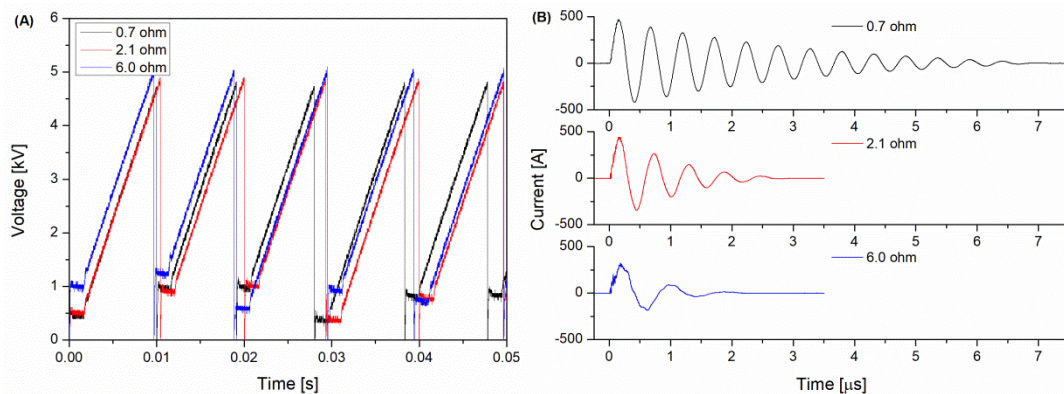


**Figure 3.1.2** Voltage (A) and current (B) measured in an SDG having different total resistances (SDG A).

**Figure 3.1.2A** shows three voltage waveforms measured in an SDG having different total resistances. It is clearly discernible that the total resistance of the discharge loop does not affect the breakdown voltage and hence the stored energy as calculated from **Equation 3.1.2**. In contrast, a remarkable effect can be seen on the corresponding current waveforms (**Figure 3.1.2B**). The damping factor of the current oscillations strongly increases with increasing resistance resulting in a decrease of total duration of the current ceases to zero. At a total resistance of  $6\ \Omega$  only approx. one full cycle is observable. Concomitantly, the peak current also decreases. It has to be noted that the frequency of the oscillations also slightly changes, which is due to the fact that the inductance slightly increases with increasing resistance. The results shown in **Figure 3.1.2** are perfectly in line with the well-known peculiarities of series RLC circuits [106]. However, these results have important consequences on SDGs. First, one can conclude that in general the instantaneous current should be used to derive the spark energy, instead of the breakdown voltage traditionally used in the literature. The circumstance that hinders to use the measured current and **Equation 3.1.4** for calculating the spark energy is the lack of knowledge on the spark resistance. It is obvious that the resistance of the discharge loop cannot be neglected when a rigorous analysis of the spark energy is performed. Nonetheless, as it will be shown later, the integral of the square of the instantaneous current is sufficient to describe the processes taking place in the spark discharge ignited in an SDG.

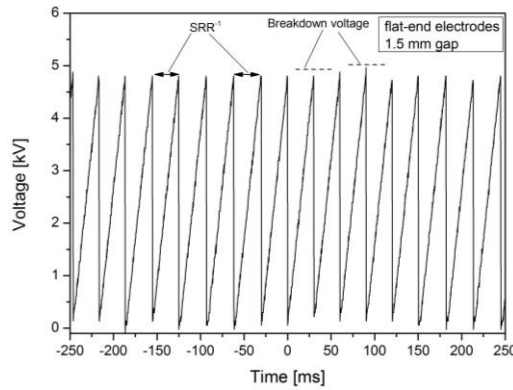


**Figure 3.1.3** Voltage signal measured for consecutive spark events recorded between electrodes at 1.5 mm apart. The peak values represent the breakdown voltage for the given spark. The inverse of the duration between consecutive peaks gives the repetition rate of the sparks, i.e. the SRR (SDG B).

Besides spark energy, the other important process parameter of SDGs which is set by the electric circuit is the spark repetition rate (SRR). The SRR is determined by the current charging the capacitor,  $I_{ch}$  which will be denoted as charging current, the capacitance,  $C$ , and the breakdown voltage,  $U_{bd}$  as described by **Equation 3.1.5** [46]:

$$SRR = \frac{I_{ch}}{CU_{bd}}. \quad (3.1.5)$$

A typical high voltage waveform acquired on repetitive spark events is shown in **Figure 3.1.3**. The charging current defines the slope of the charging cycles (the sloping lines on the oscilloscope trace), while the breakdown voltage sets the end of charging

which is followed by the fast discharge of the capacitor (apparently vertical lines in the trace). It is obvious that the variation of both the charging current and the breakdown voltage affects the duration of charging-discharging cycles, i.e. the repetition rate of the sparks. As can be seen in **Figure 3.1.3** the typical scatter in the breakdown voltage is small which results in only a minor uncertainty in the SRR.

### 3.1.2 Effect of SDG control parameters

It was pointed out in the previous section that the most important process parameters of the SDG which depend on the electric circuit are the spark energy (or energy per spark) and the SRR. Although these parameters can effectively be tuned by adjusting the  $R$ ,  $L$  and  $C$  components of the discharge and the charging loop it is not realistic to vary these parameters during the routine operation of a nanoparticle generator. Therefore more practical parameters are needed which can be used to vary the SRR and the spark energy thereby tuning the output of the SDG. These experimentally easily accessible parameters will be called *control parameters*. The main control parameters affecting the spark energy and SRR are the distance between the electrodes (i.e. gap size) and the charging current.

At a constant pressure and electrode geometry the breakdown voltage predominantly depends on the gap size, hence it can be used to vary the energy stored in the capacitor according to **Equation 3.1.2**. At a fixed gap, the SRR can be varied by changing the charging current, as follows from **Equation 3.1.5**. In the following, the effect of the gap size and the charging current will be shown on the breakdown voltage, stored energy and SRR.

The variation of the measured breakdown voltage as a function of the gap size as well as the charging current measured during sparking between Cu electrodes is shown in **Figure 3.1.4A**.

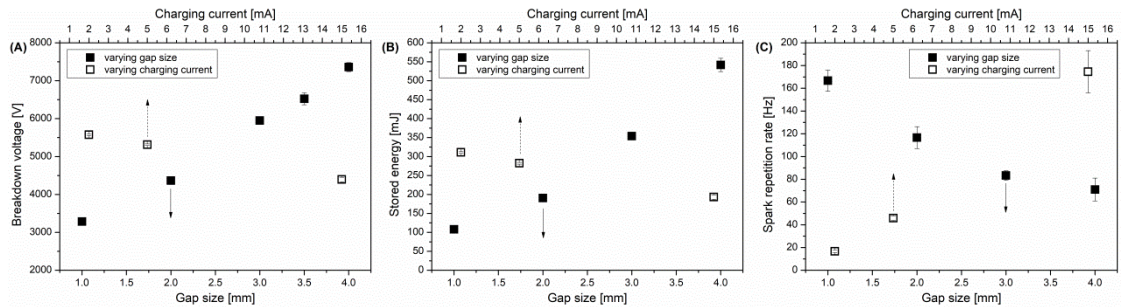


**Figure 3.1.4** The variation of the breakdown voltage (A), energy stored in the capacitor (B), and spark repetition rate (C) as a function of gap size at 10 mA charging current and as a function of the charging current at 2 mm gap in case of Cu electrodes in nitrogen atmosphere (SDG C).

As can be seen in **Figure 3.1.4A**, the breakdown voltage increases linearly with the increase of the gap size in qualitative agreement with Paschen's law [112]. The increasing charging current and the concomitantly increasing SRR results in a linearly decreasing breakdown voltage. This tendency (which is common for all the SDGs used in my experiments) cannot be explained solely by the electrical properties of the discharge loop. This is most probably due to the fact that charge carriers are left behind by the preceding

spark and accumulated in the gap thereby somewhat lowering the breakdown voltage as compared to the single spark or quasi single spark cases [113].

The energy stored in the capacitor calculated from the breakdown voltage using **Equation 3.1.2** and the measured SRR are shown in **Figure 3.1.4B** and **C**, respectively, as a function of the gap size and the charging current. The stored energy is directly determined by the variation of the breakdown voltage (**Figure 3.1.4A**) according to **Equation 3.1.5**, which therefore increases with the increase of the gap size in a quadratic manner and decreases with the increase of the charging current (**Figure 3.1.4B**). The SRR however decreases with increasing gap size and increases quasi linearly with an increasing charging current, as dictated by **Equation 3.1.5**.

It has to be noted that the effect of control parameters on the energy stored in the capacitor was shown here instead of the more precise spark energy. This has practical reasons, since as it was pointed out in the previous section the stored and the spark energy differ only by a constant factor when an SDG of fixed circuit parameters is used. Therefore in a given SDG setup the variation of the spark energy as a function of the control parameters will be the same as that of the stored energy. This proportional relationship will also be relied upon later when the effect of control parameters on other characteristics of the SDG is examined.

It should also be noted that the trends shown in **Figure 3.1.4** were found to be universal, i.e. hold for various electrode materials and carrier gases in all the SDGs I used.

## 3.2 Morphology of the spark plasma

### 3.2.1 Experimental

Time-resolved images of the spark produced in SDG B were recorded using a high sensitivity, ns-gated intensified CCD (ICCD) camera (Model iStar-734 Gen 2 (W-AGT-03, Andor), with a photographic lens system (WD=200 mm) attached to it (**Figure 3.2.1**). For triggering the ICCD camera, the falling edge of the voltage signal measured by a high voltage probe (Model N2771B, Agilent, 50 MHz) was used. Due to the insertion delay of the camera and the delay caused by signal propagation, the minimum total delay for recording imaging data was 50 ns. In order to study the time evolution of the spark, images of the discharge were taken at time delays varying from 50 ns to a few ms. The gate width of the camera was progressively increased from 5 ns to 100  $\mu$ s in order to compensate for the decreasing emitted light intensity at longer delay times. Correction for different gate widths, amplification, and background was carried out by post-processing the images using a MATLAB code. The general conditions, such as gap size, spark repetition rate, breakdown voltage were kept constant. The sensitivity of the camera and the transmission curve of the photographic lens allowed for recording light intensity data integrated in the 200-850 nm wavelength range.

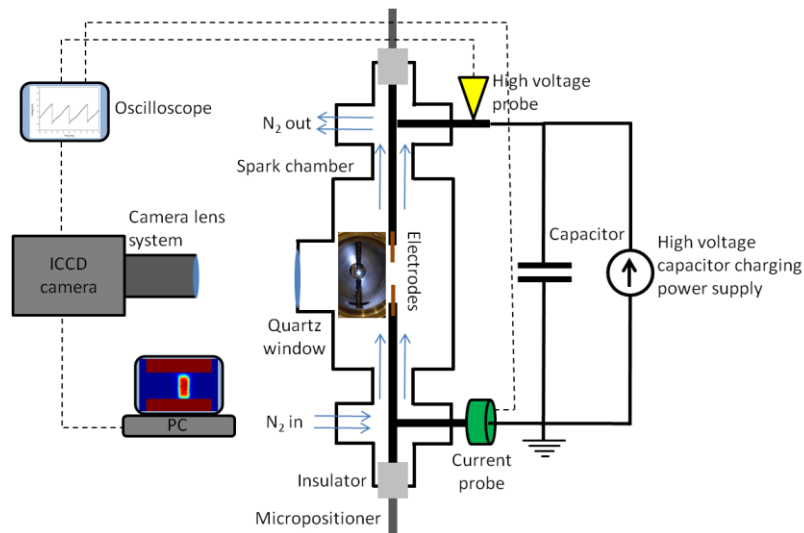


**Figure 3.2.1** Schematic view of the experimental setup used for studying the plasma morphology (SDG B).

### 3.2.2 The evolution of plasma morphology

Fast imaging is a reliable tool for studying the breakdown in gases under different conditions [52,114–118]. Most of the discharge imaging studies published in the scientific literature either focus on streamer formation and propagation, or analyze globally the different discharge regimes such as glow, corona or spark. In the present section the results on how the shape and intensity of the spark channel evolves once it is formed in the SDG will be summarized. The temporal evolution of plasma morphology, i.e. the size, shape and intensity distribution as well as the position were followed from 50 ns up until a few tens of microseconds, i.e. covering the entire arc and the majority of afterglow stages of the spark (see Section 1.3.2).

Snapshots shown in **Figure 3.2.2** illustrate the evolution of spark morphology over time. Please note that every image shown in **Figure 3.2.2** was normalized in intensity, in order to make the shape of the discharge discernible also at longer delays, when the emitted intensity is very weak, i.e. much weaker than at the beginning of the arc stage. The images prove that the discharge starts as a thin and intense approx. cylindrical channel between the two tipped electrodes. As more power is dissipated, the channel diameter as well as the integrated intensity of emission increases, as will be shown later in **Figure 3.2.3**. After about 500 ns, the channel starts to partially lose its cylindrical shape but it is still relatively well confined as a quasi-cylindrical volume between the two electrode tips. By about 10  $\mu$ s, when the current oscillations and consequently the energy input cease (the discharge reaches the end of the arc stage by definition), the discharge spreads (out) greatly and loses its cylindrical shape almost completely. After this point, i.e. in the afterglow the decaying plasma expands in 3D and gradually fades away.

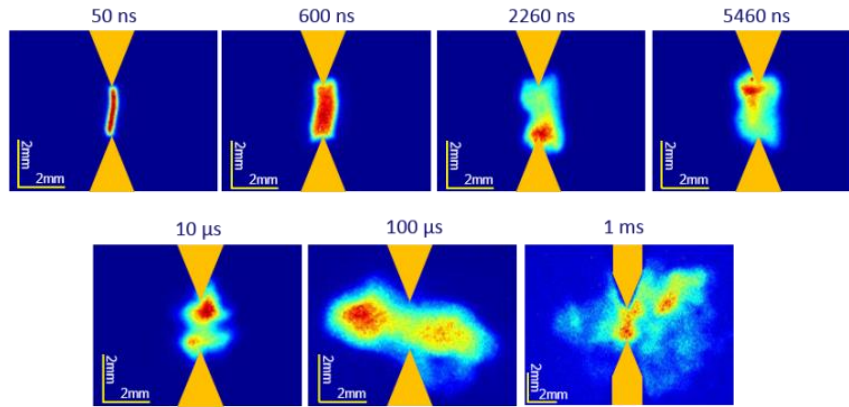


**Figure 3.2.2** Images acquired at different delays for spark discharges between tipped-end electrodes placed at 2 mm distance in 10 l/min of co-axial  $N_2$  flow. The top electrode was initially the anode (SDG B).

It must be clarified again that due to the intensity rescaling, the images presented in **Figure 3.2.2** are meant to visualize the shape and the expansion of the emitting vapor and the temporal evolution. In order to compare the intensity of each image all the light collected in one frame is integrated and normalized for different exposure times, i.e. gate width. In **Figure 3.2.3A**, the total light intensity collected is shown as a function of delay time. The intensity curve was normalized to its maximum. The figure shows how the total light intensity of the spark rises during the first half microsecond and then it decays quasi-exponentially until a few tens of microseconds (please note the logarithmic scale of the horizontal axis in **Figure 3.2.3A**). After about 50  $\mu s$ , the decaying trend changes to a less steep one. The total light intensity exhibits oscillations in the 1-10  $\mu s$  time window. **Figure 3.2.3B** shows that these oscillations follow neatly the oscillations of the instantaneous power. It must be noted that the instantaneous power is calculated according to **Equation 3.3** where the equivalent resistance of the spark gap was estimated to be 1.4  $\Omega$  for SDG B.

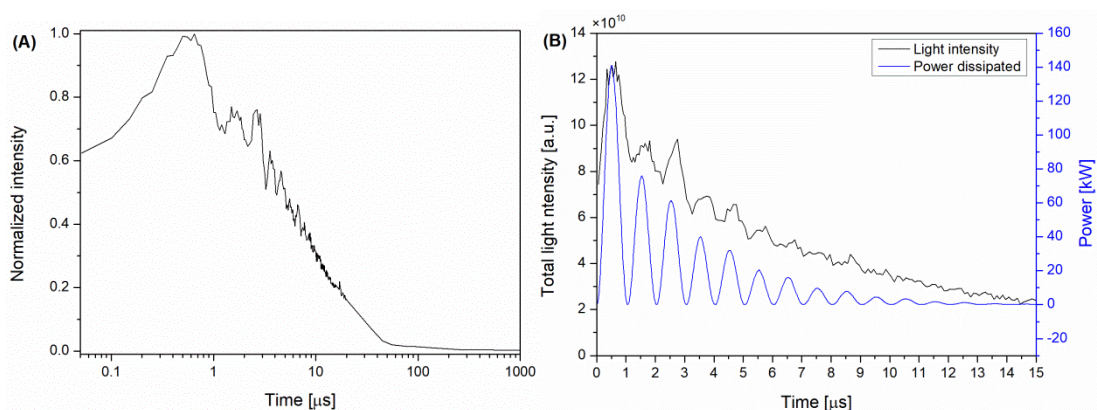


**Figure 3.2.3** (A) Total light intensity collected for spark discharges between tipped-end electrodes 2 mm apart. (B) Total light intensity collected (black line) compared to instantaneous power (blue line) at a gap size of 3 mm (SDG B).

The snapshots shown in **Figure 3.2.2** exhibit another striking feature of the spark plasma. The plasma not only changes in intensity and shape over time, but several recorded snapshots also reveal an uneven intensity distribution along the axis of the electrodes. For example, in the particular frames shown in **Figure 3.2.2**, there is a "plasma hot spot" (i.e. a spot with distinctively more intense emission) in front of the lower electrode at 2260 ns, then in front of the upper electrode at 5460 ns, and in front of the upper electrode again at 10  $\mu$ s. Note that the existence of such a hot spot does not mean that the discharge would not fill the entire gap. **Figure 3.2.4** shows how the position of this plasma hot spot oscillates over time and how its oscillation correlates with the current waveform. As is known (cf. Section 3.1.1, **Figure 3.1.1**), the current exhibits an oscillatory behavior, meaning that the electrode polarity alternates typically less than 20 times in the 0-20  $\mu$ s temporal window in the present case, i.e. the polarity of the electrodes reverses several times during the lifetime of the spark. It can also be seen that the displacement of the plasma hot spot with respect to the center position of the spark gap becomes smaller as time passes, i.e. reflecting the decreasing strength of the electric field. Please note, that these findings hold for every other experimental parameters (e.g. gap sizes, flow rates, etc.), and the data shown in **Figure 3.2.4** only exemplifies the tendencies on the case of tipped electrodes placed 3 mm apart.

Data in **Figure 3.2.4** proves that the plasma hot spot is always situated close to the temporary negative electrode (cathode) and the position of the most luminous part of the discharge follows the current signal with some delay. The axial structure of the discharge channel at every moment seems to be similar to that of a glow discharge [119] or a DC continuous arc as defined by Boumans [53]. Close to the (momentary) negative electrode, a region with non-zero charge, known as the "cathode fall", forms in the gap which effectively shields the electric field. When moving beyond the cathode fall region, i.e. a bit further towards the anode, the plasma tends to be more intense in emission due to the dissipation of a substantial amount of energy gained by the electrons in the fall region. This latter process causes the formation of the most luminous plasma region in the spark gap, hereby referred to as "plasma hot spot". When polarity changes, the existing hot spot collapses fast and another one builds up around the opposite electrode, which turns to be the instantaneous cathode during the next half cycle of the oscillations. It should be noted, that the present imaging setup cannot spatially resolve the cathode fall region in the vicinity of the momentary cathode, but the behavior of the discharge is fully in line with the above given arc-like behavior and hence provides an indirect evidence on the existence of the cathode fall region during the spark discharge.

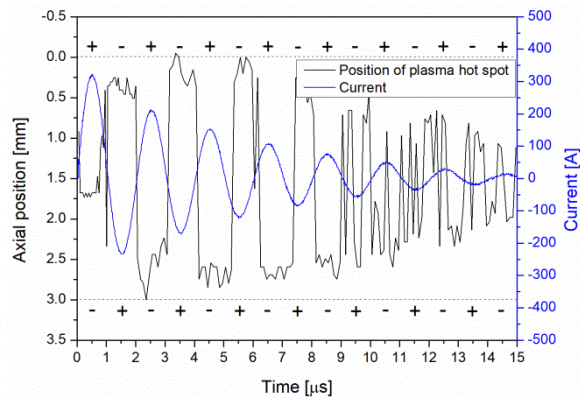


**Figure 3.2.4** Axial position of the plasma hot spot (black line) compared to the current waveform (blue line). The positions of the electrodes are marked by horizontal dashed lines. The instantaneous polarity of the electrodes is also shown (SDG B).

I also studied how the width of the spark channel evolves in time. The average channel width was determined by averaging the full width at half maximum of the light intensity traces perpendicular to the electrode axis for every row of the ICCD-image located between the two electrodes. **Figure 3.2.5** depicts the temporal evolution of the channel width for up to 15  $\mu\text{s}$ . Please note, that the determination of the channel width is complicated by the existence and axial movement of the plasma hot spot and the gradual loss of the initially well-defined cylindrical shape of the channel, which is well reflected in the degraded accuracy of channel width values at delays beyond about 3.5  $\mu\text{s}$ . Still, the following tendencies are clear and conclusive. First, the discharge sets off as a narrow channel (its width is below 500  $\mu\text{m}$ ) and then it grows monotonically. At around 3.5  $\mu\text{s}$  the channel width stabilizes around a value of about  $(1.5 \pm 0.2)$  mm.

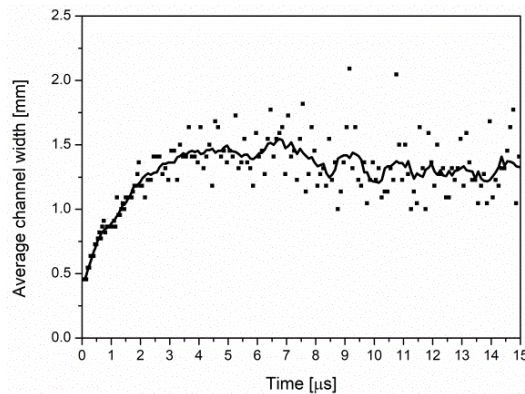


**Figure 3.2.5** Average channel width for spark discharges at a 2 mm gap size. The dots show the measured values of the channel width, while the solid lines are obtained by arithmetic averaging (using a 9-point moving window) (SDG B).

The expansion velocity of the plasma front was determined using the slope of the average channel radius as a function of time curve (assuming that the radial distance of the external front of the channel from the channel axis is the half of the average channel width). In **Figure 3.2.6** the early stage of the average channel width evolution at a gap length of 4 mm is plotted. The figure indicates that in the initial phase of the discharge, up until about 500 ns after the breakdown, the expansion velocity of the plasma front is

nearly constant and equals to about  $0.48 \text{ mm}/\mu\text{s}$ . This value is higher than the speed of sound in  $\text{N}_2$  at room temperature, which is  $0.35 \text{ mm}/\mu\text{s}$ . (One can add that the gas temperature in the gap before the spark may be higher than room temperature as a result of earlier spark events. If this is the case, the speed of sound is somewhat higher than  $0.35 \text{ mm}/\mu\text{s}$  according to the Newton-Laplace equation.) The above results mean that the expansion of the spark channel starts at supersonic speeds. Such fast growth of the plasma channel, together with the inherent change in temperature and gas pressure induces a shockwave [120]. The supersonic expansion was confirmed directly, for all but one cases used in this work (see later in **Figure 3.2.10**), since the characteristic sound was clearly audible during sparking.

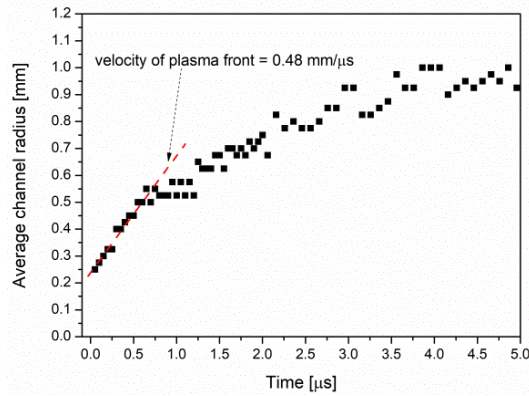


**Figure 3.2.6** Temporal evolution of the average channel radius for a spark discharge maintained between tipped electrodes at 4 mm gap size. The dashed (red) line indicates an initial plasma front expansion velocity of  $0.48 \text{ mm}/\mu\text{s}$  (SDG B).

It is plausible to assume, that at the beginning of expansion, the radius of the spark channel and the shockwave front coincide [120]. Therefore, the measurement of the initial front speed can be taken as a measurement of the shockwave velocity. Reinmann and Akram [121] used an interferometric method to follow the shockwaves created in similar spark discharges. They obtained radial velocities of the shockwave of about  $0.6 \text{ mm}/\mu\text{s}$ , which is somewhat faster than the highest expansion velocity obtained here. This difference can be explained by the different currents in the two cases. In the experiments reported by Reinmann and Akram, the current raised to about 400 A in less than 100 ns, while in my setup, the rate of current increase was smaller: it took about 500 ns to reach a value around 260 A, which would qualitatively explain a smaller expansion velocity.

### 3.2.3 Effect of the gap size on plasma morphology

In this section, I summarize the observations related to the effect of gap size on the studied spark parameters (i.e. total light intensity, position of plasma hot spot, channel width, and expansion velocity), obtained from my imaging measurements. **Figure 3.2.7** presents the time-resolved total light intensity curves at three different gaps. The general trend is that the total light intensity emitted is higher for larger gaps, which is in line with the observations that with increasing electrode distance, the energy dissipated in the gap is also increasing (see Section 3.1.2).

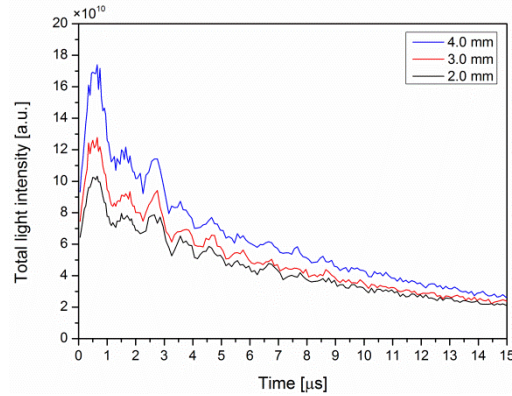


**Figure 3.2.7** The temporal evolution of total emitted light intensity collected at different gap sizes (SDG B).

The variation of the axial position of the “plasma hot spot” with the gap length is depicted in **Figure 3.2.8**. The results clearly show oscillations between the electrodes, which become more pronounced with increasing gap sizes. Despite measurement noise, it can also be clearly seen that the plasma tends to settle at the center of the gap as the oscillations decay.

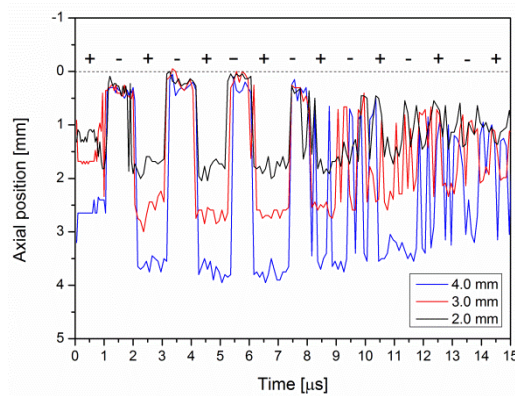


**Figure 3.2.8** The temporal evolution of the axial position of the most luminous part of the plasma (plasma hot spot) at different gap sizes. Note that for the sake of clarity, only the position of one electrode is shown given by the dotted line, for reference. The instantaneous polarity of the electrodes is also shown (SDG B).

**Figure 3.2.9** shows the evolution of the average channel width over time for several gaps. As can be seen, the spark channel undergoes similar expansion. By the end of the initial linear expansion (500 ns – 1  $\mu$ s) the channel becomes slightly wider with increasing gap size. After reaching a maximum, the channel width slowly moves towards values around 1.5 mm, for all gaps. The reason of this behavior is unclear.

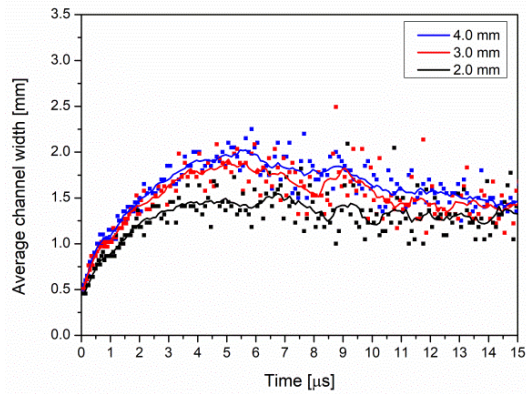


**Figure 3.2.9** Time evolution of the channel width at three different gap sizes. The points represent the measured values of the channel widths, while the solid lines are obtained by arithmetic averaging (using a 9-point moving window) (SDG B).

From the curves shown in **Figure 3.2.9**, as well as from measurements obtained at other experimental conditions, the initial expansion velocity of the plasma front (or the speed of the shockwave) was derived at different spark energies. In **Figure 3.2.10**, the initial expansion velocity, characteristic to the first, approx. 500 ns long period after the breakdown, is plotted as a function of spark energy. The graph convincingly proves that plasma channel expansion scales quasi-linearly with spark energy, and that this velocity is higher than the speed of sound, except for the lowest spark energy obtained at 0.5 mm gap size. At 0.5 mm gap size we observed that the spark show a different behavior, most probably because under that particular condition the discharge works in the micro-discharge regime [122,123].

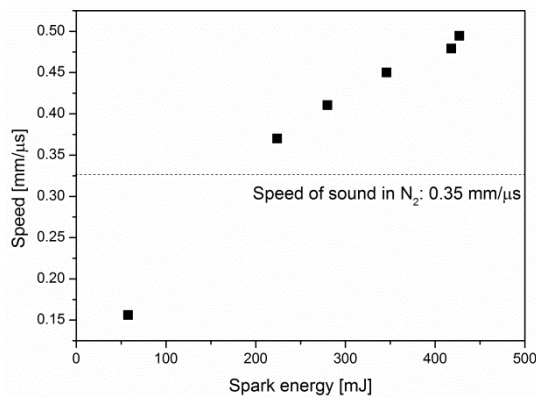


**Figure 3.2.10** Initial expansion velocity of the plasma front as a function of the spark energy. The dotted line marks the speed of sound in nitrogen at room temperature (SDG B).

Since the spark energy can be controlled by several parameters, such as the size of the spark gap, electrode geometry and circuit capacitance, it is then possible to adjust or control the expansion velocity of the spark channel by tuning these parameters.

### 3.3 Spectrally resolved optical emission of the spark plasma

#### 3.3.1 Experimental

Time-resolved optical emission spectroscopy (OES) measurements were carried out by an Andor Mechelle 5000 fiber-coupled echelle spectrograph equipped with an Andor iStar 734-18F-03 intensified CCD (ICCD) camera. In order to reduce the electromagnetic interference induced by the SDG, the spectroscopic instrumentation was set up in a nearby laboratory and the optical signal was transmitted to the spectrometer using a 12 m long fused silica optical fiber with 50  $\mu\text{m}$  core diameter. In one part of the experiments the emitted light from the plasma was spatially integrated over a ca. 6 mm diameter circular area (in a direction perpendicular to the axis of the electrodes) by using a quartz collection lens (Avantes COL-UV/VIS). The position of the collecting lens was optimized (to the highest optical signal) before each experimental run. In the other part of the measurements spectrum acquisition was carried out by spatial resolution. To this end, the 1:1 image of the spark plasma was produced with a fused silica lens and the bare end of the optical fiber (NA 0.22, SFS50/125Y, Thorlabs GmbH) was positioned to different locations over the image. The spectrograph was wavelength-calibrated and allowed for spectral data collection in the 300-800 nm wavelength range with  $\sim 0.125$  nm resolution (at 435 nm). The spectral sensitivity of the optical system was corrected by using a NIST-traceable deuterium-halogen calibration lamp (Model DH-2000-CAL, Ocean Optics, Inc.). The correction was checked before each experimental run and repeated if necessary.

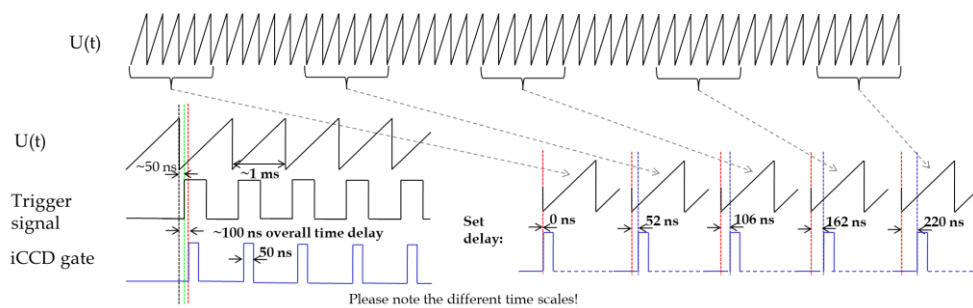


**Figure 3.3.1** Schematic timing of the ICCD camera with respect to the voltage signal of the sparking ( $U(t)$ ) in the particular case when 50 ns gate width is used with varying delay.

The light acquisition of the ICCD camera was triggered either by the sharp negative signal edge (provided by a Tektronix P6015A high-voltage probe) or the sharp positive signal edge (provided by a Pearson 110 current probe) caused by the breakdown of the gas between the electrodes. A Stanford DG535 pulse generator was used to produce a logical signal after the onset of the breakdown and initiated the exposure, i.e. the spectral acquisition. The overall time delay (including insertion delays and signal propagation) of the setup is around 70-100 ns, which thus defines the temporal starting point of the investigations with respect to the breakdown. In order to study the time evolution of the spark, emission spectra of the discharge were acquired at time delays varying from 0 ns to 50  $\mu\text{s}$ . The gate width of the camera, hence the temporal resolution of the measurements,

was set to either 50 ns or 500 ns. Each spectrum was measured on separate, consecutive sparks and few hundred spectra were accumulated at each experimental setting. The schematic graph of the timing of the ICCD is depicted in **Figure 3.3.1**. Spectral data processing was carried out by using Origin (Originlab Co.) and purpose-made scripts written in MATLAB (MathWorks, Inc.).

### 3.3.2 Temporally and spatially resolved emission spectrum of the spark plasma

The erosion of electrode material in the SDG is driven by the energetic sparking in the electrode gap. Due to this high energy input (on the order of 10<sup>9</sup> mJ in Ar and 100 mJ in N<sub>2</sub>) the electrode material is not only removed from the bulk electrodes but atoms are also excited and may even be ionized. The optical relaxation of these excited species is accompanied by the emission of photons which are characteristic to the particular spectroscopic transition. **Figure 3.3.2** represents the typical emission spectrum of the spark acquired by spatially integrating the photons leaving the electrode gap into the acceptance angle of the lens. The spectra acquired by temporal resolution were summed in order to illustrate the time-averaged spectral character of the spark emission.

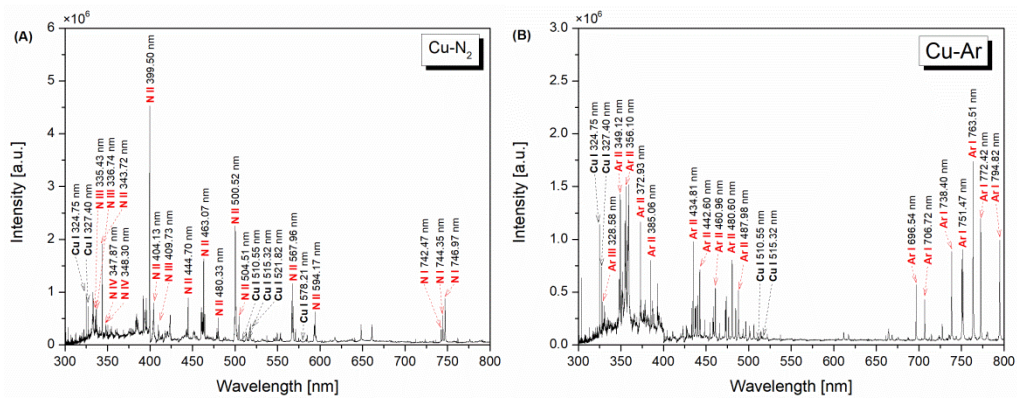


**Figure 3.3.2** Temporally and spatially integrated emission spectrum of the spark acquired during the generation of Cu NPs in nitrogen (A) and in argon (B) atmosphere (4 mm gap, 1.68 l/min gas flow rate, 10 mA charging current, SDG C).

As it can be seen in **Figure 3.3.2** the spectrum is dominated by the emission of the excited species of the gas ambient, namely spectral lines of atoms and singly or multiply charged ions<sup>4</sup> of nitrogen or argon (marked red in the spectra), depending on the type of carrier gas used. Atomic lines of the electrode material (copper, marked black in the spectra) are also present with much smaller relative intensity. This suggests that the number concentration of gas species exceeds that of the electrode material in the spark gap which will be discussed later.

<sup>4</sup> Please note that spectroscopic notation of spectral lines is used throughout the dissertation in parallel with the standard notation of neutral and charged species. Spectral lines arising from neutral species (e.g. Cu<sup>0</sup> and N<sup>0</sup>) are denoted by the Roman numeral I (e.g. Cu I and N I), while the lines emitted by singly charged ions (e.g. N<sup>+</sup>) are denoted by the numeral II (e.g. N II), and so on with ascending Roman numerals (III, IV, etc.) for multiply charged ions.

As a single spark has a characteristic temporal behavior (alternating voltage and current waveform with exponentially damping amplitude, see Section 3.1.1) the quantity and the properties (e.g. temperature) of the eroded material evolves in time as well. This temporal evolution is reflected in the emitted photons. Each temporal stage of the spark plasma (see Section 1.3.2) has different contribution to the erosion of the electrodes and also different characteristic light emission. The pre-breakdown and breakdown stages have negligible contribution to the erosion of the electrode material which is supported by the fact that spectroscopically these stages are characterized by molecular bands in the emission spectrum when a molecular gas is used as ambient gas [61]. In a typical, i.e. free-running SDG the breakdown is expected to complete quickly due to the low inductance of the discharge loop [61]. **Figure 3.3.2A** also proves that in the present case the breakdown completes in less than 100 ns, since the spectral acquisition started about 100 ns after the voltage drop between the electrodes, and the spectrum does not exhibit molecular nitrogen bands.

The duration of breakdown can also be estimated from the displacement current which is proportional to the first derivative of the voltage waveform. For an SDG operating with copper electrodes under argon atmosphere the derivative of the voltage exhibits a sharp peak about 15 ns before the current starts flowing. This peak is most probably associated with the breakdown of the gap, which therefore suggests that the breakdown completes in 40-50 ns, as indicated by the  $1/e^2$  width of the signal. This agrees well with the above considerations based on the absence of molecular bands in the emission spectrum of the spark. This very short breakdown duration means that the breakdown occurs practically instantaneously, as compared to the timescale of the entire emission process when the voltage between the electrodes drops.

The discharge enters the arc stage after the breakdown is completed and hence current is able to flow through the conducting plasma between the electrodes. The arc stage of the spark is accompanied by intense light emission, which is dominated by the spectral lines of ions and atoms of the ambient gas. The results to be shown in the following were obtained in an SDG operating with copper electrodes under argon atmosphere. The temporal behavior of the intensity of the emission from several ionic species measured in the center point of the spark gap is shown in **Figure 3.3.3A**. The light emission of  $\text{Ar}^+$  and  $\text{Ar}^{2+}$  follows the current oscillations in the discharge loop and is only detectable while electric current flows between the electrodes. This is due to the fact that the ionization (and excitation) energies of these species are high thus can only be supplied by the discharge when the temperature and electron concentration is the highest in the gap [53]. This implies that argon ions present and emit in the close proximity of the center of the current-conducting channel bridging the electrodes, therefore the light emission of these ions can be used to monitor the properties (e.g. position, extent, temperature) of the current-carrying channel. Apart from the emission of the ionic species, atomic argon emission is also detectable from the very beginning of the arc stage as evidenced by the temporally resolved spectra (see **Figure 3.3.4A**). As it will be shown later, it means that

argon atoms and ions coexist in the conducting spark channel and have the same temperature in a given position. However, they have different spreading rates and hence argon atoms spread farther apart from the electrodes' axis as time passes (cf. **Figure 3.3.3B** and **Figure 3.3.4B**).

Unfortunately  $\text{Cu}^+$  could only be detected with a very low signal-to-noise ratio, which is probably due to the reduced sensitivity of my instrumentation in the UV range, where dominant Cu II lines emit. The approximate time at which the light emission from  $\text{Cu}^+$  peaks differs significantly from that of the argon species. This proves that copper species are much less abundant in the gap at early times, since they are only produced in the arc stage.

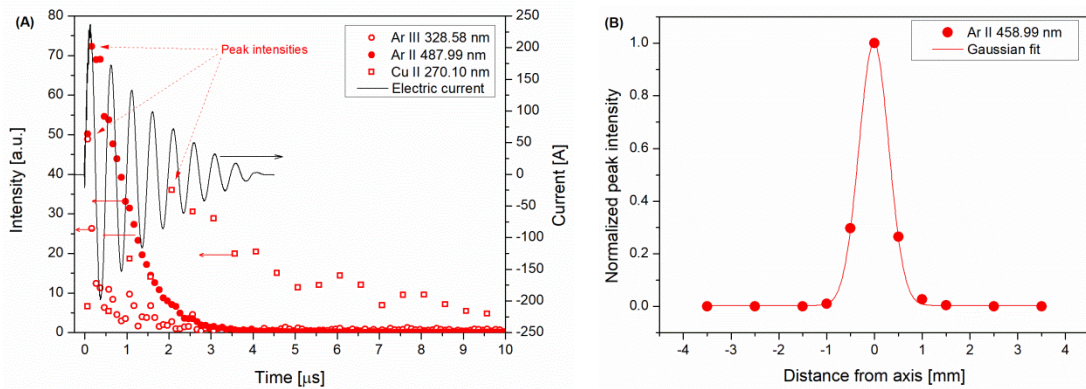


**Figure 3.3.3** Time evolution of the intensity of some selected *ionic* spectral lines, emitted from the center of the gap (A). The spatial variation of the peak intensity of an ionic Ar spectral line perpendicular to the electrodes' common axis, at the center of the gap (B) (Cu electrodes in Ar gas, SDG A).

In order to reveal the spatial extent of the spark channel, as defined by Ar ions during the arc stage, a 7 mm wide area perpendicular to the direction of the common axis of the electrodes was scanned at the center of the gap (i.e. in the direction of the argon flow). Time evolution curves, similar to those shown in **Figure 3.3.3A**, were constructed from the recorded emission spectra. In **Figure 3.3.3B**, the emission intensity at the maximum of the time evolution curves (denoted as peak intensities on **Figure 3.3.3A**) of the Ar II<sup>5</sup> line is plotted as a function of spatial position. Within the time-resolution of the present experiments the emission lines of Ar<sup>+</sup> ions reach their peak intensity simultaneously across a 2 mm wide area at around 500 ns after the onset of the breakdown. As can be seen in **Figure 3.3.3B**, the spatial distribution of the emission intensity of the Ar II species has a full width at half maximum (FWHM) of about 0.7 mm. This can be used to represent the diameter of the spark channel when the intensity of the given spectral line is at maximum, that is, when the formation of the channel is finished. It should be noted, that the spark channel evolves in time, which results in the broadening of the channel, as was

<sup>5</sup> Several spectral lines of each species have been investigated. It was confirmed that the intensity of spectral lines of the same species have similar temporal and spatial evolution. Therefore one line, detectable with good signal-to-noise ratio, was selected from each species as the representative spectral line of the given species.

already shown in Section 3.2.2, where an approx. threefold increase in diameter was found by the end of the arc stage in nitrogen atmosphere from the spectrally integrated data (cf. **Figure 3.2.5**).

In the afterglow stage, i.e. well after the conductive channel had ceased, light emission from the spark gap is still detectable even though no (further) energy is pumped into the spark gap from the capacitor. It is apparent from **Figure 3.3.4A**, that this sustained radiation is produced by excited *atomic* species. The intensity evolution of Ar I and Cu I spectral lines is shown in **Figure 3.3.4A**. The Ar I emission peaks within the arc stage of the discharge, and it sustains until approx. 50  $\mu\text{s}$ . The emission of copper atoms ceases approximately at the same time as that of the argon, but it reaches its peak intensity considerably later, at around 20  $\mu\text{s}$  after the breakdown.

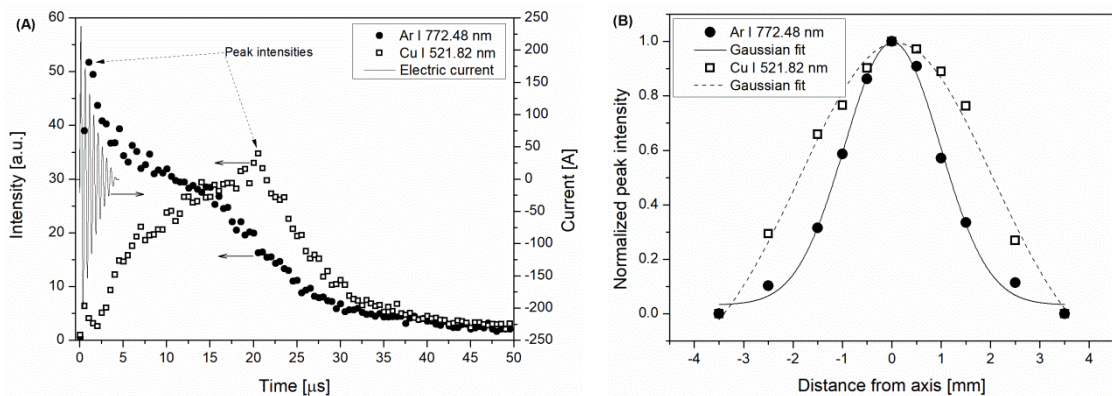


**Figure 3.3.4** Time evolution of the intensity of some selected *atomic* spectral lines, emitted from the center of the gap (A). The spatial variation of the peak intensity of some specific atomic spectral lines perpendicular to the electrodes' common axis, at the center of the gap (B) (Cu electrodes in Ar gas, SDG A).

**Figure 3.3.4B** shows the spatial distribution of the emission of atomic Cu and Ar when their respective peak intensity is reached. Unlike ions, where emission peaks in the arc stage, the peak intensity of atomic spectral lines shifts towards longer times as a function of distance from the electrodes' common axis. This suggests that during the afterglow, atomic species are spreading outwards from the center line of the spark channel, where ions exist in the arc stage and their emission exhibits spatial distributions having a characteristic FWHM of 2.3 and 4.6 mm for Ar and Cu, respectively. The broader intensity-distribution of the atomic copper lines are probably due to the much lower excitation energy of Cu, as compared to Ar atoms, therefore excited and emitting Cu species can exist also in the outer, somewhat cooler region of the discharge.

The emission spectroscopic results shown above illustrated the particular case when copper electrodes are used in argon gas. However, the considerations summarized above also hold for different electrode materials and carrier gases. This was proved by performing similar experiments with a variety of electrode materials and different carrier gases.

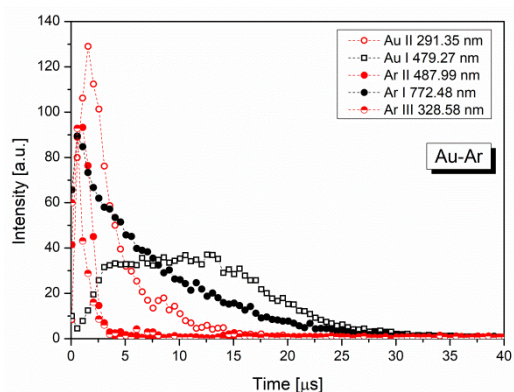


**Figure 3.3.5** Temporal evolution of the intensity of some selected *atomic* and *ionic* spectral lines, emitted from the center of the gap in case of gold electrodes in argon atmosphere. The points are connected to guide the eyes only (SDG A).

**Figure 3.3.5** illustrates the temporal evolution of the intensity of spectral lines acquired during the generation of Au NPs in argon atmosphere. The same order of appearance of the emission of different species is discernible. Namely that the intensity of spectral lines emitted by species of the gas ambient peaks first (ionic lines are ahead of that of the atoms), followed by the emission originating from the electrode material (similarly to Ar lines, Au II precedes Au I). The generality of the temporal behavior of different species exist in the spark gap also hold for different electrode materials.

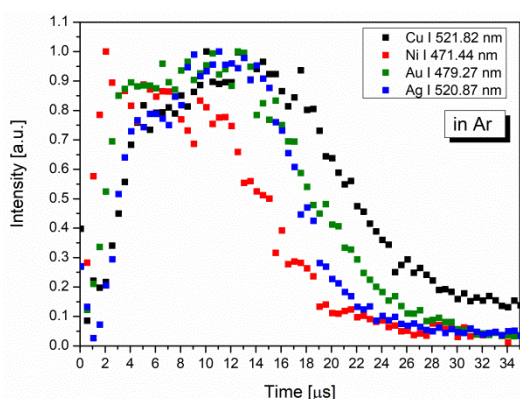


**Figure 3.3.6** Temporal evolution of the intensity of selected *atomic* spectral lines of Cu, Ni, Au, and Ag emitted from the center of the gap in case of argon atmosphere (SDG A).

**Figure 3.3.6** shows that the intensity of atomic spectral lines of four electrode materials, copper, nickel, gold, silver, evolves very similarly over time. The emission of the Ni I line peaks somewhat sooner than the rest of the lines of the metal atoms, but the overall trend of each dataset is almost identical.

### 3.3.3 Effect of control parameters on the emission spectra

In the following, the effect of two of the main control parameters, namely the gap size and charging current will be shown on the spectroscopic properties of various species (both that of the electrode material and the carrier gas), present in the spark gap. The experiments were performed using two electrode materials, namely Au and Cu under N<sub>2</sub>

atmosphere. Although monitoring the emission of metal atoms is most directly related to nanoparticle generation, along with that the emission of atomic nitrogen, the most abundant component of the spark plasma in the present case is also discussed here. To this end, the intensity (which is defined as the area under the spectral line) of selected atomic copper, gold and nitrogen lines (521.82 nm, 479.26 nm and 746.83 nm, respectively) was measured in the afterglow stage of the spark (more specifically, in a 10  $\mu$ s long temporal window starting 5  $\mu$ s after the onset of the breakdown). The temporally resolved spectra were summed in order to get a cumulated spectrum representing the afterglow stage.

Considering the typical SRR values obtained in the present experiments and the length of the afterglow stage it can be assumed that consecutive sparks are optically independent from each other, so the emission intensity of a single spark does not depend on the SRR. Therefore the emission intensity data shown below are always normalized to a single spark.

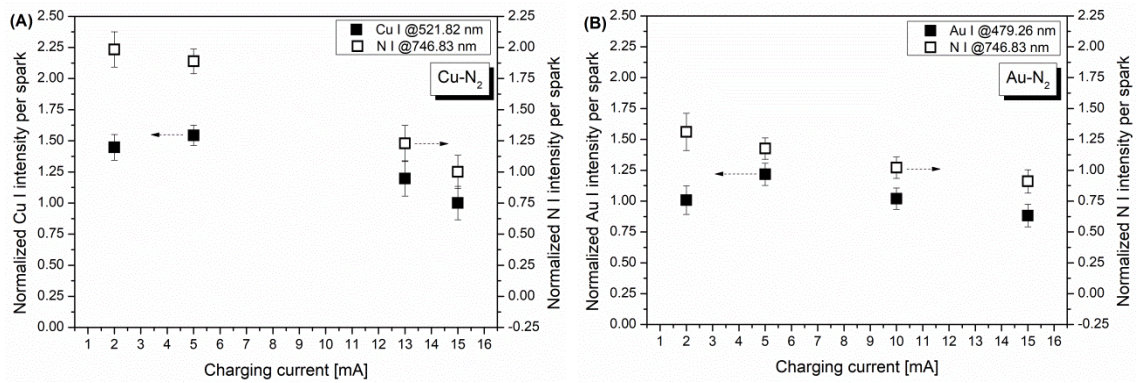


**Figure 3.3.7** Normalized intensity of an atomic spectral line of the gas and the electrode material as a function of the charging current acquired during sparking between Cu (A) and Au (B) electrodes in nitrogen. (SDG C, 2 mm gap size, 1.68 l/mni gas flow rate).

As can be seen in **Figure 3.3.7**, the intensity of atomic metal and gas spectral lines follows very similar trends in case of both Cu and Au electrodes. The atomic nitrogen emission decreases monotonously while the emission of metal atoms varies via a slight maximum with increasing charging current.

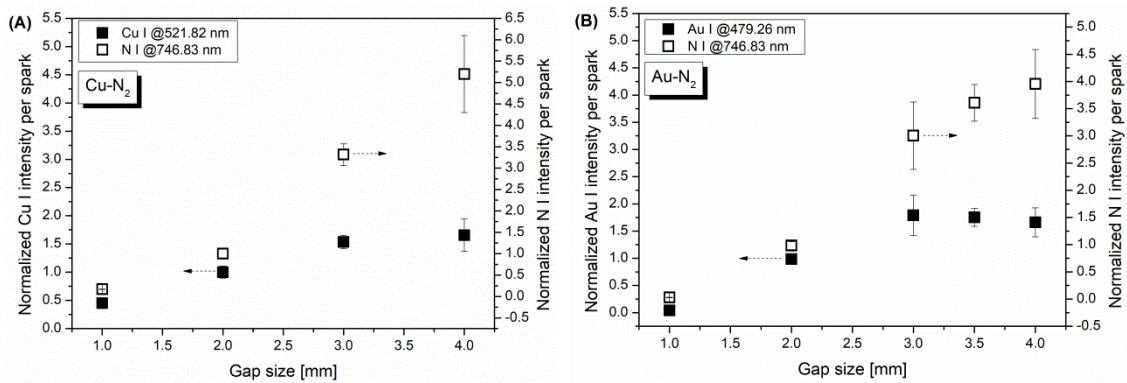


**Figure 3.3.8** Normalized intensity of an atomic spectral line of the gas and the electrode material as a function of gap size acquired during sparking between Cu (A) and Au (B) electrodes in nitrogen. (10 mA charging current, 1.68 l/min gas flow rate, SDG C).

The variation of the gap size results in a different trend. As it is shown in **Figure 3.3.8** the intensity of the N I line increases monotonously with increasing gap size, while the emission of metal atoms shows a saturating behavior after about 3 mm gap for both electrode materials.

**Figure 3.3.7** and **Figure 3.3.8** prove that the control parameters of the SDG (namely the gap size and the charging current) clearly affect the optical emission of the spark. The emission of atomic nitrogen behaves differently from that of the atomic gold and copper. The results obtained for different metal electrodes, namely copper and gold, in nitrogen atmosphere exhibit very similar trends.

The amount of metal vapor eroded by a single spark is determined by the spark energy<sup>6</sup> [84] and OES is a perfect tool to gain *in situ* information on the erosion process in this regard. If we assume that the optical emission of the spark plasma depends solely on the energy per spark (indirectly affecting the plasma temperature in addition to the concentration of the eroded material), the atomic emission intensities (shown in **Figure 3.3.7** and **Figure 3.3.8**) can be presented on the same graph regardless of whether the particular energy per spark value was achieved via varying the gap size, the charging current, or both. Please note, that the measured emission intensity values depend on the actual light collection conditions (e.g. the optical system, integration time, gain factor, averaging, etc.) so the spectra measured in different experimental runs were needed to be scaled to make trends comparable. In order to facilitate this re-scaling the measurement series were performed to contain overlapping energy values which were used to normalize the acquired spectra to the same stored energy.

<sup>6</sup> In the cited reference the spark energy is considered to be equal to the energy stored in the capacitor. I have previously shown in Section 3.1 that these two quantities are not necessarily equivalent, although they are proportional to each other when the electric circuit of the SDG is fixed. Since the results shown in the present section are obtained in an SDG of fixed electrical parameters, the tendencies presented hold both for the spark energy and stored energy. Since it is more straightforward to derive the stored energy, for the sake of convenience I will present the measured data as a function of the stored energy.

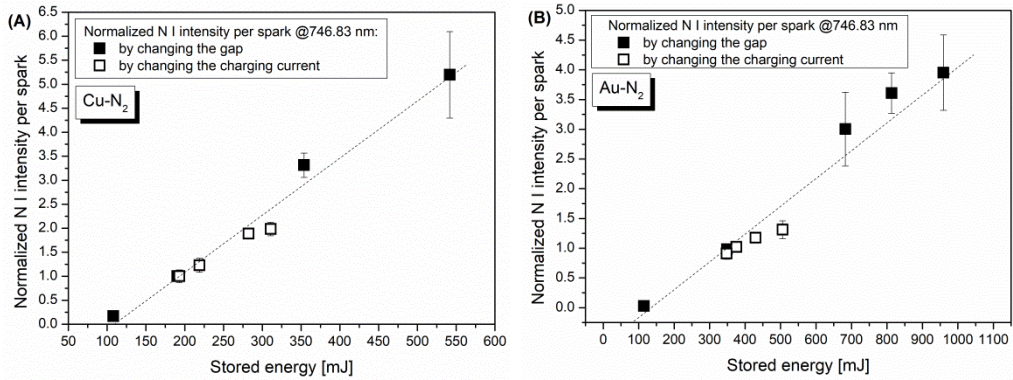


**Figure 3.3.9** Normalized intensity of an atomic nitrogen line as a function of the stored energy acquired during sparking between Cu (A) and Au (B) electrodes. (varying gap and charging current values, 1.68 slm gas flow rate, SDG C).

Since the most dominant feature of the emission spectra of the spark are the atomic and ionic lines of the ambient gas (here nitrogen) it seems logical to examine the effect of the energy stored in the capacitor<sup>6</sup> on the emission of nitrogen atoms. The normalized intensity of a typical atomic nitrogen line (N I 746.83 nm) measured at different stored energies during sparking between Cu and Au electrodes is shown in **Figure 3.3.9**. Points represented by closed symbols were obtained when the spark energy was varied via changing the gap size, while open symbols represent intensities obtained by the variation of the charging current. As it is illustrated by the fitted dashed line, the overall trend of the emission intensity is linear in the entire energy range studied, meaning that nitrogen atoms emit more light when the spark energy is increased, regardless of whether this increase is realized via adjusting the gap or the charging current. This also justifies the previous assumption on the dependence of the emission intensity on the spark energy. As can be seen in **Figure 3.3.9A** and **Figure 3.3.9B** the observed linear correlation applies to both electrode materials studied.

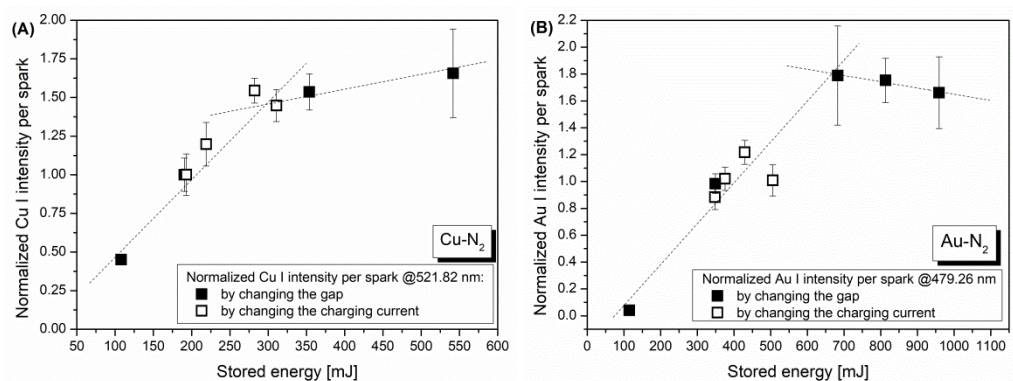


**Figure 3.3.10** Normalized intensity of an atomic Cu (A) and Au (B) line as a function of the stored energy acquired during sparking under nitrogen atmosphere. (varying gap and charging current values, 1.68 slm gas flow rate, SDG C).

As it is shown in **Figure 3.3.10**, the emission intensity of metal atoms behaves differently from that of the nitrogen. The emission intensity of Cu I increases roughly linearly up to about 300 mJ (by varying either the gap or the charging current), beyond

which the increasing tendency slows down, or even saturates (**Figure 3.3.10A**). A similar trend can be seen in **Figure 3.3.10B** for Au electrodes, with the sole difference that the threshold energy is about 600 mJ.

The intensity of a spectral line depends on the temperature and the concentration of the given species [124]. If we assume that the spark is in local thermodynamic equilibrium during the spectral acquisition (see Section 3.4.2 for the justification of this assumption in the afterglow) it follows that nitrogen and metal atoms, existing in the same spatial region, have the same temperature. This suggests that the difference observed between the dissimilar behavior of nitrogen and metal atoms (cf. **Figure 3.3.9** and **Figure 3.3.10**) should be attributed to the concentration difference of the two species. Nitrogen atoms are present in the spark gap before each spark event at a constant concentration while copper or gold atoms are only produced during sparking (cf. **Figure 3.3.4** and **Figure 3.3.5**). In light of this **Figure 3.3.10** suggests that after a certain threshold value, the energy is utilized less efficiently for increasing the concentration of metal atoms in the spark gap.

### 3.4 OES-based diagnostics of the spark plasma

#### 3.4.1 Methods

Temporally resolved emission spectra acquired with the instrumentation described in Section 3.3.1 were also used for plasma diagnostic calculations. More specifically, optical emission spectroscopic (OES) data (cf. **Figure 3.3.2**, **Figure 3.3.5**) were used to derive the temperature and the electron concentration of the spark plasma. The Boltzmann plot method (see e.g. [125,126]) is a widely used method for calculating the so-called excitation temperature of the plasma. Here one needs to assume, that the system is in local thermodynamic equilibrium (LTE), i.e. the population of the excited states obey the Boltzmann distribution. As a consequence, the emitted intensity of a transition between two energy levels ( $i \rightarrow j$ ) can be written as:

$$I_{ij} = \frac{hc}{\lambda_{ij}} A_{ij} \frac{1}{Z} g_i n e^{\left(\frac{-E_i}{kT}\right)} \quad (3.4.1)$$

where  $A_{ij}$  is the transition probability,  $Z$  is the partition function,  $g_i$  and  $E_i$  are the statistical weight and the energy of the excited level (denoted by subscript  $i$ ), respectively,  $k$ ,  $h$ , and  $c$  are the Boltzmann constant, the Planck's constant, and the speed of light, respectively,  $T$  is the excitation temperature,  $\lambda_{ij}$  is the wavelength of the transition, and  $n$  is the number concentration of the studied species. If we rearrange **Equation 3.4.1** it is apparent that different spectral lines of a selected species scatter around a straight line when  $\ln\left(\frac{I_{ij}\lambda_{ij}}{c g_i A_{ij}}\right)$  is plotted as a function of  $E_i$ :

$$\ln\left(\frac{I_{ij}\lambda_{ij}}{c g_i A_{ij}}\right) = \ln\left(\frac{hn}{Z}\right) - \frac{E_i}{k_B T} \quad (3.4.2)$$

The slope of the line (i.e.  $-\frac{1}{k_B T}$ ) as defined by **Equation 3.4.2** can be used to derive the excitation temperature of the given species. This form of the Boltzmann plot method

can only be used for a single species at a given ionization level. However, **Equation 3.4.2** can be generalized to a given species at different ionization levels or to different species at the same ionization level if additional information on the plasma is available. The former is called the Saha-Boltzmann method (see e.g. [64,126]) while the latter is the so called multi-element Saha-Boltzmann method [126].

When LTE exists in a plasma it is assumed that at a given spatial position (i.e. locally) all species have the same temperature which, together with the electron concentration, sets the concentration of the species at different ionization levels through the Saha equation:

$$n_+ = \frac{1}{n_e} 2 \frac{Z_+}{Z} \left( \frac{2\pi m_e k_B T}{h^2} \right)^{\frac{3}{2}} \exp\left(-\frac{W_+ - \Delta W}{k_B T}\right) n \equiv S n, \quad (3.4.3)$$

where  $n_e$  is the number concentration of electrons,  $W_+$  is the ionization energy of the studied species and  $\Delta W$  is the lowering of the ionization energy [127]. The + subscript refers to ions. By combining **Equations 3.4.2** and **3.4.3** the following generalized equation can be written for a given species at different ionization levels:

$$\ln\left(\frac{I_{ij}\lambda_{ij}Z}{hc g_i A_{ij} S}\right) = \ln(n) - \frac{E_i}{k_B T}, \quad (3.4.4)$$

where  $S$  is unity for atoms and can be calculated from **Equation 3.4.3** for each ionization level as a function of temperature and electron concentration. Plotting ions and atoms on the same graph obviously widens the energy spread of species and hence increases the accuracy of temperature determination via spectroscopic means. The validity of LTE assumption can also be inferred from the linearity of the plot. However, **Equation 3.4.4** requires the knowledge of the electron concentration and  $Z$  and  $S$  also contain the temperature, hence solving the Saha-equation requires an iterative process for determining the temperature.

Optically well resolved, interference- and self-absorption-free spectral lines need to be selected for the above calculations. The atomic data of transitions selected for the case of Cu electrodes in Ar gas were taken from the NIST database [128] and are tabulated in **Table 3.1**. The effect of self-absorption, which could potentially bias the results of the temperature calculation, was tested by using the double light path method [129] and was found to be negligible at the selected spectral lines used. It should be noted, that the accuracy of the excitation temperature values obtained can be influenced by the accuracy of the transition probabilities, which is also tabulated in **Table 3.1**.

**Table 3.1** Atomic data of selected Ar and Cu transitions;  $\lambda_{ij}$  is the emission wavelength,  $E_i$  and  $g_i$  are the energy and the statistical weight of the upper level and  $A_{ij}$  is the transition probability of selected atomic transitions, respectively.

Spectrum	$\lambda_{ij}$ [nm]	$E_i$ [cm <sup>-1</sup> ]	$g_i$	$A_{ij}$ [ $\times 10^7$ s <sup>-1</sup> ]	$A_{ij}$ accuracy [%]
Ar I	738.40	107290	5	0.85	$\leq 25$
Ar I	763.51	106237	5	2.45	$\leq 25$
Ar I	696.54	107496	3	0.64	$\leq 25$
Ar I	794.82	107132	3	1.86	$\leq 25$
Ar II	448.18	173393	6	4.55	$\leq 10$
Ar II	457.93	161089	2	8.00	$\leq 10$
Ar II	458.99	170401	6	8.20	$\leq 3$
Ar II	480.60	155043	6	7.90	$\leq 3$
Ar II	484.78	155708	2	8.50	$\leq 10$
Ar II	487.99	158730	6	7.80	$\leq 3$
Ar II	496.51	159393	4	3.94	$\leq 3$
Ar II	506.20	155351	4	2.23	$\leq 10$
Ar II	465.79	159706	2	8.10	$\leq 10$
Ar II	476.49	160239	4	5.75	$\leq 10$
Ar III	328.58	204803	7	20.00	$\leq 50$
Ar III	330.19	204656	5	20.00	$\leq 50$
Ar III	331.12	204570	3	20.00	$\leq 50$
Cu I	521.82	49942	6	7.50	$\leq 18$
Cu I	465.11	62403	8	3.80	$\leq 18$
Cu I	510.55	30783	4	0.20	$\leq 18$
Cu I	515.32	49935	4	6.00	$\leq 18$
Cu I	578.21	30535	2	0.17	$\leq 18$
Cu I	458.70	62948	6	3.20	$\leq 18$

The electron concentration in the spark channel during the arc stage was calculated from the Stark broadening of the emitted spectral lines. The Stark effect dominantly depends on electron impacts while the electric microfields of ions have a minor contribution [129]. In the present work the broadening of the 460.96 nm Ar II line was used to derive the electron concentration. In case of ionic lines, the contribution of ions to the Stark broadening is negligible and the Stark width, according to Konjevic [129], can be approximated by:

$$w(N_e, T_e) = w_e(T_e) \cdot N_e \cdot 10^{-17} \text{ cm}^3 \quad (3.4.5)$$

where  $w$  is the full width at half maximum (FWHM) of the Lorentzian line profile associated to Stark broadening,  $N_e$  is the electron concentration and  $w_e$  is the electron impact FWHM at  $N_e = 10^{17} \text{ cm}^{-3}$  and  $T_e$  is the electron temperature. As can be seen in **Equation 3.4.5**, the electron concentration can be derived from the Stark width of a spectral line if  $w_e$  is known at the given electron temperature. Prior to applying **Equation 3.4.5** to a measured line profile other broadening mechanisms, such as natural, Doppler, collisional and instrumental broadening have to be considered. By using a low-pressure calibration source I determined that the most dominant mechanism in the present case is instrumental broadening, which results in a Gaussian line profile (which has an FWHM of 0.128 nm in the present case). The Stark width of the spectral line was therefore obtained by fitting the measured line profile with a Voigt profile, having a

Gaussian component of fixed width accounting for instrumental broadening. It should be noted that the derived electron concentrations have uncertainties around 25%, set by the accuracy of the electron impact width value used in **Equation 3.4.5**. The electron width value used here was taken from [130].

The OES data processing and calculations were carried out by using Origin (OriginLab Corporation) and by purpose-made scripts written in Python 3.5 programming language and MATLAB (MathWorks, Inc.).

### 3.4.2 Properties of the spark plasma

The temporally and spatially resolved optical emission spectra of the spark allows for the derivation of the electron concentration, temperature and the concentration of the metal and gas species that exist in the spark plasma as a function of time and space. In the following the OES-based characterization of a spark plasma used for the generation of copper NPs under argon atmosphere will be shown, as an example.

During the arc stage of the spark, the electron concentration was derived from the Stark broadening of Ar II lines, as described in Section 3.4.1. The temporal evolution of the electron concentration in the spark channel (reported here for three points around the center of the spark gap) is shown in **Figure 3.4.1**. As can be seen its value decreases from  $\sim 7 \times 10^{17} \text{ cm}^{-3}$  to  $\sim 2 \times 10^{17} \text{ cm}^{-3}$  as the amplitude of the oscillating current decays. The three datasets plotted in **Figure 3.4.1** also prove, that the electron concentration is very similar across the 0.7 mm diameter plasma channel.

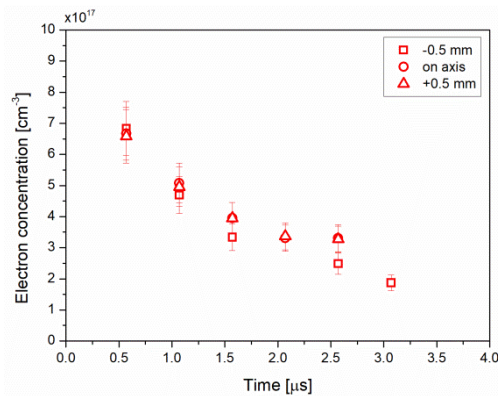


**Figure 3.4.1** The electron concentration of the spark plasma during the arc stage at different spatial locations (on axis and 2 radially symmetric positions, Cu electrodes in Ar gas, 2 mm gap, 100 Hz SRR, SDG A).

In accordance with the literature (e.g. [63,64]) I assume that the LTE condition holds in the arc stage of the spark discharge. Based on this assumption, the excitation temperature can be derived from the intensity of selected spectral lines by using the Boltzmann plot method (see Section 3.4.1 for further details). The existence of LTE could be checked by comparing the temperature values derived from the spectra of different species (see e.g. [64]). Unfortunately, in the present case the energy spread of the apparent spectral lines only allowed for temperature determination for Ar<sup>+</sup> ions. However, as it was pointed out in Section 3.4.1, indirect evidence on the existence of LTE can be found by constructing the Saha-Boltzmann plot of argon species at different ionization levels,

namely  $\text{Ar}^0$ ,  $\text{Ar}^+$  and  $\text{Ar}^{2+}$  (tabulated in **Table 3.1**). **Figure 3.4.2A** shows the Saha-Boltzmann plots obtained at different delays in the spark gap. Both Ar III, Ar II and Ar I lines are incorporated in the graph where the signal-to-noise ratio of the experimental data allowed me to do so.

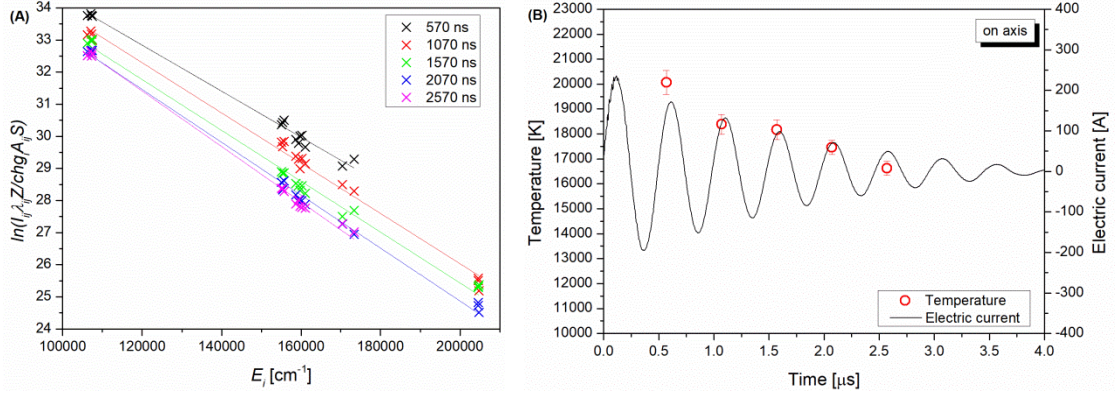


**Figure 3.4.2** Saha-Boltzmann plots obtained in the spark gap at different time delays (A), and the temporal variation of the temperature plotted over the oscillating electric current waveform (B). The temperature values were derived from the acquired emission spectra which were taken with a gate width of 500 ns at every 500 ns starting from about 70 ns after the peak current (Cu electrodes in Ar gas, 2 mm gap, 100 Hz SRR, SDG A).

As it can be seen in **Figure 3.4.2A**, the Saha-Boltzmann plots of argon atoms and ions show small scatter and good linearity up until 2500 ns delays. This provides a strong indication that  $\text{Ar}^0$ ,  $\text{Ar}^+$  and  $\text{Ar}^{2+}$  have the same temperature during the arc stage in the spark channel hence LTE is reached and allows for calculating a common temperature with relatively small uncertainty. The graph shown in **Figure 3.4.2B** presents the time evolution of the temperature derived in the center of the gap from the slope of the fitted lines shown in **Figure 3.4.2A**. The temperature (in the temporal range where the signal-to-noise ratio permitted the calculations) has a peak value of  $\sim(20000 \pm 480)$  K and decreases to  $\sim(16600 \pm 280)$  K following to the decrease of the amplitude of the current oscillations. The emission spectroscopic analysis of arc discharges in argon is investigated in detail for tungsten-inert gas (TIG) welding. Recently a thorough study was published on the temperature distribution of TIG arcs in the current range of 100-200 A, where peak temperatures of about 17000-19500 K were reported near the cathode [131]. These values agree fairly well with the temperatures we obtained here in the 0.5-2.0  $\mu\text{s}$  time range in which the peak current is also around 100-200 A.

*During the afterglow stage*, the electron concentration is not high enough to facilitate the reliable observation of Stark broadening of the spectral line with the instrumentation I used. The temperature is also lower, therefore the spectral lines of ionic species could not be detected and hence Saha-Boltzmann method could not be used, either. Therefore I developed the following model for deriving the temperature and estimating the concentration of the species populating the discharge gap in the afterglow regime. The model is based on the following assumptions: *i*) atmospheric pressure prevails in the spark gap, *ii*) the discharge is only composed of electrons and the neutral and singly

charged ionic species of the ambient gas, as well as that of the electrode material (here: electrons, Ar, Ar<sup>+</sup>, Cu, Cu<sup>+</sup>), *iii*) LTE holds, *iv*) the net charge of the discharge plasma is zero. These assumptions can be expressed via the following equations:

$$n_{Cu^+} + n_{Ar^+} = n_e \quad (3.4.6)$$

$$p = (n_{Cu^0} + n_{Ar^0} + n_{Cu^+} + n_{Ar^+} + n_e)k_B T \quad (3.4.7)$$

$$I_{Cu^0} = h\nu_{Cu^0} A_{Cu^0} \frac{1}{Z_{Cu^0}} g_{Cu^0} \exp\left(\frac{-E_{Cu^0}}{k_B T}\right) n_{Cu^0} \quad (3.4.8)$$

$$I_{Ar^0} = h\nu_{Ar^0} A_{Ar^0} \frac{1}{Z_{Ar^0}} g_{Ar^0} \exp\left(\frac{-E_{Ar^0}}{k_B T}\right) n_{Ar^0} \quad (3.4.9)$$

$$\frac{n_e n_{Cu^+}}{n_{Cu^0}} = 2 \frac{Z_{Cu^+}}{Z_{Cu^0}} \left(\frac{2\pi m_e k_B T}{h^2}\right)^{\frac{3}{2}} \exp\left(-\frac{W_{Cu^+} - \Delta W}{k_B T}\right) \quad (3.4.10)$$

$$\frac{n_e n_{Ar^+}}{n_{Ar^0}} = 2 \frac{Z_{Ar^+}}{Z_{Ar^0}} \left(\frac{2\pi m_e k_B T}{h^2}\right)^{\frac{3}{2}} \exp\left(-\frac{W_{Ar^+} - \Delta W}{k_B T}\right) \quad (3.4.11)$$

where  $n_{Cu^0}$ ,  $n_{Ar^0}$ ,  $n_{Cu^+}$ ,  $n_{Ar^+}$  and  $n_e$  are the concentration of copper atoms, argon atoms, singly charged copper and argon ions, and electrons, respectively.  $p$  denotes the pressure in the gap,  $T$  is the equilibrium plasma temperature,  $I_{Cu^0}$ ,  $I_{Ar^0}$ ,  $\nu_{Cu^0}$ ,  $\nu_{Ar^0}$  are the intensity and the frequency and  $g_{Cu^0}$ ,  $g_{Ar^0}$  and  $E_{Cu^0}$ ,  $E_{Ar^0}$  are the statistical weight and the energy of the upper state of a specific Cu I and Ar I spectral line, respectively.  $Z_{Cu^+}$ ,  $Z_{Cu^0}$ ,  $Z_{Ar^+}$ ,  $Z_{Ar^0}$  are the partition functions of Cu and Ar ions and atoms, respectively,  $h$  is the Planck's constant,  $k_B$  is the Boltzmann constant,  $m_e$  is the mass of electron,  $W_{Cu^+}$  and  $W_{Ar^+}$  are the first ionization energies of Cu and Ar, respectively and  $\Delta W$  is the decrease in the ionization energy according to Griem [127]. **Equation 3.4.6** expresses the neutrality criterion, **Equation 3.4.7** is Dalton's law, **Equations 3.4.8** and **3.4.9** are the emission intensity of an atomic copper and argon line, respectively while **Equations 3.4.10** and **3.4.11** denote a pair of Saha-Boltzmann equations describing the ratio of the concentration of ions to atoms for Cu and Ar, respectively.

Two of the above given assumptions need to be corroborated. First, one has to assume that the discharge is under atmospheric pressure during the afterglow stage. The breakdown is accompanied by a pressure peak which can be as high as 120 bar in case of a nanosecond spark discharge [121]. After this peak pressure drops exponentially and settles close to atmospheric pressure again by the end of the arc stage [80,121]. Although the exact pressure values might depend on the experimental conditions, considering this rapid exponential decrease it is safe to assume that the initial atmospheric pressure is quickly reached in about 10  $\mu$ s after the onset of the breakdown.

The other main assumption of **Equations 3.4.6-3.4.11** is the LTE condition during the afterglow stage. As it was pointed out earlier it is widely accepted in the scientific literature that LTE is reached in less than a microsecond after the onset of the breakdown in spark discharges [53,63]. However, it is not trivial how long this equilibrium exists during the afterglow stage of the discharge. Since the electron concentration is decreasing, the spark plasma is recombining during the afterglow, therefore it is clear that time-

averaged LTE-based techniques could not be applied, so temporally resolved measurements are needed, instead. Therefore, I assume that the discharge evolves through quasi-equilibrium intermediate states, in which LTE conditions hold during the 500 ns temporal window of the spectral acquisition and hence **Equations 3.4.6-3.4.11** can be applied to characterize the spark. Considerations about the validity of this assumption will be made later in this section.

The intensity ratio of atomic copper and argon lines can be calculated from **Equations 3.4.6-3.4.11** in a given temperature and electron concentration range. By comparing the calculated values with experimentally determined intensity ratios the plasma parameters can be deduced. The measured intensity ratios of two Cu-Ar line pairs (Cu I 521.82 nm/Ar I 738.40 nm and Cu I 515.32 nm/Ar I 751.53 nm) were used to find solutions of **Equations 3.4.6-3.4.11**. In order to find the best possible solution Saha-Boltzmann plots were constructed incorporating the atomic emission lines of both argon and copper. This requires the modification of **Equation 3.4.4** by weighting the left side with the concentration of the given species (denoted as  $n$ ) calculated from **Equations 3.4.6-3.4.11**. It is expected that if both Saha and Boltzmann equilibrium conditions are met (i.e. assumptions of **Equations 3.4.6-3.4.11**) the points belonging to argon and copper lines lie on the same line. A further verification of the calculated data was made by simulating the emission spectrum (including the calculation of the Voigt line profiles dependent on the derived plasma parameters) and comparing it to the measured spectrum.

By using this model, the discharge parameters (i.e. the equilibrium plasma temperature, electron concentration, and the concentration of the species in the gap) were estimated from the emission spectra collected 20.5  $\mu$ s after the breakdown, namely at the time when the Cu I emission is about its maximum. The multi-element Saha-Boltzmann plot obtained from 6 Cu I and 4 Ar I spectral lines (see **Table 3.1**) measured around the center of the gap is shown in **Figure 3.4.3A**. It can be seen that the points at similar energies overlap and both Cu and Ar lines nicely fit on the same line indicating the consistency of the results. The error of the derived temperatures comes from the error of the slope of the linear fit to the points of the multi-element Saha-Boltzmann plot and ignores the uncertainty of constants used for the calculations (see Section 3.4.1). This uncertainty translates to an absolute temperature error of about 130-300 K for most cases discussed here. It should be noted, that the concentration values derived from the model are fairly sensitive to temperature variation, so spectral lines having upper energy spread as wide as possible should be incorporated in the Saha-Boltzmann plot in order to maximize the accuracy of temperature determination (c.f. the comparison of the accuracy of the Boltzmann and Saha-Boltzmann methods in Section 3.4.1). The emission spectrum of the three most dominant Cu I spectral lines simulated under plasma conditions derived from **Equations 3.4.6-3.4.11** is shown in **Figure 3.4.3B** together with the measured spectrum. The effect of the error of the temperature calculation on the simulated spectrum is indicated by a grey zone around the solid, black curve.

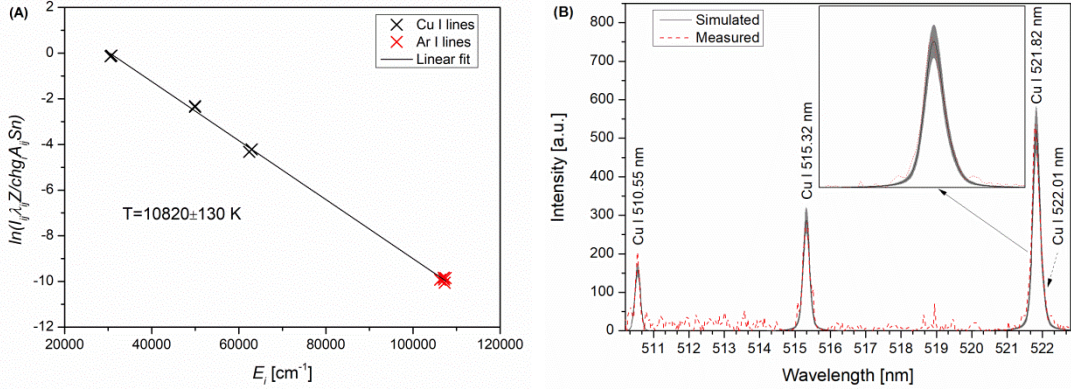


**Figure 3.4.3** Multi-element Saha-Boltzmann plot of atomic Ar and Cu lines (A) and the spectrum of the three most dominant Cu I lines measured (dashed curves) and simulated (solid curves) (B) in the center of the gap at 20.5  $\mu$ s after the breakdown. The error is shown as a grey zone around the simulated spectrum. The 521.82 nm peak is shown magnified in the inset (Cu electrodes in Ar gas, 2 mm gap, 100 Hz SRR, SDG A).

It can be seen from **Figure 3.4.3B** that the simulated spectrum fits the measured one neatly, which suggests that the initially assumed LTE condition is met and this model describes the spark in the SDG during the afterglow stage fairly well. The parameters calculated from spectra measured in the center of the gap at 20.5  $\mu$ s after the breakdown are summarized in **Table 3.2**. It can be seen that the temperature is about (10820 $\pm$ 130) K, and the electron concentration is ca. (3.59 $\pm$ 0.39)  $\times 10^{16}$  cm $^{-3}$ , the latter is about one order of magnitude smaller than the characteristic value at the end of the arc stage (cf. **Figure 3.4.1**).

**Table 3.2** Calculated parameter values for the center of the gap 20.5  $\mu$ s after the breakdown.  $n_{Cu}$  and  $n_{Ar}$  denote the sum of the concentration of ion and atoms of Cu and Ar species, respectively. The error of the concentrations was derived from the error of the temperature determined from the Saha-Boltzmann plot.

$T$ [K]	$n_e$ [ $10^{16}$ cm $^{-3}$ ]	$n_{Cu0}$ [ $10^{13}$ cm $^{-3}$ ]	$n_{Ar0}$ [ $10^{17}$ cm $^{-3}$ ]	$n_{Cu+}$ [ $10^{14}$ cm $^{-3}$ ]	$n_{Ar+}$ [ $10^{16}$ cm $^{-3}$ ]	$n_{Cu}$ [ $10^{14}$ cm $^{-3}$ ]	$n_{Ar}$ [ $10^{17}$ cm $^{-3}$ ]
10820 $\pm$ 130	3.59 $\pm$ 0.39	3.85 $\pm$ 0.36	6.08 $\pm$ 0.16	9.24 $\pm$ 1.08	3.49 $\pm$ 0.38	9.63 $\pm$ 1.08	6.43 $\pm$ 0.16

The temporally resolved data, together with my simple model, also allow for estimating the rate of change of temperature and electron concentration during the afterglow. By evaluating the data in the center of the gap  $\frac{dT}{dt} \approx -3.4 \times 10^8 \frac{K}{s}$  and  $\frac{dn_e}{dt} \approx -1.4 \times 10^{22} \frac{cm^{-3}}{s}$  are obtained. From this it follows that the temperature and the electron concentration changes by  $\sim 170$  K and  $\sim 7 \times 10^{15}$  cm $^{-3}$ , respectively during the 500 ns temporal window of the spectral acquisition, which corresponds to a  $\sim 1.5\%$  and  $\sim 20\%$  change of the temperature and electron concentration, respectively. The electron concentration is frequently used to estimate whether LTE exists in a spark plasma or not, by comparing it to a critical value calculated from the Griem criterion [64]. Although one cannot rely solely on the electron concentration, this criterion could provide a rough estimate of the temporal window in which LTE holds in the afterglow. From the values

reported earlier I obtained that LTE does hold in the studied system until around 24  $\mu\text{s}$  after the breakdown.

In order to investigate the spatial distribution of species emitting in the spark plasma, emission spectra were taken at different spatial locations, both along the electrodes' axis and perpendicular to it. In addition to these measurements, fast imaging (by means of a separate ICCD camera) was used in order to acquire data on the exact shape of the discharge under the present experimental conditions. The cylindrical shape of the discharge which is characteristic to the arc stage becomes more diffuse after the current ceases, which fits nicely into the general tendency of plasma morphology evolution, shown previously in **Figure 3.2.2**. The image of the spark gap at 20.5  $\mu\text{s}$  after the breakdown, acquired concomitantly with the spectral measurements is shown in **Figure 3.4.4**.

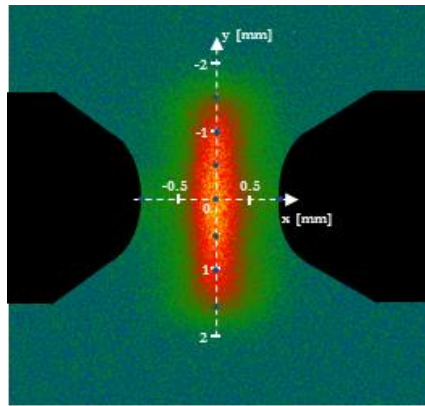


**Figure 3.4.4** Image of the electrode gap taken with 100 ns exposure time at 20.5  $\mu\text{s}$  after the breakdown. The points where emission spectra were taken are indicated by the blue dots along the axes (Cu electrodes in Ar gas, 2 mm gap, 100 Hz SRR, SDG A).

Under the conditions used in these measurements the image, i.e. a 2D projection, of the spark shows the presence of an emitting, more-or-less rectangular area having dimensions of  $\sim 3$  mm in height, i.e. perpendicular to the electrodes' common axis and  $\sim 1$  mm in width, i.e. along the electrodes' common axis. Please note, that the emission collected by the imaging ICCD is spectrally integrated, thus the image cannot be directly related to the distribution of a specific species. Still, it suggests that the overall emission of the excited species is fairly homogenous in the central core. However, by evaluating the spectrally resolved emission taken at different spatial points (indicated by blue dots in **Figure 3.4.4**) the distribution of the spark parameters, namely temperature and electron concentration, can be derived from my semi-empirical model based on **Equations 3.4.6-3.4.11**. The calculated temperatures and electron concentrations and their spatial variation, both along and perpendicular to the electrodes' common axis are shown in **Figure 3.4.5**.

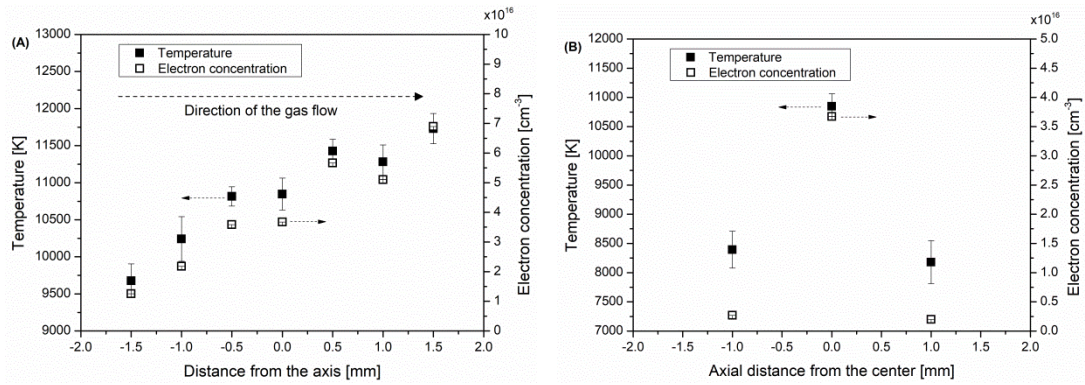


**Figure 3.4.5** Spatial variation of temperature and electron concentration perpendicular to (A) and along (B) the electrodes' common axis 20.5  $\mu\text{s}$  after the breakdown (Cu electrodes in Ar gas, 2 mm gap, 100 Hz SRR, SDG A).

As can be seen in **Figure 3.4.5A**, perpendicular to the electrodes' common axis, the temperature and electron concentration exhibit an increasing trend in the direction of gas flow. This result suggests that the 5 l/min gas flow employed in the SDG has an effect on spark parameters resulting in higher temperature and larger electron concentration downstream of the flow. Contrary to this, the distribution of the temperature and electron concentration along the electrodes' common axis is symmetric, as shown in **Figure 3.4.5B**. The distribution of the Ar and Cu species in the gap was also investigated by employing the model to estimate the concentration of each species at different spatial positions.

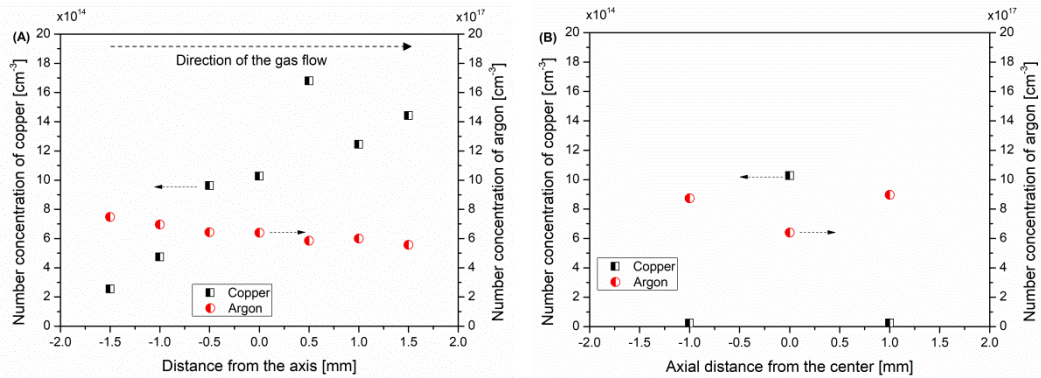


**Figure 3.4.6** Spatial distribution of total number concentration of copper and argon species (i.e. the sum of the atomic and ionic species) perpendicular to (A) and along (B) the electrodes' common axis, 20.5  $\mu\text{s}$  after the breakdown (Cu electrodes in Ar gas, 2 mm gap, 100 Hz SRR, SDG A).

As can be seen in **Figure 3.4.6** the concentration of argon (i.e. the sum of the atomic and ionic species) is about 2-3 orders of magnitude higher than the average number concentration of copper. The number concentration of copper increases, while the argon concentration slightly decreases in the direction of the gas flow (c.f. **Figure 3.4.6A**). The increasing amount of Cu correlates to the fact that the majority of copper is in ionic form whose concentration increases with increasing temperature.

In the axial direction, the argon concentration exhibits slight and symmetrical changes, while the total concentration of copper species varies significantly in the -0.5 mm - +0.5 mm axial range. It is, by a factor of about 50, smaller close to the electrode tips as

compared to the value obtained in the middle of the gap. The results are summarized in **Figure 3.4.6B**. The two distributions shown in **Figure 3.4.6** suggest that at 20.5  $\mu\text{s}$ , the copper plume is concentrated in the middle of the gap and exhibits increasing concentration along the direction of the carrier gas flow.

### **3.5 Morphology of the electrode surface after sparking**

#### **3.5.1 Experimental**

For studying the effect of erosion on the surface morphology, electrodes were exposed to sparking in a well-controlled manner. For the initiation of a single or a few sparks in the SDG (which is primarily designed for continuous operation) custom circuitry was developed for the power supply, which allowed for either manual or electrical triggering of the spark. Thereby, in these experiments the number of sparks as well as their repetition rate was well-controlled. The electrodes employed in this investigation were cylinders of 3 mm diameter. Cu (99.9% purity, Kurt J. Lesker Co.) and Ni electrodes of high purity (99.9%) were prepared by polishing one of the cylinder faces. Polishing was preceded by successive water-lubricated sanding with 600, 800 and 1200 grit sanding paper. Polishing was conducted employing synthetic diamond suspensions of 9  $\mu\text{m}$ , 3  $\mu\text{m}$  and 0.25  $\mu\text{m}$  grain sizes on polishing cloth. The remnants of the polishing grit was removed by brief ultrasonication in demineralized water, as well as by careful wiping with low-lint wiped soaked in ethanol.

Before each experiment, the morphology of the electrode surfaces was documented using optical dark-field and bright-field microscopy. Bright-field microscopy did not reveal any blemishes on the polished electrode surface, however dark-field illumination revealed the presence of straight scratches with characteristic lengths in the range of a few tens of micrometers to several millimeters. The scratches are distributed randomly on the surface, which suggests that they were formed during the polishing procedure.

In order to guide the spark channel towards the center of the polished electrode surface and to avoid sparking between the edges of the electrode rods, removable caps made from insulating materials were used to cover most of the opposing electrode faces except for a central circular area of approx. 1-2 mm in diameter. The electrodes were horizontally positioned and axially aligned with submillimeter accuracy. The inter-electrode distance (i.e. electrode gap) was controlled by micropositioners (Model K150-BLM-1, MDC Vacuum Ltd.) and set to 2.0 mm for all results reported herein. The experiments have been carried out in atmospheric pressure nitrogen, flowing with a rate of 5 l/min. After the initiation of a single spark or a controlled number of sparks, the electrodes were removed and characterized by optical microscopy (OM), confocal laser scanning microscopy (CLSM), and atomic-force microscopy (AFM) with the instruments Nikon Optiphot 100S, Keyence VK-X100K, and PSIA XE-100, respectively.

The effect of prolonged sparking on the electrode surfaces was also investigated in case of nickel, gold and silver electrode materials (>99.95% purity, ChemPUR GmbH,

Germany). The electrodes were cylinders with a diameter of 3 mm and they were positioned axially, at a distance (gap size) of 3 mm. The SRR was kept constant at a value of about 30 Hz throughout the experiments, which were carried out in atmospheric pressure nitrogen. After sparking between the electrodes for several hours, the changes occurring on the surface of the electrodes were documented using CLSM (Keyence VK-X100K).

### 3.5.2 Surface of the electrodes after sparking

**Figure 3.5.1A** shows the surface of a polished nickel electrode subjected to a single oscillatory spark discharge. It can be seen that even a single spark results complex morphological changes on the surface of the electrodes. The overall appearance of the spark-hit surface is the following: the discharge affects the surface at several, partially overlapping areas that have a roughly circular shape and are scattered all over the exposed electrode surface. The presence of multiple erosion sites on the surface can be qualitatively explained by the multiple peaks in the current and voltage waveform of the spark, which assumption is supported by the fact that the number of the structured sites is comparable to that of the half-periods in the oscillatory current waveform shown in **Figure 3.5.1B**. As it was shown in Section 3.1.1, the sparks produced in an SDG have oscillatory behavior, therefore each spark can be considered as a series of sub-discharges with alternating polarity and exponentially damping voltage and current amplitude (**Figure 3.5.1B**). **Figure 3.5.1** suggests that this oscillatory nature of the spark plays an important role in the formation of the complex surface morphology observed.

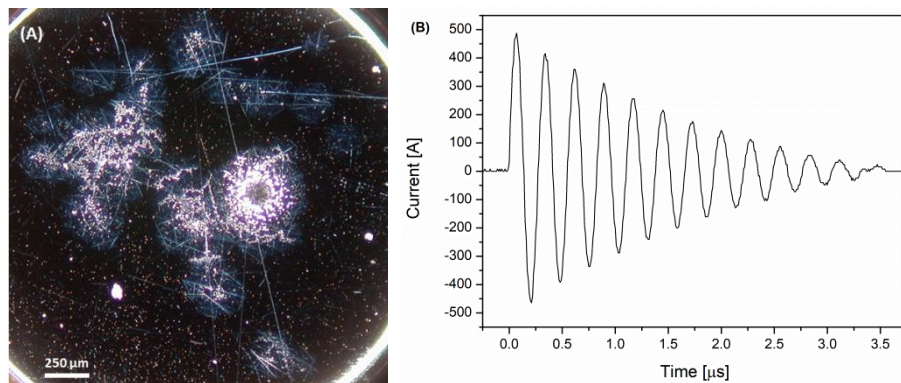


**Figure 3.5.1** Dark field OM micrograph of the surface of an initially cathodic, polished nickel electrode after a single spark (A). Current waveform of the oscillatory spark discharge (B) that produced the morphology shown in part A (SDG A).

The detailed investigation of the electrode surface exposed to a single spark reveals three, well distinguishable morphological structures. **Figure 3.5.2** exemplifies these surface features, namely craters (a), “undulated areas” (b), and “dendritic areas” (c). These morphological features will be discussed in detail below

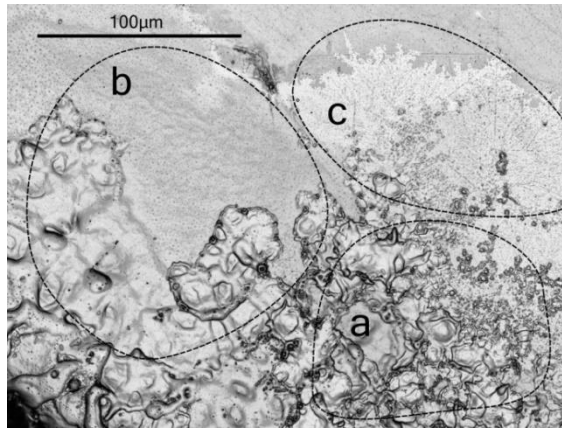


**Figure 3.5.2** CLSM micrograph of an initially anodic nickel electrode surface after a few oscillatory discharges. Each circled area exemplifies a typical morphological feature a) craters, b) undulated area, c) dendritic area (SDG A).

### *Craters*

Craters are the most abundant surface feature produced by a single spark. Even during a single oscillatory discharge, several hundred to several thousand craters are formed on the surface. Craters are characterized by a roughly circular central depression surrounded by a protruding rim of distinctly molten appearance (cf. the AFM topographic image of a chain of craters in **Figure 3.5.3**). Micropoints and strands of metal on the rim indicate a fast movement of molten material with subsequent rapid re-solidification. Individual craters often occur in the vicinity of each other, sometimes leading to a cluster of overlapping craters. The latter appearance is more typical for larger craters, while small craters are usually scattered with some distance between them.

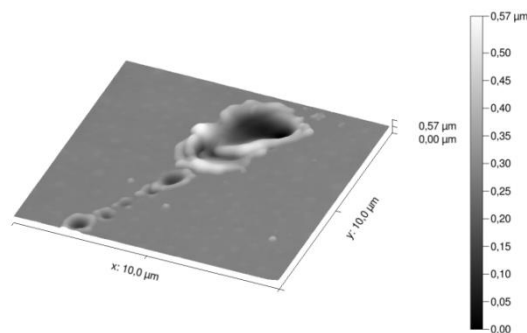


**Figure 3.5.3** Visualization of an ensemble of craters, based on AFM data (SDG A).

The crater morphology was found to be identical for both nickel and copper electrodes. The depth of the craters is always significantly smaller than their radius, and craters can be described as hemi-ellipsoidal in shape. The appearance of craters does not show polarity dependence, both initially anodic and cathodic electrodes exhibit similar morphology. An exception to this was found for the largest craters, where a peculiar arrangement was typical for initially cathodic electrodes (this will be elucidated in Section 3.5.3).

When investigating the electrode surfaces the evidence of another erosion phenomenon was also observed, which can be referred to as “splashing”. This supposedly accompanies crater formation, hence it cannot be considered as a primary feature. The displacement of the melt during crater formation also results in the ejection of molten droplets (melt expulsion), some of which will relocate around the perimeter of the crater (as shown in **Figure 3.5.4**), while other may also be ejected into the gas phase. This could explain the presence of micrometer-sized droplets at the rim of surface areas covered by craters.

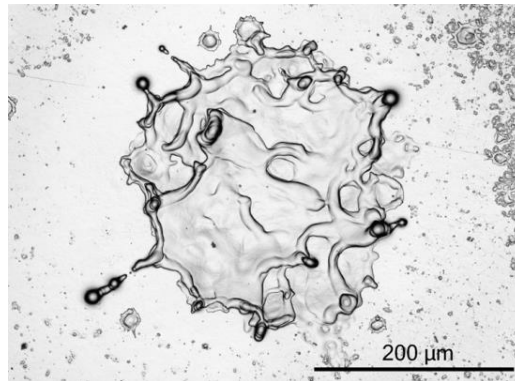


**Figure 3.5.4** Ensemble of micron-sized droplets on a nickel electrode (CLSM image, SDG A).

#### *Undulated areas*

This surface feature is characterized by a coherent area of characteristically undulated or wavy appearance, in which pre-existing surface features (e.g. scratches) as well as craters appear to be smoothed (**Figure 3.5.5**). The creation of these undulated areas homogenizes the morphology of the surface they cover, including other features, e.g. scratches and craters.

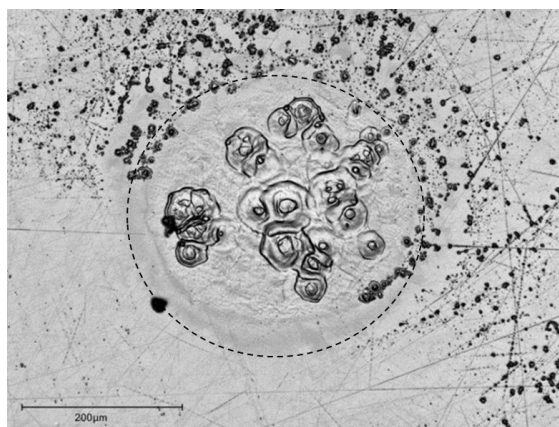


**Figure 3.5.5** An undulated area (indicated by a circle) with a central ensemble of craters. Note the effect of smoothing, which is most prominent on craters within the undulated area (SDG A).

The smoothing effect is also observable at the submicron scale. Towards the center of an undulated area, the smoothed surface transforms into a wavy structure. The intensity of smoothing is most pronounced and the roughness is the largest in the center

of the area and decreases with increasing distance from the center. At the edge of the undulated area, smoothing occurs on the submicron level, while the characteristic appearance and smoothing of larger structures is more pronounced in the center.

#### *Dendritic areas*

This morphological feature can be described as a large coherent area with a sharp border resulting in shapes which are reminiscent of fractals, tree leaves or snowflakes. This similarity inspired the name “dendritic areas”. On electrode surfaces affected by several oscillatory discharges, these areas are distinctly visible in bright-field OM due to their higher brightness compared to other areas of the electrode, and is even more apparent in dark-field observation mode (cf. **Figure 3.5.1A**) indicating the increased scattering ability of these areas. Dendritic areas are sharply delineated at their boundary at the micrometer and even sub-micrometer scale, as evidenced by atomic force micrographs (see e.g. the inset of **Figure 3.5.6**). The interior of these areas exhibits an increased roughness. High resolution AFM imaging reveals characteristic dimensions in the range of 100 to 200 nm.

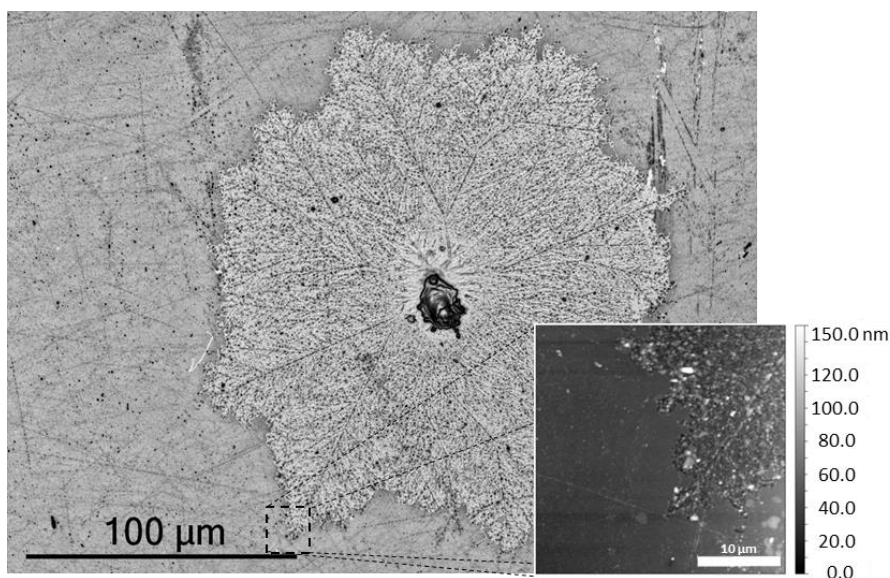


**Figure 3.5.6** CLSM image of an isolated dendritic area around a central crater. The inner structure of the image was enhanced by post-processing. Inset: AFM scan around the border of a dendritic area. Notice the sharp border and the fractal-like behavior (SDG A).

Single craters or clusters of craters, on electrodes subjected to several oscillating discharges, are always accompanied by dendritic areas, but dendritic areas without central craters may also be present in smaller amounts. When dendritic areas appear isolated from other features they are roughly circular in shape (**Figure 3.5.6**).

#### *Prolonged sparking*

When the number of sparks ignited between the electrodes increases, the well discernible areas shown in **Figure 3.5.1-Figure 3.5.6** are replaced by an apparently evenly eroded surface as shown in **Figure 3.5.7A**. **Figure 3.5.7A** shows the surface of a Ni electrode

exposed to 100 sparks. In general, the surface has a solidified molten character covered with numerous deepened spots.

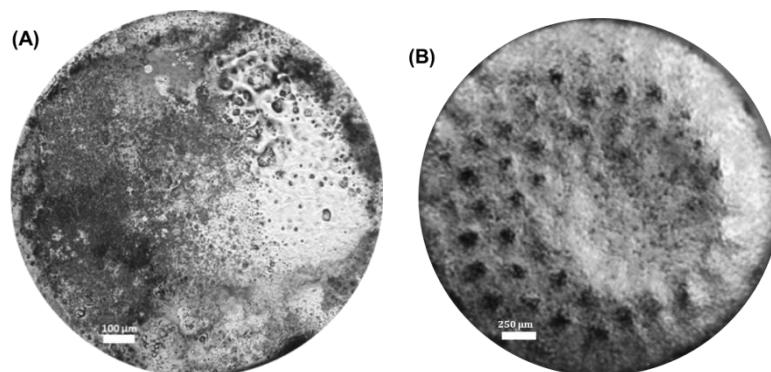


**Figure 3.5.7** Optical micrograph of the surface on an initially anodic Ni electrode exposed to 100 sparks (SDG A) (A) and after prolonged sparking (ca.  $2.4 \times 10^6$  sparks, SDG D) (B).

When increasing the number of sparks into the millions – i.e. continuously operating the SDG for several hours – the morphology of the surface evolves further and a remarkable erosion pattern appears. As shown in **Figure 3.5.7B** for the case of a Ni electrode, the surface is covered by ordered, small diameter, circular protrusions. The pattern appeared to be consistent in its configuration, even after several subsequent experimental runs. Similar patterns form on electrodes from a number of metals exhibiting material-dependent features in their appearance and morphology as shown in **Figure 3.5.8**.

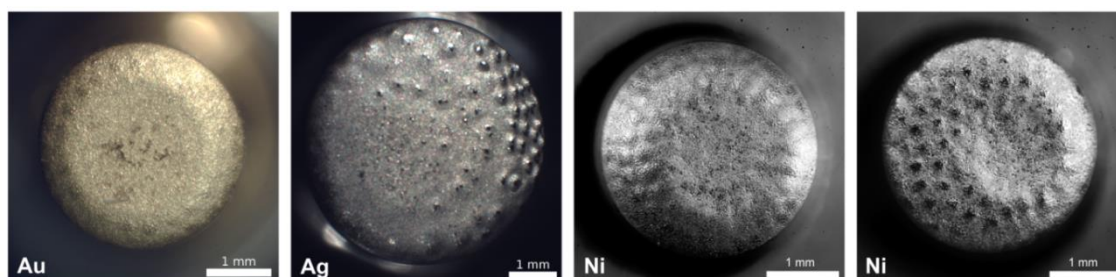


**Figure 3.5.8** Optical micrographs of the erosion at initially cathodic Au, anodic Ag, cathodic Ni and anodic Ni electrode front surfaces after prolonged sparking (ca.  $2.4 \times 10^6$  sparks, SDG D).

### 3.5.3 Formation of morphological features on the electrode surface

As it was shown earlier, the electrode surface is dominated by craters. The morphology of craters bears a striking resemblance to those reported for metal surfaces exposed to vacuum arcs [132,133] and high-pressure spark discharges [134]. This similarity, despite of the different discharge conditions, suggests a common formation process for these craters. The process briefly summarized below has been suggested by Jüttner for craters formed in vacuum arcs [135]. In the beginning, the incident ions of the discharge channel heat the electrode surface at the channel's contact point and form a molten pool. The ion pressure deforms and forces the molten material radially outwards, forming the central

depression as well as a molten rim. At some point, the discharge channel may not be maintained in the center of the crater and is transferred to the rim, due to the high field strength at local micropoints. A similar process has also been proposed for high pressure spark discharges [134].

In contrast to craters produced by vacuum arc discharges, the craters observed on polished nickel electrodes subjected to a single-spark mostly do not form coherent chains of overlapping craters. While overlap may occur, the majority of the craters are scattered over the surface. The scattered crater distribution could be the effect of an oxide layer on the electrode surface. For vacuum arcs, it has been reported that the presence of an oxide layer as thin as a few nanometers may induce a transition of the typical chain-like configuration (the so called “type 2” craters [136]) towards scattered craters (“type 1” craters) [137]. As the formation of a thin oxide layer may only be prevented by meticulous cleaning, handling and sparking the electrodes in an ultra-clean atmosphere, oxide layer will always be present on electrodes used in SDGs. The above-mentioned effect is especially important in single-spark experiments, where an oxide layer or contaminants are practically always present on the electrode surface. During prolonged sparking, however, the electrode surface can “self-clean” itself and transition from type 1 to type 2 craters may occur [138].

The diameter of craters produced in vacuum arcs was shown to correlate with the arc current [135]. Therefore, the largest craters in an oscillatory discharge are likely to be formed during the first half-cycle, where the current is the highest. This explains neatly why we found somewhat larger craters on initially cathodic electrodes.

The presence of hundreds of craters after a single spark discharge of about 3-6  $\mu$ s duration comes as a surprise. The formation of multiple craters was shown for atmospheric pressure oscillatory spark discharges [134,139], but the authors did not report high crater number. One possible explanation might be the multi-spark nature of previous investigations. As the electrodes are usually removed from sparking setups after thousands or even millions of sparks only, their surfaces are usually fully covered with craters, obscuring the identification of the number of individual craters produced by a single oscillatory discharge.

The rather high current (in the order of hundreds of amperes or even beyond) existing in spark discharges could also have a contribution to the exceptionally large number of craters. It was an early observation that the transition from a single crater to multiple craters correlates with the current increase in arc discharges [140]. Due to the very low resistance of the discharge loop of the SDG, peak currents in the order of several hundred amperes can be reached (see Section 3.1.1), which is well above the typically few amperes threshold currents associated with the transition from a single arc crater to multiple craters [140]. In order to investigate the role of the peak current on crater number, the SDG circuitry was modified by adding an extra of ca. 40  $\Omega$  resistance to the discharge loop, which resulted in strongly damped oscillations, characterized by only

three half cycles. Concomitantly, the peak current also decreased significantly from ca. 500 A to about 10 A.

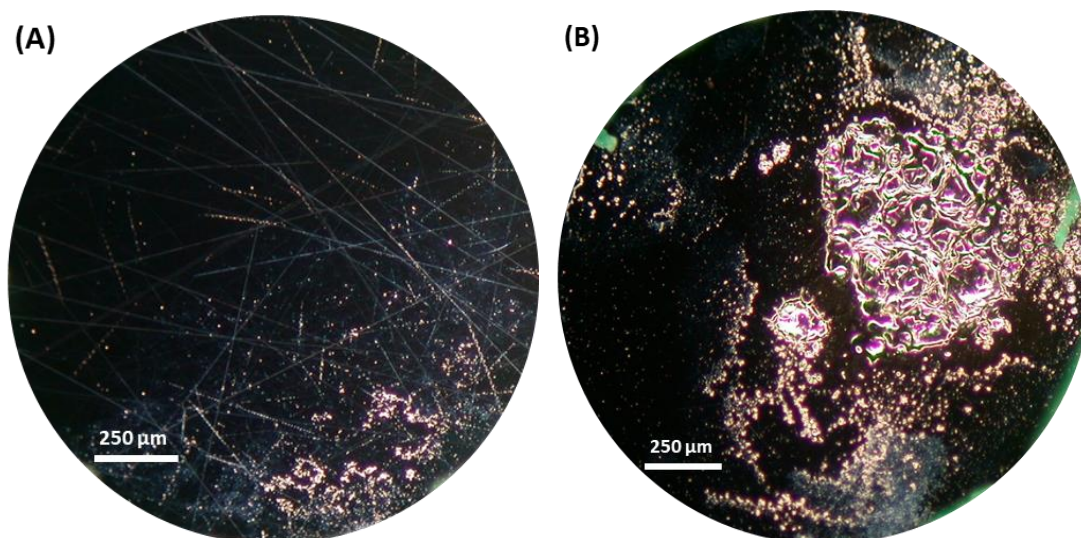


**Figure 3.5.9** Dark-field optical micrograph of an initially cathodic nickel electrode subjected to a single oscillatory spark with (A) and without (B) the extra 40  $\Omega$  resistor (SDG A).

The surface of an initially cathodic nickel electrode after a single spark with and without the added extra resistance is shown in **Figure 3.5.9A** and **Figure 3.5.9B**, respectively. The addition of the extra resistor to the discharge loop drastically reduces the number of craters, as well as the size of the largest craters. This proves, qualitatively but convincingly, that the peak current plays an important role in crater formation.

In case of the high resistance circuit, it is easier to recognize the difference between the initially anodic and cathodic electrodes, namely that the number of craters is higher on the initially cathodic electrode. As a direct consequence of this, in a few cases, no craters at all were observable on the initially anodic electrode. This is in line with observations of the undamped discharge, where a slight polarity dependence was observed in case of the largest craters. More specifically, the maximum crater diameter on the initially anodic electrode was found to be larger, while the number of craters in the spot associated with the first current half-cycle was smaller. Brewer and Walters also reported on polarity-dependence of crater formation. They attributed large, low-count craters to the anodic polarity and diffuse larger-count craters to the cathodic electrode [139].

As it was shown in **Figure 3.5.4**, crater formation is accompanied by the ejection of micrometer-sized molten droplets, some of which solidifies at the rim of the craters. This phenomenon is known to occur also during the laser ablation of solid materials [141,142] and it is also the likely source of micrometer-sized spherical particles, the so called splashing particles reported to be present in aerosols produced in SDGs [46,85]. It is plausible to assume, that the electrode material influences the occurrence and size distribution of splashing droplets. The number concentration of the ejected droplets is typically low [46], which hinders the precise measurement of the size distribution of splashing particles. Therefore, the experimental determination of the correlation between

the size distributions of craters and droplets is difficult. Therefore we must rely on hydrodynamics when qualitatively state that larger craters as well as a higher surface tension and viscosity of the melt are expected to lead to the ejection of larger droplets.

The increased resistance not only affects the number and the size of the craters, but also the formation of additional surface features. Undulated areas seen in the low resistance case are practically missing when the resistance is high (cf. **Figure 3.5.9A** and **Figure 3.5.9B**). This is in line with our observation that in the low resistance case undulated areas were found to coincide with the largest craters formed by a single oscillatory discharge (cf. e.g. **Figure 3.5.5**, **Figure 3.5.9B**). If the individual sampling sites are spread all over the electrode surface, and hence the effect of each current half-cycle is distinguishable (as in **Figure 3.5.1A**), it becomes obvious that only a single undulated area forms per oscillatory event. The fact that large craters are affected by the area's smoothing effect suggests that the process that results in undulation proceed in parallel or after crater formation, during the first half-cycle, which represents the highest energy point of the entire spark event and hence the biggest thermal load. Therefore, undulated areas are likely to form as a "side-effect" of the formation of the largest craters due to melting and then the re-solidification of surrounding regions.

When the peak current was further decreased, i.e. complementing the addition of the 40  $\Omega$  resistance with a smaller electrode gap, the crater number became even lower (ca. 5 miniscule craters). However, dark-field optical microscopy revealed that dendritic features are still present along pre-existing grooves on the surface. This indicates that the formation of dendritic areas requires a low discharge energy density. Such a behavior can also be spotted on the electrode surface subjected to an oscillatory discharge without added resistance. Its presence at the perimeter of individual circular sites (c.f. **Figure 3.5.1A**) is also in line with a low threshold energy density. Apparently, the energy (density) necessary for the formation of dendritic areas is lower than what is needed for the formation of undulated areas. As it was shown in the inset of **Figure 3.5.6**, dendritic areas comprise of a rough surface structure with typical sizes on the sub-micrometer scale. **Figure 3.5.10** shows AFM measurements performed on these sites reveal nanometer-sized substructures within the dendritic area. These nanostructures protrude from the smooth, flat electrode surface and exhibit a sharp boundary. The sharp, fractal-like border of the dendritic areas can be explained by the deposition of vapor or ejected molten nanoparticles, similarly to those observed in the case of epitaxial growth of metal layers and attributed to diffusion-limited aggregation of particles and atoms [143].

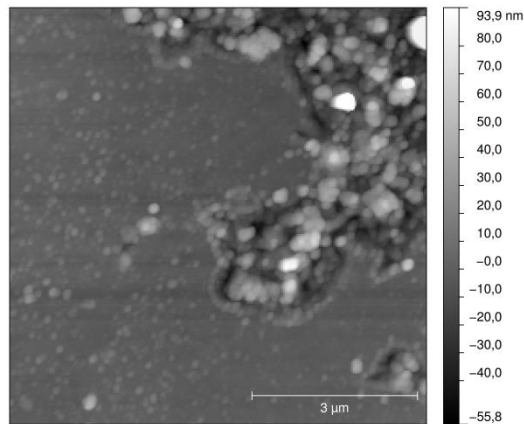


**Figure 3.5.10** AFM image of the border of a dendritic area (SDG A). Please note that the vertical scale of the image proves that dimension of the structures perpendicular to the surface is in the order of 100 nm.

As it was shown in **Figure 3.5.7B**, the surface features described above evolve into ordered patterns when increasing the spark numbers into the millions. The formation of patterns on surfaces subjected to electrical discharges has been reported for glow discharges, arc discharges and dielectric barrier discharges [144–147]. A considerable amount of work towards the modelling of pattern formation can also be found in the literature, with regard to both for the generalized process [148,149] as well as for certain special electrical discharges [150–152]. The patterns described therein are diverse and comprise regular arrangements of dots [144], lines [153] and concentric circles [145]. As it has been pointed out by Benilov in his recent review [154], regular patterns of multiple spots, such as those found on the electrodes of certain glow discharges and ambient-gas arcs, corona discharges and dielectric barrier discharges, are produced by self-organization. Trelles has recently reported non-LTE simulation results for arc discharges in the *pin cathode - plane anode* configuration [152] and found that the anode pattern formation is strongly affected by the current, as well as the anode cooling. The number, size and location of the spots was found to be markedly current-dependent. An increasing lack of symmetry in the arrangement of spots was observed for decreasing currents and increasing cooling. In SDGs, the peak current is typically very high (several hundreds of amperes) and there is no water cooling applied to the electrodes, hence a very consistent spot pattern can be expected, which is in line with the observations presented here (cf. **Figure 3.5.7B**). Trelles suggested that the pattern formation is due to an imbalance between the heat lost by the heavy species to the electrode and current transfer by electrons. It was also stated that the presence of competing processes is a common characteristic of self-organization phenomena [152,154].

The electrode surface patterns obtained in our experiments bear striking resemblance to those found in arc and glow discharges [135], suggesting similar formation mechanisms. What makes the generalization of the processes behind different types of discharges not trivial, is the marked difference between the highly localized and transient phenomenon of the spark discharge produced in an SDG and the stationary nature of the

arc and glow discharges. A further difference is that the direction and amplitude of the current is rapidly changing and the electrodes typically have identical shape and an axisymmetric arrangement in the SDG. Each and every spark only affects a part of the electrode surface, as is obvious from the results of the single-spark experiments shown above. This suggests that each spark event contributes only a small portion to the whole pattern, which is further evidenced by the fact that the electrode pattern begins to emerge only after a large number ( $10^5$  to  $10^6$ ) of spark events. These considerations suggest that despite the similarity of the surface patterns, a more complex mechanism may govern the pattern formation in SDGs, which requires additional experimental and theoretical work in order to be revealed. Such a study is beyond the scope of the present dissertation.

### 3.5.4 Energy demand of crater formation

The description of surface erosion features provided in the previous sections prove that the electrode erosion in an SDG, even under the influence of single sparks, is a complicated process that cannot be expected to be adequately described by a single spark-single crater model. Still, the Jones model [81], which is considered to be the standard spark erosion model within the SDG community, does exactly that. In an effort to give a better characterization, I carried out a statistical evaluation of crater data and estimated the energy demand of crater formation, the dominant erosion process.

As it was shown, craters have a roughly circular central depression surrounded by a protruding rim of distinctly post-molten (i.e. re-solidified) appearance (**Figure 3.5.3**). By comparing the volumes of the depression to that of the material protruding above the surface around the rim, I estimated that the volume of material deposited on and missing from the electrode are similar within measurement uncertainty. This suggests that during crater formation the electrode material is mostly displaced on the electrode surface and only a small fraction of it is actually removed (evaporated). This finding is in line with the literature: studies on spark switches and arc spots reported very low energy efficiency of material removal [155–157].

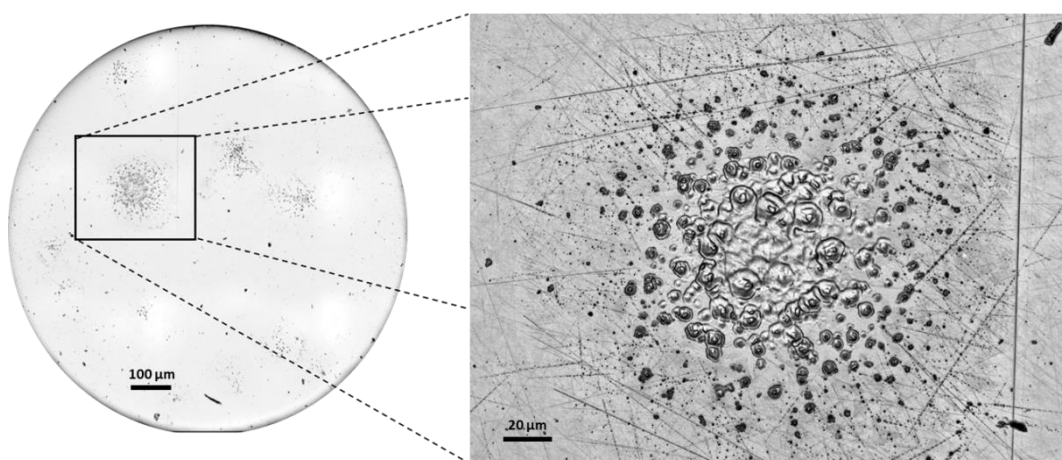


**Figure 3.5.11** CLSM image of the surface of an initially cathodic Ni electrode after a single spark (in case of low circuit resistance) (left). The biggest affected area on the surface, associated with the first half cycle of the current waveform is enlarged (right) (SDG A).

It can be qualitatively seen in **Figure 3.5.11** that crater sizes range from few tens of micrometers down to submicron sizes, with micrometer-sized craters being the most abundant. This was quantified by measuring the size-distribution of craters at the *largest erosion-affected spot* (associated with the first half cycle of the discharge) of the electrode surface after subjecting it to a single spark (i.e. the area shown in the right panel of **Figure 3.5.11**). Please note, that the crater diameter is defined here as the diameter of a circle which has the same area as the ellipse that can be fitted to the central depression of the crater (i.e. “equivalent crater diameter”). The depth of the craters is defined as the height difference between the deepest point of the crater and the overall (plain) level of the surface, measured by AFM and CLSM.

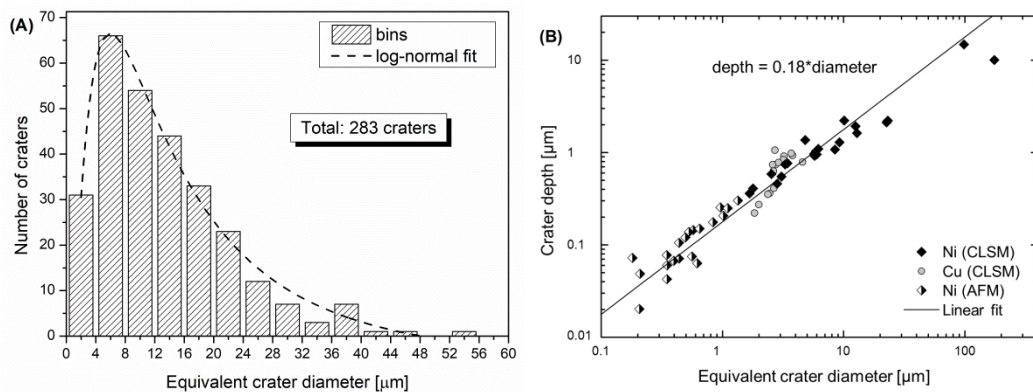


**Figure 3.5.12** The size distribution of craters produced by the first half cycle of a single spark on an initially cathodic Ni electrode (A). The depth of craters as a function of their diameter as measured by CLSM and AFM, both on Ni and Cu electrodes. Due to the wide diameter range the data are presented on logarithmic scales (B) (SDG A).

As shown in **Figure 3.5.12A**, the size distribution of craters on Ni electrodes follows a log-normal distribution with a modal diameter of approx. 6  $\mu\text{m}$ . It was also established that there is a linear relationship between the depth and the diameter of the craters (the depth-to-diameter ratio is ca. 0.18), for both Cu and Ni electrodes, as can be seen in **Figure 3.5.12B**. As it was alluded to previously, the depression of craters have a hemi-ellipsoid shape. Based on the data for the craters counted here, their volume can be approximated as  $0.062(\text{diameter})^3$ . By utilizing this generalized volume formula, the energy needed during the first half-cycle to melt the material which corresponds to the volume of a single crater having a diameter  $d$  (in meters), including radiation and conduction losses, can be calculated from the energy balance (**Equation 3.5.1**). Please note, that this calculation somewhat underestimates the total amount of molten material since it is possible that some of the molten material solidifies back at the bottom and on the walls of the crater, therefore not accounted for when the volume of the depression is calculated.

$$E = 0.062\rho d^3(c_s(T_m - T_c) + H_m) + 0.5\pi d^2\sigma\tau(T_m^4 - T_c^4) + \pi dk_e\tau(T_m - T_c) + \pi dk_g\tau(T_m - T_c) \quad (3.5.1)$$

where  $\rho$  ( $\text{kg m}^{-3}$ ) is the density of the solid electrode material,  $c_s$  ( $\text{J K}^{-1} \text{kg}^{-1}$ ) is the heat capacity of the solid electrode material,  $\tau$  (s) is the duration of energy input (which, in the present case, was taken as the length of a half-cycle, namely 250 ns),  $k_e$  and  $k_g$  ( $\text{W m}^{-1} \text{K}^{-1}$ ) are the thermal conductivity of the electrode material and carrier gas, respectively,  $T_c$  and  $T_m$  (K) are the temperatures of the carrier gas and the melting point of the electrode material, respectively,  $H_m$  ( $\text{J kg}^{-1}$ ) is the enthalpy of melting of the electrode material, and  $\sigma$  ( $5.67 \times 10^{-8} \text{ W m}^{-2} \text{ K}^{-4}$ ) is the Stefan–Boltzmann constant.

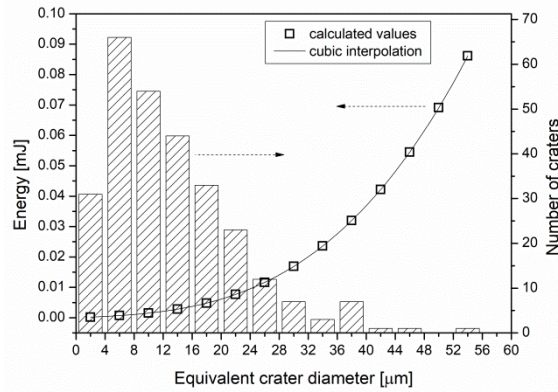


**Figure 3.5.13** The size distribution of craters (right vertical axis) and the energy needed to melt the electrode material corresponding to the volume of a crater of a given diameter (left vertical axis) (SDG A).

**Figure 3.5.13** shows that the energy needed to melt a volume of the electrode material corresponding to the volume of a crater (as calculated from **Equation 3.5.1**) steeply increases with crater diameter. This actually can be expected, as the crater volume increases with the cube of the diameter. It can also be added that the energy plot in **Figure 3.5.13** has an almost perfect cubic shape, which suggests that within the studied domain the first term is dominating in **Equation 3.5.1**. This means that the radiative and conductive cooling (represented by the second, third, and fourth terms in **Equation 3.5.1**) of the heated volumes is negligible during the ca. 250 ns period of the first half-cycle. The cubic dependence also indicates that the smallest craters, which dominate the surface in number, have only a minor contribution to the total energy needed for melting the material that reside in all of the craters generated during the first half-cycle (cf. **Figure 3.5.11**). The formation of bigger and medium-sized craters however consumes considerably more energy which, despite their relatively small number, makes them more important from an energetic point of view. This is in line with the qualitative difference observed between the low and high resistance circuit cases (cf. **Figure 3.5.9**). Namely, by increasing the resistance of the discharge loop, the peak current and hence the spark energy is decreased drastically and consequently only small craters are able to form on the electrode surface.

From the data presented in **Figure 3.5.13** the total energy needed to produce all the craters shown in the right panel of **Figure 3.5.11** can be estimated. By summing up the product of the energy needed to melt the volume of a crater and the number of craters having a certain size, total energy demand calculated to be about 1 mJ. The energy stored in the capacitor during these single-spark experiments prior to sparking was about 300 mJ, but only a small portion of it is dissipated during the first half cycle of the process. I estimated from the instantaneous current, measured in the SDG having low resistance discharge loop, by **Equation 3.1.4** that this portion is about 5 mJ, which is pumped into both electrodes resulting in an energy input of roughly 2.5 mJ per each electrode. This agrees fairly well with the calculated 1 mJ value, especially if we consider, that *i*) it is impossible to count and measure all the craters on the surface and *ii*) the volume of the depressions is only a lower limit of the actually melted volume, both of which resulting in the underestimation of the energy demand of crater formation; moreover *iii*) other morphological features (i.e. undulated and dendritic areas) also require some energy to form. So within the limits of this simple qualitative model it can be concluded that the formation of the surface structure shown in **Figure 3.5.11** can be fairly well explained by thermal processes (most dominantly melting) driven by the electrical energy of the spark. Also, as evidenced by the measurement of the volume of the displaced material on the surface and the mass loss of the electrodes, only a small fraction of the electrode material actually leaves the electrode surface and serves as the source of subsequent NP formation process.

## 3.6 Implications on the generated nanoparticles

### 3.6.1 Experimental

The NPs formed from the spark-eroded vapor was investigated by employing *in-situ* and *ex-situ* techniques. The integrated effect of spark erosion on the electrodes was investigated by measuring the mass loss of the electrodes as a result of sparking. This, gravimetric method requires the precise measurement of the mass of the electrodes prior to and after sparking. In my experiments the electrodes were thoroughly cleaned with ethanol and wiped dry with low-lint wipes before using a semi-micro analytical balance (Mettler Toledo, Model AB135-S/FACT) in order to measure their mass with a precision of 10  $\mu\text{g}$ . Each experiment consisted of typically two hours of sparking at  $SRR=100$  Hz in order to increase the erosion effect on the electrodes hence ensuring that the mass-changes are well above the detection limit of the instrumentation used.

The aerosol NPs generated in the SDG were sampled by using a low-pressure impactor. A rotary pump was used to maintain a pressure of 5-8 mbar in the impactor chamber, where a TEM grid was placed in the path of the aerosol flow formed by an orifice. The nanoparticles are deposited onto the TEM grid due to their inertia. The deposition time, and hence the concentration of the particles over the grid, was controlled by a shutter in front of the aerosol jet. The deposited NPs were characterized by TEM (FEI

Tecnai G2 20 X-TWIN). Size distribution of singlet particles was constructed by the Fiji (ImageJ) image processing software.

For the *in-situ* characterization of the generated NPs the SDG was connected to one of two scanning mobility particle sizer (SMPS) setups. SMPSs are widely used tools of aerosol science for the in-flight classification and concentration-measurement of gas-borne particles [9]. These instruments are based on the measurement of the electrical mobility of aerosol particles. Initially, electrical mobility techniques were used to measure ions in gases [158] which was followed by the sizing of aerosol particles based on their electrical mobility [159]. The same working principle has several technical realizations, but all of them are centered around two main parts, namely the electrostatic classifier and the particle counter. The electrostatic classifier is used to classify charged particles<sup>7</sup> according to their electrical mobility. The most widely used classifier type is called differential mobility analyzer (DMA) DMAs consist of two concentric electrodes with a given polarity. The aerosol particles are introduced into the electric field defined by the electrodes and will travel through the DMA according to their electric mobility. By adjusting the voltage between the two electrodes particles with a given mobility can be selected and led out the system via an exit slit. Because the electric mobility is a function of the particle size, this method leads to the selection of a monodisperse particle flow. The size of the selected particles can be deduced from their mobility by using inversion algorithms [160], and their concentration can be measured by using a particle counter [9]. When the particle concentration is high, usually a Faraday cup electrometer is used to measure the particle number concentration. These electrometers are based on the collection of the selected charged particles on high-efficiency filters and the measurement of the induced current, from which the total particle number concentration can be estimated [9]. Lower concentrations (in principle down to single particles) can be measured by using condensation particle counters (CPCs). CPCs are based on the optical detection of particles, therefore the measurement of nanoparticles requires the condensation of a vapor of a working fluid onto the sample particles to be detectable [161].

In my experiments, either a Grimm Aerosol Technik GmbH SMPS-C model or a custom-made SMPS setup, constructed from a particle charger containing a  $\beta$ -emitting  $^{63}\text{Ni}$  source, a dynamic mobility analyzer (DMA, TSI 3081) and an electrometer was used (see **Figure 3.6.1**). Either of these setups allows for the measurement of the concentration of NPs of a given size, selected by the DMA, based on the electrical mobility of the aerosol particles. By scanning the SMPS over a predefined mobility diameter range, the size distribution of the NPs was derived.

---

<sup>7</sup> Usually a so called particle charger, or neutralizer is used to set a well-defined charge distribution of the particles.

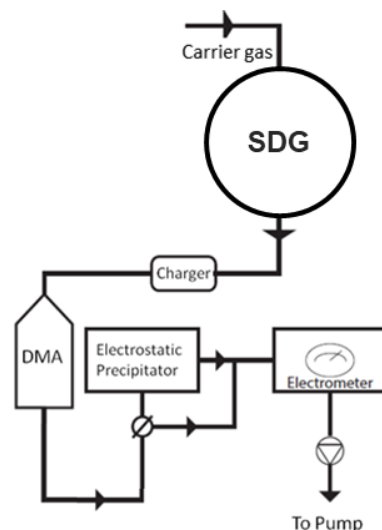


**Figure 3.6.1** Schematic representation of the SMPS system used for in situ characterization of the nanoparticles generated in SDG C.

### 3.6.2 Electrode erosion

The initial step of nanoparticle formation in the SDG is the production of an atomic plume as a result of the erosion of the electrode material due to sparking. On one hand, the NP yield of the SDG depends on the amount of the eroded material, while on the other, the number of atoms produced, as well as the volume of the atomic plume, strongly influences the size of the primary particles [77].

The amount of the eroded material and hence the atomic vapor is usually approximated by the mass-loss of the electrodes subjected to prolonged sparking as measured by gravimetry [46]. All the material eroded from the electrodes not necessarily turns into atoms and nanoparticles but this easily measurable quantity well describes the erosion properties of different electrode materials or the dependence of erosion on the process parameters, such as the spark energy.

It has been demonstrated that the erosion rate, i.e. the eroded mass per spark of a given electrode material increases with increasing the energy stored in the capacitor, irrespectively whether the latter is realized via changing the breakdown voltage or the capacitance [46]. It follows that the mass of the eroded material and hence the NP yield of a given SDG can be tuned via the stored energy. This however is only true when the resistance of the discharge loop is fixed. **Figure 3.6.2** exemplifies the mass loss of Au electrodes subjected to prolonged sparking in an SDG of varying total resistance under otherwise identical experimental conditions. It was shown in Section 3.1.1 (see **Figure 3.1.2**) that the total resistance ( $R$ ) does not affect the breakdown voltage resulting in practically constant stored energy. In contrast to this, the mass of the eroded material drastically decreases when the resistance of the discharge loop increases. By increasing the total resistance from  $1 \Omega$  to  $2 \Omega$ , the mass loss and hence the NP yield drops by a factor of 1.5 (cf. **Figure 3.6.2**).

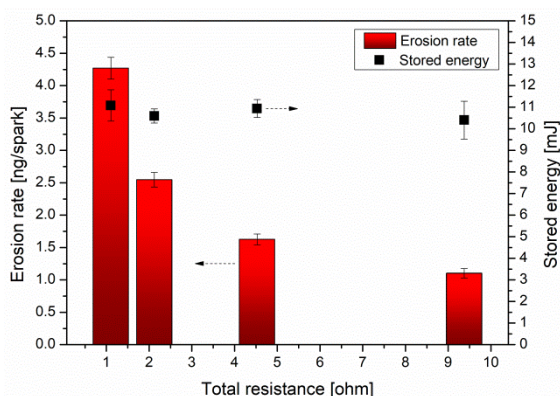


**Figure 3.6.2** Erosion rate of Au electrodes at varying total resistance (columns) and the variation of the energy stored in the capacitor (squares) (1 mm gap, 2 hours of sparking at 100 Hz in Ar atmosphere, SDG A).

The results shown in **Figure 3.6.2** prove that the resistance of the electrical components of the SDG has an important effect on the NP production, even if the stored energy remains unchanged. This result provides an additional proof and further strengthens my previous statement, namely that the energy stored in the capacitor, as defined by **Equation 3.1.2**, does not represent properly the energy dissipated in the gap. As it was previously suggested, the dissipated energy should be calculated from the instantaneous current and the spark resistance as defined by **Equation 3.1.4** instead. In general,  $R_{spark}$  is unknown in an SDG, and it is also challenging to measure. As an alternative, several theoretical models exist from which its value can be estimated [107]. According to these models,  $R_{spark}$  depends on the instantaneous current therefore the variation of the total resistance also affects the spark resistance via the current (cf. **Figure 3.1.2**). Under the conditions investigated in **Figure 3.6.2**,  $R_{spark}$  varies by less than 50%, while the integral of the square of the current (cf. **Equation 3.1.4**) changes by more than an order of magnitude. It follows that although the exact value of  $E_{spark}$  cannot be calculated, its variation is dominated by the integral of the square of the current. In order to illustrate these effects, the erosion rate values shown in **Figure 3.6.2** are plotted as a function of the integral of the square of the current (see **Figure 3.6.3**).

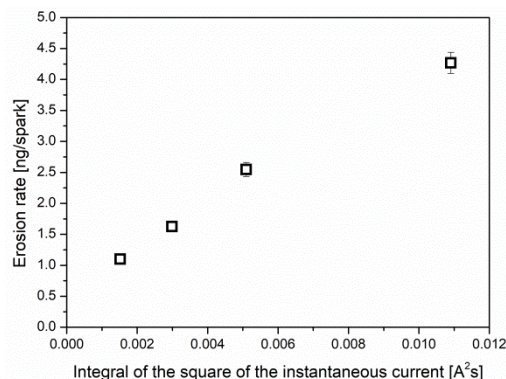


**Figure 3.6.3** Erosion rate of Au electrodes at varying total resistance as a function of the integral of the square of the instantaneous current measured in the spark gap (1 mm gap, 2 hours of sparking at 100 Hz in Ar atmosphere, SDG A).

**Figure 3.6.3** clearly shows a strong correlation between the material erosion rate and the electric current, proving that the energy dissipated in the gap, hence determining the material erosion, should be calculated from the instantaneous current.

The above considerations can be summarized as follows: *i)* electrode erosion can properly be described by the spark energy calculated from the measured current waveform; *ii)* the stored energy is only adequate for describing the material erosion in an SDG qualitatively if the resistance (as well as the inductance) of the discharge loop is fixed. These findings have the practical consequence that stored energy values cannot be reliably used to compare the erosion properties of different SDG setups, hence it either has a qualitative meaning or the other electrical parameters ( $R$ ,  $L$ ,  $C$ ) of the circuit have to be specified. Also, special care should be taken during the operation of an SDG in order to keep the  $R$  and  $L$  value of the discharge loop fixed. It must be noted, that the resistance of the discharge loop can easily be achieved, in the range exemplified in **Figure 3.6.2**, by using lower quality or longer cables or even loose contacts, which might be overlooked and still result in the significant variation of the erosion rate.

The erosion rate of different electrode materials can be very different. **Figure 3.6.4** shows the mass loss per spark for four electrode materials obtained under identical experimental conditions. As can be seen in **Figure 3.6.4** from four electrode materials typically used in SDGs copper has the lowest, while gold has the highest erosion rate. The different erosion rates of materials exposed to electrical discharges is a well-known phenomenon [162,163], but the material properties that are responsible for the experimentally obtained differences are not fully understood.

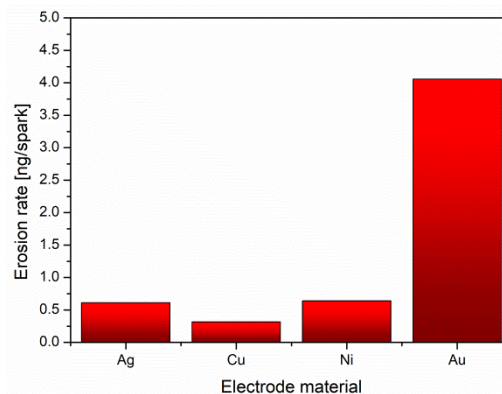


**Figure 3.6.4** Erosion rate of Ag, Cu, Ni, and Au electrodes (1 mm gap, 2 hours of sparking at 100 Hz in Ar atmosphere, SDG A).

Several erosion models have been tested in the literature to explain the differences in the measured erosion rates, including the theory of sputtering, ejection of molten droplets, or the evaporation of the electrode material [134]. The electrode erosion in an SDG is usually described by the simple model of vaporization of the electrode material in a small spot created by the spark plasma channel [17,24,46,77]. By assuming that the energy delivered by the spark channel is in balance with the energy output represented by thermal conduction and radiation, the mass evaporated from such a spot can be calculated,

which is the bases of the so-called Jones-model [81]. The Jones-model requires an experimentally determined energy-efficiency factor for fitting the measured mass-loss, which has a remarkably low value – in the order of 0.1% – in case of a traditional SDG [77]. By incorporating the energy efficiency factor (as well as other experimentally determined parameters) the mass derived from the energy balance gives a reasonably good estimate of the material eroded in an SDG at varying inter-electrode distances [47] and for several different electrode materials [24]. However, the highly simplified character of this approach is well reflected by the fact that it erroneously predicts the relative erosion of certain materials, e.g. gold and silver [46] and neither can explain the fundamental basis of the energy-efficiency factor nor its very low value.

By investigating the surface morphology of electrode surfaces I found that a high number of craters are produced by each single spark and most of the material is only melted and re-distributed on the surface which ultimately leads to the formation of self-ordered regular patterns on the electrode surfaces when the number of sparks is increased (cf. Section 3.5.2). Thus, the evaporation of the finally aerosolized material only accounts for a small fraction of the energy pumped into the electrode gap. This explains, at least qualitatively, why the Jones-model requires the incorporation of a very small scaling factor. It was also demonstrated that by decreasing the electric current and hence the energy pumped into the spark gap both the number and size of craters and the electrode erosion rate decreases (cf. **Figure 3.6.3** and **Figure 3.5.9**). Therefore it is plausible to assume that the overall material removal caused by a single spark very much depends on the actual size and number of craters, which are dependent on material properties. As a consequence, the simplification of the complex surface pattern to a single “quasi-crater” is inappropriate for all electrode materials, which means that the assumptions of the Jones-model should be refined. One aspect which should be taken into account in such a refined erosion model is the presence of a high number of craters. The number and size of craters obviously affects the total volume from which material can be released, and which also seem to correlate with the current. Another important aspect is the melting of the electrode material, which could dissipate a considerable amount of energy pumped into the electrodes, according to my results.

### **3.6.3 Particle formation**

Nucleation and formation of atomic clusters can take place in the SDG when the atomic plume generated during a single spark cools down to about room temperature, mainly due to the ceasing energy input and mixing with the carrier gas [17]. The typical temperature of the plasma during erosion, i.e. in the arc stage, is in the range of 15000-20000 K (see **Figure 3.4.2B**). In the arc stage the rather high temperature is maintained by the energy input of electric current flowing between the electrodes. The cooling of the metal vapor can commence when the current ceased, that is in the afterglow stage. The rate of temperature decrease, the so-called quenching rate, was estimated to be  $(5.5 \pm 0.6) \times 10^8 \text{ Ks}^{-1}$  by employing the Boltzmann plot method (see Section 3.4.1) on temporally resolved emission spectra acquired in a nitrogen atmosphere. This value fits

into the  $10^6$ - $10^9$   $\text{Ks}^{-1}$  range declared in the literature [77,86,164,165], and it is closer to the higher end of the reported range. Recently Feng *et al.* estimated the quenching rate in an SDG for gold vapor in nitrogen atmosphere and obtained  $7.5 \times 10^6$   $\text{Ks}^{-1}$  [77], which is almost two orders of magnitude smaller than the value I obtained. Their value was calculated by assuming that the temperature of the atomic gold vapor is around the boiling point. As a contrary, I found, by evaluating the optical emission spectrum of the spark, that the temperature is considerably higher than that, even at later stages of the spark discharge. I determined a similar quenching rate, with a value of  $\sim 3.4 \times 10^8$   $\text{Ks}^{-1}$ , in argon atmosphere by using the equilibrium plasma model described in Section 3.4.2 for calculating the temperature from time-resolved spectra. Thus, I believe that quenching rate values of about  $10^8$ - $10^9$   $\text{Ks}^{-1}$ , including my own, are more accurate estimates for the conditions existing in an SDG.

Knowing the quenching rate and the temperature at the beginning of cooling, one can estimate how long it takes the metal vapor to cool down to room temperature. This is about 25  $\mu\text{s}$  for copper atoms in nitrogen atmosphere<sup>8</sup>. This can be considered as an estimate for the end of the cooling stage, and can also be taken as the temporal starting point of particle formation. Spark repetition rate values are normally not higher than a few hundreds of Hz, which means that the repetition of spark events occur in the millisecond time range, at most. This is about 2-3 orders of magnitude larger than the typical cooling time obtained here. Therefore one can conclude that NPs have ample time in between consecutive sparks, i.e. spark events can be considered independent from the point of view of NP and cluster formation.

The seeds formed after nucleation from the metal vapor will grow further by condensation and coalesce into singlet particles that grow up to a certain size after which aggregation and agglomeration might also take place. The biggest singlet particles, formed before aggregation commences are called primary particles which will finally form NP aggregates after attaching to each other via collisions [17]. By adopting the main mechanisms relevant to particle formation (nucleation, coagulation, turbulent dilution, turbulent diffusion, laminar diffusion, aggregation) and their respective approximate time domains from Feng *et al.* [77], the approximate time-scale of NP formation can be summarized as it is shown in **Figure 3.6.5**. The schematic spectra shown at the top of **Figure 3.6.5** represent the characteristic emission spectra typical to the material erosion and the cooling phases. Due to the high (in the order of 100 mJ) energy pumped into the gap during the arc stage of the spark the spectrum is dominated by gas ions while the emission acquired in the cooling stage is characterized by atomic copper and nitrogen emission. As a result of particle growth steps (schematically shown at the bottom of **Figure 3.6.5**) aggregated Cu nanoparticles (shown in the right inset of **Figure 3.6.5**) form from the Cu atoms and ions eroded from the electrodes in the material erosion phase initiated by the spark plasma (exemplified in the left inset of **Figure 3.6.5**).

---

<sup>8</sup> At a gap size of 2 mm, 1.68 l/min gas flow rate and SRR of about 180 Hz.

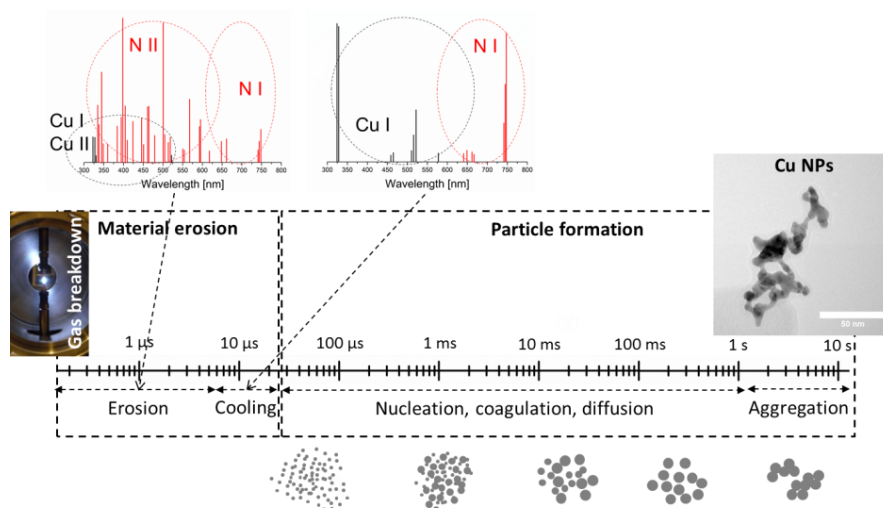


**Figure 3.6.5** Approximate time scale of NP formation in SDGs starting from the breakdown of the gap until the formation of NP aggregates. The typical spectral fingerprints of the erosion and cooling stages are shown together with the main NP formation mechanisms and time-ranges as adopted from [77]. A picture of the spark is shown in the left and a typical Cu NP aggregate is shown in the right inset.

**Figure 3.6.6A** shows a TEM image of gold NPs produced in argon gas. NP aggregates can be seen with sizes in the range of a few tens of nanometers, as well as non-aggregated, almost spherical particles having diameters of a few nanometers. These spherical singlets represent the primary particles [46]. By performing the tedious analysis of numerous TEM images of the generated gold NPs, the size distribution of the primary particles can be obtained, as shown in **Figure 3.6.6B**. The diameter of the primaries exhibits a log-normal distribution with a geometric standard deviation of 1.31 and a modulus of about 5 nm. This value agrees well with the biggest particle size of about 5-6 nm at which full coalescence, and hence the formation of singlet particles can occur at room temperature in the SDG [47].

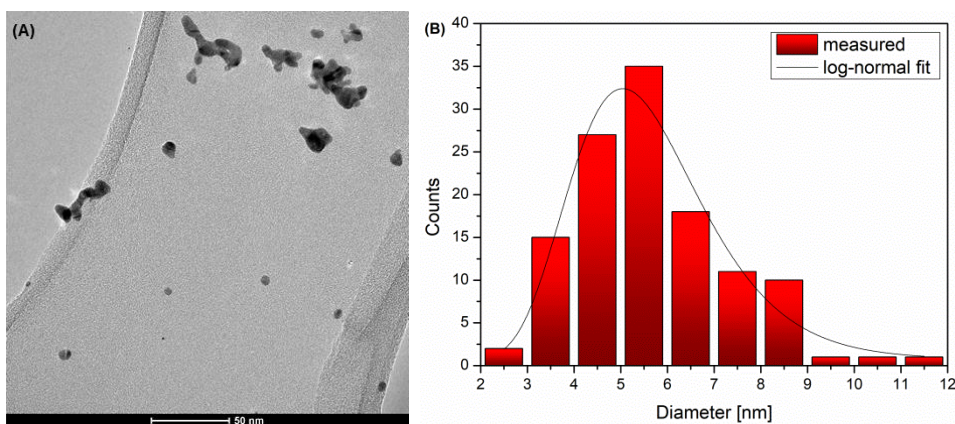


**Figure 3.6.6** TEM image of singlet and aggregated Au NPs generated in Ar atmosphere (A). Size distribution of the singlet Au NPs (B) (1 mm gap, 100 Hz SRR, SDG A).

As it is evident from **Figure 3.6.6A** the particles leaving the SDG are typically aggregated NPs. The most common way of producing spherical NPs is the compaction of the NP aggregates further downstream of the SDG by means of a tube furnace [11]. By adjusting the temperature of the furnace and the residences time of the particles inside the hot zone of the furnace even perfect compaction can be achieved at sufficiently high temperatures. **Figure 3.6.7** shows compacted gold NPs after passing SDG-generated aggregates through a tube furnace, kept at 800°C. The previously seen aggregates (**Figure 3.6.6A**) coalesce into compact, almost perfectly spherical particles with reduced sizes, having typical diameters of about 15-20 nm.

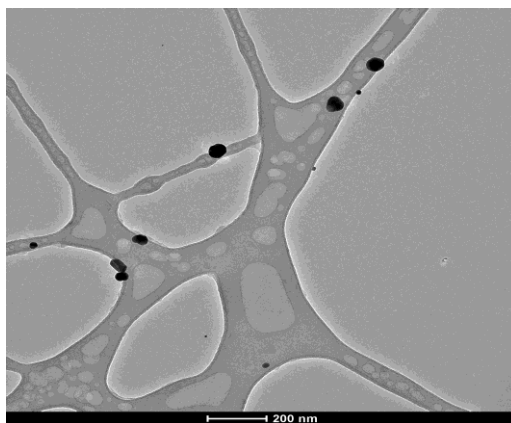


**Figure 3.6.7** TEM image of Au NPs generated in Ar atmosphere and compacted at 800°C in a tube furnace (1 mm gap, 100 Hz SRR, SDG A)

NPs generated in SDGs are usually characterized *in-situ* by their electric mobility. This allows for assigning an equivalent diameter<sup>9</sup> to each NP irrespectively of its shape [90]. This equivalent mobility diameter is measured by an SMPS (see Section 3.6.1 for details on the working principle of the SMPS). The typical size distribution of gold NP aggregates generated under nitrogen atmosphere can be seen in **Figure 3.6.8**. The NPs exhibit a log-normal distribution with a modulus of 52 nm and a geometric standard deviation of 1.70 in the particular case shown here. After passing through the NP aggregates in a tube furnace of 750°C the modal mobility diameter decreases drastically. The initial modal diameter of 52 nm shifts to 28 nm, while the geometric standard deviation also decreases from 1.70 to a value of 1.53.

---

<sup>9</sup> The electric mobility diameter of an irregularly shaped aggregate is the diameter of a spherical particle of the same material which moves in the electric field the same as the aggregate does.

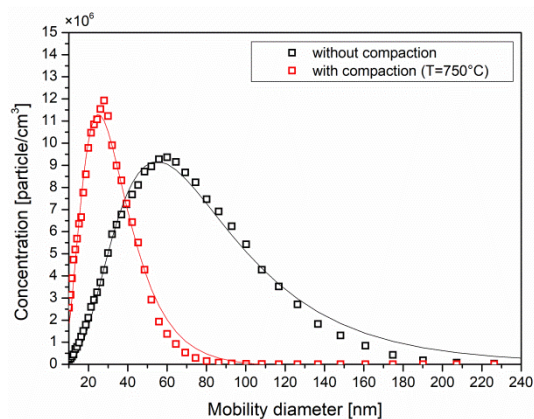


**Figure 3.6.8** Size distribution of compacted and not compacted, i.e. aggregated Au NPs generated in  $N_2$  atmosphere. The measured data are represented by squares, while solid lines indicate fitted log-normal functions (1 mm gap, 100 Hz SRR, 1 slm flow rate, SDG A).

### 3.6.4 Effect of control parameters on the generated aggregates

As it was pointed out in the previous sections the charging current and the gap size strongly affect the operation of an SDG. The effect of these control parameters on NP production (i.e. on the NP aggregates) was characterized by using an SMPS. In order to prove the generality of this approach, all experiments were performed using two electrode materials, namely Au and Cu, exhibiting rather different erosion properties (cf. **Figure 3.6.4**).

**Figure 3.6.9** illustrates the effect of charging current on the size distribution of Cu and Au NPs generated in an SDG under nitrogen atmosphere. The mobility size distribution of the NPs follows log-normal distribution at every charging current value used, with a modus in the range of 18-30 nm and 21-45 nm for Cu and Au, respectively. Both the modal diameter and peak concentration increase with increasing charging current in both cases.

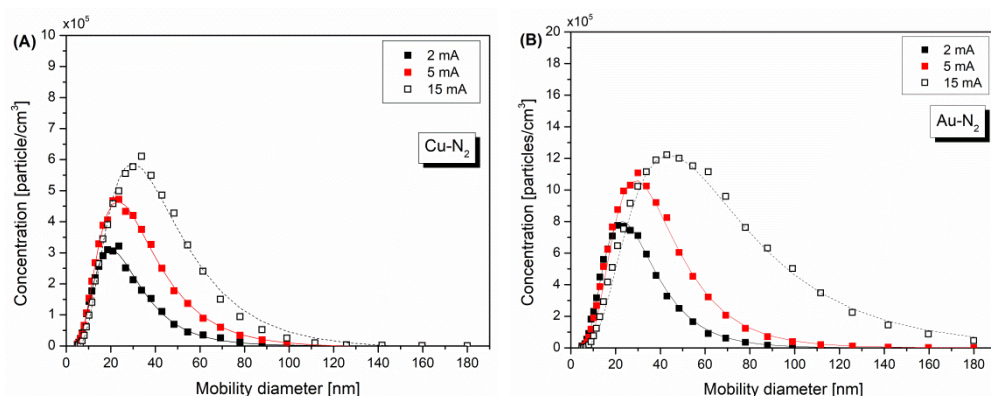


**Figure 3.6.9** Mobility size distribution of Cu (A) and Au (B) NP aggregates generated in nitrogen atmosphere at different charging currents (2 mm gap, 1.68 l/min gas flow rate). The log-normal fit of the measured data (squares) is represented by the lines (SDG C).

The tendencies shown in **Figure 3.6.9** can be interpreted by recalling the relations between the charging current, breakdown voltage, and SRR (**Figure 3.1.4**). The variation

of charging current results in the variation of the SRR (**Figure 3.1.4C**). Increased SRR produces more eroded material per second, which results in higher particle concentration, more pronounced aggregation and hence an increase in the modal diameter of the generated NPs [46,88]. This qualitatively explains the trends shown in **Figure 3.6.9**, namely that both the diameter and the concentration of the generated Au and Cu NPs increases with increasing charging current. The SRR depends more strongly on the charging current than the spark energy (cf. **Figure 3.1.4B** and **Figure 3.1.4C** which explains the overall increasing trend in the particle diameter.

The size distributions of Cu and Au NPs generated at a fixed charging current at varied gap sizes are shown in **Figure 3.6.10**. As can be seen in **Figure 3.6.10A**, at 1 mm gap the produced Cu NP agglomerates have log-normal size-distribution with a modal diameter of 34 nm. When the gap is increased to 2 mm the modus does not change, only the concentration increases. By further increasing the gap both the modus and the peak concentration shift to smaller values, down to about 19 nm modal diameter at 4 mm gap. A similar trend can be seen during the generation of Au particles (**Figure 3.6.10B**). The modal diameter of the NPs increases from about 32 nm to ~42 nm when the gap is changed from 1 mm to 3 mm and by further increasing the gap the modus of the size distribution shifts back to ~32 nm. A practical consequence of this behavior is that, as opposed to the case of charging current, the gap size variation cannot be used to monotonously tune the size of the NPs generated in the SDG.

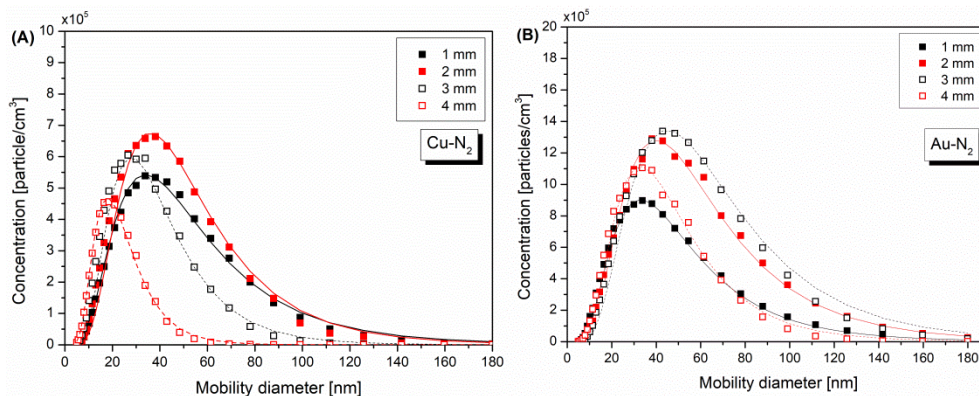


**Figure 3.6.10** Mobility size distribution of Cu (**A**) and Au (**B**) NP aggregates generated in nitrogen atmosphere at different gaps (10 mA charging current, 1.68 l/min gas flow rate). The log-normal fit of the measured data (squares) is represented by continuous lines (SDG C).

When varying the gap size at a fixed charging current, both the SRR and the spark energy change significantly. As it can be seen in **Figure 3.6.10**, the diameter and the concentration of the generated NPs reach a peak value and start to decrease when the gap size is increased for both Cu and Au electrodes. This behavior reflects the combined effect of the variation of the SRR and the spark energy at different gaps as shown in

**Figure 3.1.4B** and **Figure 3.1.4C**<sup>10</sup>. The spark energy strongly increases with increasing gap, while the SRR decreases. The bigger the gap and hence the higher the energy per spark the more material is eroded from the electrodes [46], which is expected to increase the vapor concentration and hence the NP concentration in the gap. This is well reflected in the size distributions measured at 1 mm and 2 mm gaps for Cu, and in the gap range of 1-3 mm for Au (cf. **Figure 3.6.10**). However at bigger gaps, despite the increased erosion rate caused by the higher energy per spark, the opposing effect of the decreasing SRR (cf. **Figure 3.1.4C**) starts to dominate, which decreases the total particle concentration. The above findings are in line with the results obtained by optical emission spectroscopy, namely that after a certain energy value the vapor concentration increases less effectively (see **Figure 3.3.10**). As it is indicated in **Figure 3.1.4B**, the ca. 300 mJ threshold energy for Cu (cf. **Figure 3.3.10A**) is reached when the gap is increased from 2 mm to 3 mm. This optimum gap size value correlates well with the peaking of the total concentration (and the diameter) of the generated particles – as measured by the SMPS – which started to decrease between 2 mm and 3 mm gap sizes despite of the monotonously increasing spark energy (cf. **Figure 3.1.4B**). An analogous behavior was observed for Au (cf. **Figure 3.3.10B**), with the sole exception that for gold the threshold energy is about 600 mJ, and corresponds to a gap of 3 mm, correlating neatly with the peak concentration and the modal diameter of the generated Au NPs (cf. **Figure 3.6.10B**). Although the amount of metal vapor eroded in unit time cannot be directly translated to the total particle concentration or diameter, they are related to each other. As it was shown e.g. by Byeon *et al.*, the more material is eroded in unit time the higher the concentration and the larger the diameter of NPs will be [89].

My OES results suggest that the concentration of metal vapor produced by a single spark in an SDG can be increased by increasing the spark energy, but only up to a certain threshold energy. Therefore, it is qualitatively understandable why the total NP concentration and hence the modal diameter starts to decrease, synchronously with the decreasing SRR (which therefore decreases the total vapor concentration) instead of the more steeply increasing spark energy curve after a certain gap size. The generality of this tendency is further strengthened by the fact that the very same behavior was found for Cu and Au electrodes.

Since the erosion rate and hence the number of metal atoms increases with increasing spark energy, the observed variation in the number concentration of metal atoms should be attributed to the variation of the volume of the vapor plume. Information on the vapor volume can be inferred from the plasma morphology measurements discussed in Section 3.2.2. Spectrally integrated images of the spark plasma cannot be directly correlated to the spatial extent of the metal vapor since *i*) only the emission of electrode material related species (atom, ions) would be relevant and *ii*) only the emitting species can be detected by this technique. Therefore I must rely on the plausible assumption that

---

<sup>10</sup> Please note that due to the constant ratio between the stored and spark energy in a given SDG, the trends shown in **Figure 3.1.4B** for stored energy are implicitly assumed to hold for the spark energy as well.

in the arc stage of the discharge, i.e. when electrode erosion takes place, metal ions and atoms exist in the conducting channel which is defined mainly by the gas ions. It was previously shown that the expansion speed of this plasma channel increases quasi linearly with spark energy (see **Figure 3.2.10**). This suggests that the higher the spark energy the further the metal atoms can get from the electrodes' axis by the end of the energy input, resulting in a larger vapor volume in the afterglow. In light of the above reasoning, the saturating concentration of metal atoms and metal NPs as evidenced by emission spectroscopic and nanoparticle results shown in **Figure 3.3.10** and **Figure 3.6.10**, respectively is caused by the balancing net effect of the increasing vapor mass by the increasing vapor volume. The threshold energy at which this effect takes place was found to be 300 mJ and 600 mJ for copper and gold, respectively. This is in qualitative agreement with the different erosion rates of these two materials, suggesting that the higher the erosion rate the larger spark energy is needed to balance off the eroded vapor mass.

A similar tendency to that is shown in **Figure 3.3.10** and **Figure 3.6.10** was observed by Horvath and Gangl during the investigation of the effect of spark energy on the mass concentration<sup>11</sup> of carbon particles produced in a modified SDG [84]. Beyond a threshold energy (which is reported to be 10 mJ for carbon) the mass concentration of particles saturates. This result is in line with the behavior I observed (cf. **Figure 3.3.10**) and further strengthens that the value of the threshold energy is material dependent.

---

<sup>11</sup> Measured gravimetrically after collecting the particles in a capillary membrane filter.

## 4. Summary

The mass production of metal nanoparticles with well controlled physical and chemical properties in an environmentally friendly and cheap way is of primary importance for the advancement of nanoparticle-based applications. Physical methods for producing nanoparticles in the gas phase have already proved their potential in satisfying the ever increasing needs of research and industry. Out of various aerosol-based techniques spark discharge nanoparticle generation stands out with its exceptional capability for producing high purity nanoparticles of virtually any composition from a stock of bulk conducting materials in a continuous, environmentally friendly and scalable manner with relatively low energy consumption. The method relies on the initiation of repetitive sparking between two electrodes, serving as bulk precursors, in a stream of gas, typically under atmospheric pressure. Under the impact of microsecond-long high-current spark discharges the electrode material becomes eroded and a cloud of atomic vapor forms in between the electrodes. Due to the atmospheric gaseous environment, the vapor will undergo a fast cooling, followed by nucleation resulting in the formation of gas suspended nuclei. Full coalescence of these seeds then leads to the formation of nanometer-sized spherical particles, which might grow further into nanoparticle aggregates due to collisions.

The experimental realization of spark-based nanoparticle synthesis is relatively simple, which, together with its inherent ability for upscaling, makes the technique very appealing for industrial applications. However, the technological simplicity hides complex, fundamental processes, occurring on multiple scales both in time and space. For example, the breakdown of the inter-electrode space occurs on the nanosecond timescale and involves the formation of plasma, whereas the evolution and oscillations of the discharge plasma take place on the microsecond time scale. The properties of the spark plasma and its interaction with the electrode surface determine the material erosion process which in turn affects the nanoparticle formation mechanism that may last up until hundreds of milliseconds after the breakdown.

In the present work, experimental investigation of the spark discharge plasma and the electrode erosion processes was carried out under the conditions of nanoparticle generation, with concomitant characterization of the produced nanoparticles. *In situ*, non-invasive methods were developed and applied which do not disturb the particle formation process. The temporal and spatial evolution of the spark plasma was examined by means of fast imaging. Images taken with temporal resolution on the nanosecond timescale were used to follow the changes of the plasma morphology, commencing as a confined quasi cylindrical channel and proceeding towards a more diffuse, irregular shape. The variation of the width and the expansion speed of the plasma channel, as well as the spatially resolved and spatially integrated light emission of the spark were also determined. In order to gain information on the species present in the spark gap, optical emission spectroscopy was employed. The acquired emission spectra were used to determine the excitation temperature and the electron concentration of the spark plasma at different

temporal and spatial domains. With the help of a semi-empirical plasma model developed, the concentration of the metal vapor in the spark gap was also estimated. The temporal evolution of the excitation temperature and the electron concentration was also elucidated via acquiring and processing temporally resolved atomic emission spectra. In parallel with the optical investigations of the spark plasma, current and voltage waveforms were also continuously monitored, and via *in situ* aerosol based sizing the size distribution of the generated nanoparticles was also determined. Correlation was found between the electrical and optical signals and the particle properties. Last, but not least, the effect of sparking on the electrode surface, i.e. the role of the material erosion process was also investigated by characterizing the changes of electrode surface morphology as a result of either a single spark or prolonged sparking. On one hand, complex morphological changes were observed even on electrodes exposed to a single spark discharge, while on the other, the development and characteristics of self-ordered patterns were revealed after intense sparking.

The main scientific results of my work are the following:

**Thesis I.** I have employed fast *imaging* for investigating the temporal evolution of the morphology of a spark plasma produced between copper electrodes under nitrogen atmosphere in a spark discharge nanoparticle generator. I have shown that the spark channel retains its relatively confined, cylindrical shape throughout the duration of electrical current between the electrodes. The channel width expands in time at supersonic speeds, which scale quasi-linearly with the spark energy. I have found that the light emitted by the spark has an uneven spatial distribution, and identified the existence of an axial “hot spot”, that is the position of highest emission intensity within the spark gap. I have proved that the position of this spot oscillates synchronously with the instantaneous current, and is always situated in the vicinity of the momentarily negative electrode [T1].

**Thesis II.** I have applied temporally and spatially resolved *emission spectroscopy* in order to characterize the spark plasma produced in a spark discharge nanoparticle generator during the generation of copper nanoparticles under argon atmosphere without disturbing the operation of the generator. I have determined the temporal variation of the excitation temperature and electron concentration in the arc stage of the spark. Temperatures in the range of 16600-20000 K and electron concentrations of  $\sim 2 \times 10^{17}$  to  $\sim 7 \times 10^{17} \text{ cm}^{-3}$  were found. For the characterization of the afterglow stage a semi-empirical equilibrium plasma model was developed. The model was used to derive the temperature and electron concentration and also to give an estimate on the number concentration of copper atoms and ions generated in the nanoparticle generator. Number concentration of copper atoms and ions was found to be in the order of  $10^{14} \text{ cm}^{-3}$  [T2]. I have derived the rate of change of the plasma temperature in the afterglow stage, i.e. the cooling rate of metal atoms from the emission spectra, which was found to be in the order of  $10^8 \text{ K s}^{-1}$  both in argon [T2] and nitrogen atmospheres [T3].

**Thesis III.** I have investigated the *electrical properties* (i.e. voltage, current, total resistance, instantaneous dissipated power and energy) of a spark discharge generator. I proved that only a fraction of the electrical energy stored in the capacitor is dissipated in the gap. The ratio between the (dissipated) spark energy, calculated from the instantaneous current, and the stored energy was found to be about 80% in the particular generator studied [T1]. My results also prove that the mass loss of the electrodes correlates with the spark energy, calculated from the instantaneous current, and not the energy stored in the capacitor, as is generally assumed in the literature. The stored energy is only proportional to the spark energy calculated from the current, when the electrical parameters of the discharge loop (i.e. resistance, inductance, capacitance) are fixed. Therefore both quantities can be used to describe the erosion processes in a given spark discharge generator, but only the current-based quantity should be used for comparing different generators [T4].

**Thesis IV.** I have investigated the changes of the *surface morphology* of metal electrodes (predominantly Ni and Cu), exposed to a controlled number of spark discharges, ranging from a single spark to several hundreds of thousands of sparks. I have proved that important information can be gained by the analysis of surface morphology of electrodes used in spark discharge generators. I have shown that even a single oscillatory discharge event (a so called single spark) creates complex surface morphology dominated by hundreds of craters and also featuring undulated areas and dendritic structures. I have also shown that the number and size of craters depend on the electrical current measured in the spark gap [T5]. By increasing the number of sparks delivered to the electrodes, the formation of closely packed, self-ordered patterns were found on nickel, gold and silver electrode materials [T6]. My results indicate that the spark energy, i.e. electric energy pumped into the electrode gap, is mostly used for melting and redistributing the electrode material over the electrode surface and only a small fraction of it is utilized for material release, and hence nanoparticle generation [T5].

**Thesis V.** I have investigated the effect of two of the main control parameters of a spark discharge generator, namely the gap size and the charging current on the size distribution of copper and gold *nanoparticles* generated in nitrogen atmosphere. I have found that by increasing the electrode gap and hence the spark energy the size of the generated nanoparticles varies via a maximum. I have shown that this behavior correlates with the variation of the integrated emission of metal atoms acquired during the afterglow stage of the spark plasma. The observed tendencies indicate that the concentration of metal atoms generated by a single spark cannot be increased monotonously beyond a certain level by simply increasing the spark energy. I have explained the results by the competing processes of spark channel expansion and electrode material erosion and their dependence on spark energy [T3].

## 5. Magyar nyelvű összefoglaló

### 5.1 Bevezetés

A nanotechnológia kétségtelenül napjaink egyik legfontosabb kutatási területe, melynek jelentőségét mi sem bizonyítja jobban, hogy már nem is szorul bemutatásra. A legtöbb ember hallhatott már a „nano”-ról, azon titokzatos dolgok egyikéről, mely egyszerre menti meg és pusztítja el az emberiséget. De ahogy az lenni szokott, a valóság valahol a két véglet között helyezkedik el. Azon képesség, hogy különböző anyagokat a nanométeres mérettartományban manipulálhassunk vitathatatlanul olyan eszközöket adott a kezünkbe, melyek néhány évtizeddel ezelőtt még elképzelhetetlenek lettek volna. Gyógyszerek irányított szállítása és alkalmazása az emberi szervezeten belül [1], az energia, étel és vízellátás javítása [2], erős mégis könnyű anyagok előállítása [3], vagy napelemek és akkumulátorok hatékonyságának növelése [4] csak néhány kiragadott példa azon lehetőségek közül, amiket a nanotechnológia kínálhat. Noha a nanotechnológia valamint a nanotudományok számos eredménye sikerrel jutott el az ipari alkalmazásig és ezzel mindennapi életünk részévé vált, továbbra is jelentős azon alkalmazási lehetőségek száma, melyek csak a laboratóriumok falain belül léteznek. Számos feltételnek kell teljesülni ahhoz, hogy egy új technológia kitörjön a laborból és utat találjon a felhasználóig. Egyike e feltételeknek a megfizethető alapanyagok biztosítása. A nanotechnológia fő építőelemei a nanostruktúrák, melyek dimenzióik szerint lehetnek 2D-s nanorétegek, 1D-s nanorudak vagy nanoszálak, valamint 0D-s nanorészecskék [5]. E struktúrák környezetbarát tömegtermelése egy olyan technológiai kihívás, melynek megoldása elengedhetetlen a nanotechnológián alapuló termékek további fejlődéséhez. Jelen dolgozat témája a *szikrakisüléssel nanorészecske generálás* néhány alaptudományi aspektusának vizsgálata. E technika egyike a legígéretesebb módszereknek, melyek kontrollált tulajdonságú nanorészecskék akár ipari mennyiségű előállítására is alkalmasak.

Nanorészecskék előállítására számos kémiai reakciókon, valamint fizika vagy mechanikai átalakulásokon alapuló módszer létezik [6]. A kémiai módszerek több mint másfél évszázados történelemre tekintenek vissza és ma is meglehetősen népszerűek, mivel segítségükkel változatos összetételű, kontrollált méretű és alakú részecskék állíthatók elő [7]. A kémiai eljárások ugyanakkor számos kémiai prekursor és vegyszert, valamint gyakran nagy mennyiségű oldószert is igényelnek, melyek inherensen növelik a potenciális szennyező anyagok jelenlétét a folyamatban. A szennyezők pedig jelentősen megváltoztathatják a nanostruktúrák tulajdonságait [8]. A fizikai eljárások a kémiai szintézis valós alternatíváját kínálják, ugyanis lehetővé teszik nagy tisztaságú részecskék folyamatos előállítását kis mennyiségű melléktermék keletkezése mellett, továbbá magukban hordozzák a termelés felskálázásának lehetőségét [9].

Az egyik legnépszerűbb, ipari körülmények között is sikerrel alkalmazott technika a láng pirolízis, mely jól alkalmazható fém-oxid részecskék előállítására [10], ugyanakkor nem teszi lehetővé tiszta fém nanorészecskék előállítását. Az egyik leggyakoribb módszer, mellyel fém nanorészecskék hozhatók létre párologtatáson, valamint a fémgőz

nukleációján és kondenzációján alapul [11]. A kiinduló anyag elpárologtatására számos út létezik, pl. kemencés hevítés [12], elektromos izzítás (ún. izzó vezeték technika) [13] vagy lézeres abláció [14]. Ezen eljárások közös hátránya, hogy alacsony hatásfokúak, valamint nehézkesen skálázhatók. E hátrányokat egyszerre küszöböli ki a szikrakisüléses nanorészecske generálás, amely hatékony energia-felhasználást tesz lehetővé bizonyítottan felskálázható termelékenység mellett [15,16].

A szikrakisüléses nanorészecske generátorok (angol rövidítéssel SDG-k) felépítése meglehetősen egyszerű, alapja egy gáz-tömör kamra, melyben két, egymástól néhány milliméter távolságra elhelyezett elektród található. A nagyfeszültségű elektromos szikrakisülések létrehozásáról a szikraközze sorba kötött kondenzátor gondoskodik (kisülési kör), melyet egy DC tápegység tölt folyamatosan (töltő kör). A kondenzátor folyamatos töltése, majd a szikraközön keresztüli kisülése következtében repetitív szikrázás jön létre. A szikrakisülések létrejöttének lehetőségét a szikraköz átütése teremti meg, melynek során a két elektródot egy kezdetben elsősorban elektronokat és gáz ionokat tartalmazó vezető csatorna (szikra csatorna) köti össze. Az elektródok anyaga a szikraplazma hatására erodálódik, melynek következtében az elektródanyag atomjaiból álló gőz jön létre a szikraközben. A gáz-környezet hűtő hatása, valamint táulás következtében az atomok lehűlnek majd nukleációs, kondenzációs és koagulációs lépéseken keresztül nanorészecskéket hoznak létre [17].

A szikrakisüléses nanorészecske generálásban rejlő tömegtermelési potenciál csak részben köszönhető az eljárás viszonylagos egyszerűségének. Ennél fontosabb, hogy a részecske előállítási folyamat könnyedén és kontrolláltan skálázható fel környezetbarát módon, viszonylag alacsony költségek árán identikus generátor kamrák párhuzamos üzemeltetésével. A BUONAPART-E projektben Európa 21 kutatóhelye (köztük a Szegedi Tudományegyetem Optikai és Kvantumelektronikai Tanszékén működő csoportunk) dolgozott együtt a technika felskálázásán [16]. A négy évig tartó együttműködés során a szikrakisüléses nanorészecske generálás számos alaptudományi aspektusát megvizsgáltuk partnereinkkel, leküzdve számos felmerülő technikai kihívást is. Kutatócsoportunk feladatai közé tartozott az SDG-ben lezajló fundamentális folyamatok vizsgálata, különös tekintettel azokra, melyek a szikra plazmában valamint az elektródok felszínén játszódnak le.

Annak ellenére, hogy az SDG-k alapelve egyidős a benzinmotorokkal, a kimondottan nanorészecskék előállítására szolgáló generátorok 1988 óta léteznek Andreas Schmidt-Ott és kollégái munkájának eredményeként [15]. Noha napjainkban SDG-k már kereskedelmi forgalomban is kaphatók [18], és a technikát számos csoport használta és használja [19–21,23–25,22], a részecskék kialakulásához vezető fundamentális folyamatokkal kapcsolatban még mindig vannak nyitott kérdések. Ennek egyik oka az egyes részecske-keletkezési szakaszok vizsgálatának nehézsége, ami különösen hangsúlyos a folyamat kezdeti szakaszában. A gáz fázisban keletkezett részecskék vizsgálati módszerei tradicionálisan két nagy csoportra oszthatók. A módszerek első csoportjának alapja a részecskék mintavételezése (pl. elektrosztatikus leválasztással vagy tehetetlenségi

impaktorokkal), majd elektron mikroszkópián alapuló karakterizálása. A második csoportba olyan eljárások tartoznak, melyek praktikusán valós idejű vizsgálatot tesznek lehetővé. Ilyen eszközök például a mozgékonyaság szerinti részecske szeparátor és számláló (Scanning Mobility Particle Sizer, SMPS), az aeroszol részecske tömeg analizátor (Aerosol Particle Mass Analyzer, APM) vagy az aeroszol tömeg spektrométer (Aerosol Mass Spectrometer, AMS). Ezen eszközök közös tulajdonsága, hogy csak a részecskék keletkezési helyétől távolabb alkalmazhatók, így nem szolgáltatnak fundamentális információt az elsődleges keletkezési zónáról. E hiányosságot áthidalandó kísérletet tettek a nanorészecskék mintavételezésére a szikraköz közelében [26], ám az alkalmazott módszer invazív jellegénél fogva hatással van a generátor áramlási viszonyaira és ezáltal magára a részecske-keletkezésre is. További kihívást jelent, hogy a szikrakisüléseken alapuló nanorészecske keletkezés egy széles időskálán lezajló folyamat, ami megnehezíti a teljes jelenség vizsgálatát. Összehasonlításként: a részecskék keletkezése szekundumos, vagy szekundum alatti időskálán játszódik le, melyhez képest a szikrák tipikusan mikroszekundumos élettartama gyakorlatilag elhanyagolható. Mindazonáltal e rövid idő alatt is jellegzetes, időben változó folyamatok zajlanak le minden egyes szikrában, amelyek befolyásolják az elektródok erózióját és ezáltal a keletkező részecskékre is hatással vannak.

Ahogy a fenti példák is mutatják, az SDG-kre jellemző technikai és elvi korlátok a generátorban lezajló folyamatok vizsgálatára alkalmazható módszerekre is korlátokat szabnak. A megszokott generátor felépítés nem változtatható meg annak érdekében, hogy kísérleteket végezhessünk a szikra plazmán, mert ezáltal a részecske-keletkezés kondíciói is megváltoznának. Olyan kísérleti eljárásokat kell alkalmazni, melyek lehetőleg nagy időbeli feloldással képesek információt szolgáltatni a szikrában lezajló folyamatokról úgy, hogy a lehető legkevésbé befolyásolják azokat. E peremfeltételeket figyelembe véve a munkám során alkalmazott kísérleti módszerek magját olyan non-invazív, *in situ* eljárások adták, mint az időben és térben bontott optikai emissziós spektroszkópia (OES) és képalotás, kiegészítve a szikra elektromos jeleinek (pillanatnyi áram és feszültség) folyamatos monitorozásával. E technikákkal lehetőség nyílt a részecskék keletkezését megelőző folyamatok vizsgálatára azok megzavarása nélkül, beleértve a szikra plazma *operando* vizsgálatát a nanoszekundumos időskálán. Az optikai elvű vizsgálatokat a keletkezett nanorészecskék *in situ* és *ex situ* vizsgálata, valamint a szikráztatásnak kitett elektród felszín *ex situ* vizsgálata egészítette ki. A változatos kísérleti módszerek lehetővé tették, hogy a szikra plazma tulajdonságait és a plazma elektródokra gyakorolt hatását különböző szemszögekből közelítsem meg. Munkám célja a nanorészecskék előállítására használt szikrakisülés karakterizálása volt, ezen belül a szikra plazma optikai emissziójának és morfológiájának vizsgálata, valamint a plazma összetételének, a plazmát alkotó specieszek koncentrációjának és hőmérsékletének meghatározása az idő és különböző kísérleti paraméterek függvényében. További célt volt az elektród erózió vizsgálata, beleértve az elektródok felszínén lezajló folyamatokat és a kisülési kör elektromos paramétereinek erózióra gyakorolt hatását. A fenti gondosan megválasztott

kísérleti eszköztárral megszerzett információ hozzájárult ahhoz, hogy pontosabb képet kapjunk a szikrában lezajló folyamatokról, illetve elvezetett a szikrakisülések segítségével előállított részecskék tulajdonságainak még hatékonyabb kontrollálásához.

## 5.2 Szikrakisüléssel generált nanorészecske generálás

A szikrakisüléssel generált nanorészecske generálás egy ún. „bottom-up” technika, mellyel gáz fázisban állíthatók elő nanorészecskék. A módszer alapelve hasonló a többi aeroszol-alapú eljáráséhoz, azzal a különbséggel, hogy a kezdeti atomfelhőt elektromos szikrakisülések segítségével állítják elő. Burtscher és Schmidt-Ott alkalmaztak először szikrakisüléseket nanorészecske-előállítási céllal 1982-ben [70], amit egy 1988-as tanulmány követett, amiben bemutatták az ún. szikrakisüléssel generált nanorészecske generátort (SDG), ami a részecskék előállításához szükséges elektromos áramkört, kisülési kamrát és a gáz és aeroszol kezelő alegységeket is tartalmazta [15]. Ahogy az előző fejezetben már röviden említésre került, az SDG alapja egy gáz-tömör kamra és az abban található két, egymástól néhány milliméter távolságra elhelyezett elektród. Az elektródok a részecskék kiinduló anyagaként szolgálnak, vagyis a keletkező nanorészecskék tisztaságát az elektród-anyag és a gázkörnyezet tisztasága szabja meg [17]. Az eljárás egyik legnagyobb előnye a sokoldalúsága, ugyanis gyakorlatilag bármely vezető anyagból (beleértve a fémeket, ötvözeteket, grafitot vagy félvezetőket) készíthetők elektródok, és ezáltal állíthatók elő nanorészecskék egy adott rendszeren belül [46]. Eltérő anyagú, vagy kompozit elektródokkal többkomponensű nanorészecskék is egyszerűen előállíthatók, akár olyan anyagokból is, melyek makroszkopikusan nem keverednek egymással [71].

A szikrakisülések egy a szikraközrel sorosan kötött kondenzátor (bank) kisülése révén jönnek létre. A folyamat olyan értelemben szabályozatlan, hogy a kisülés akkor valósul meg, amikor a kondenzátoron lévő (és ezáltal a két elektród közötti) feszültség eléri a szikraköz átütési feszültségét [11]. Az SDG-k kisülési körét tipikusan kis ellenállás és kis induktivitás jellemzi (mindkét komponens a vezetékek, csatlakozók, egyéb alkatrészek saját ellenállásából és induktivitásából adódik össze), melynek eredményeként alulcsillapított, azaz oszcilláló, nagy áramú és feszültségű, néhány mikroszekundum hosszú szikrakisülések jönnek létre. A kialakuló kisülést gyakran egyszerűen egy-szikrának szokás nevezni, ami ugyanakkor valójában egy szinuszosan oszcilláló és exponenciálisan csillapodó amplitúdójú áram és feszültség jelet takar, mely egyúttal a polaritás periodikus változását is jelenti [72].

Az SDG-ben lezajló komplex folyamatok miatt a nanorészecskék kialakulásához vezető mechanizmusok és az ezeket befolyásoló kísérleti paraméterek leírása elsősorban kísérleti eredmények kvalitatív magyarázatán alapul. A közelmúltban került publikálásra egy egyszerű szemi-empirikus analitikus és egy numerikus modell, melyek segítségével megadható az elsődleges részecskék méreteloszlásának a kísérleti paraméterektől való függése [47,77]. A részecskék keletkezésének fő lépései a következők. Az elektródok felszínét az ún. forró pontokban melegíti a szikra, ahol kölcsön hat az elektródok

anyagával párologást és egy fémgőz felhő kialakulását idézve elő [17,78]. Ezen túl a gáz, valamint az anód és katód ionjai is bombázhatják az elektródokat, további anyagkiválást téve lehetővé [79]. Miután az atomos gőz adiabatikus tágulás, valamint a hordozó gázzal való keveredés útján megfelelő hőmérsékletűre hűl, nukleáció útján atom-klaszterek jönnek létre. E klaszterek kondenzáció és koaleszcencia útján különálló, gömbi részecskéként növekednek egy maximális méret eléréséig, mely az ún. elsődleges részecskéket jellemzi. E pont elérése után az elsődleges részecskék már nem képesek a gömbi alakjukat megtartva növekedni, és részecske aggregátumok alakulhatnak ki [17].

A keletkezett részecskék tekintetében a szikrakisüléssel nanorészecske generálás számos hasonlóságot mutat olyan eljárásokkal, melyek tömbi fém céltárgyak ablációján alapulnak. Tipikus példa erre a lézeres abláció, mely a szikrakisüléssel módszerhez nagyon hasonló részecskéket eredményez [73]. A legnagyobb előnye a szikrakisüléssel részecske generálásnak pl. a lézeres ablációval szemben viszonylagos technikai egyszerűsége. Az SDG-k nem tartalmazzák a lézerekhez hasonlóan drága eszközöket, gyakorlatilag folyamatos működésre képesek (a kondenzátor folyamatos töltése és kisülése által), minimális hulladék keletkezése mellett [17]. Továbbá az SDG-ken alapuló eljárás nagy előnye, hogy skálázható. A termelékenység növelésének egyik módja a szikra ismétlési frekvencia növelése. A keletkező részecskék tömege az ismétlési frekvencia növelésével lineárisan növekszik [46]. Ugyanakkor a klasszikus SDG-kben a maximálisan elérhető ismétlési frekvenciát a töltő tápegység maximum néhány száz Hz-ben limitálja, ami a maximálisan elérhető részecske kihozatalra is korlátot szab. E korlát leküzdésére szolgál az a közelmúltban kifejlesztett speciális tápegység, amit SDG-k nagy frekvenciájú üzemeltetéséhez terveztek és ami a maximális ismétlési frekvenciát 20 kHz-re emeli [17]. A termelékenység felskálázásának másik lehetséges módja egyedi SDG-k összekapcsolása és párhuzamos üzemeltetése. Ezáltal akár az ipari igényeket kielégítő részecske-hozam is elérhető [77]. Problémát jelenthet, hogy a részecskék megnövekedett koncentrációja a gáz fázisban általában részecske aggregátumok illetve agglomerátumok kialakulásához vezet [76], ami bizonyos alkalmazások szempontjából előnytelen lehet. Ez a folyamat a vivő gáz áramlási sebességének változtatásával kontrollálható: SDG-kben 10 nm alatti gömbi részecskék is előállíthatók [47]. Ez ugyanakkor azt is jelenti, hogy minél nagyobb a részecske-koncentráció, annál nagyobb áramlási sebességre van szükség az aggregáció meggátolásához. A gyakorlatban a praktikusan elérhető maximális áramlási sebesség limitálva van, ami kompromisszumot jelent az alacsonyabb hozamú, kisméretű szinglet részecskék és a nagy hozamú, nagyobb méretű nanorészecske aggregátumok között.

### 5.3 Kísérleti módszerek

Többféle SDG kialakítás létezik, amelyek bizonyos technikai részletekben eltérhetnek, de működési elvük és a fő építőelemek azonosak. Minden SDG központi eleme a kisülési kamra, valamint az elektromos áramkör, ami a szikrázást táplálja [11]. A tipikusan

rozsdamentes acélból készült, gáz-tömör kamrát<sup>M1</sup> általában úgy alakítják ki, hogy lehetővé tegye az elektromos átvezetések, elektród-mozgatók, egyéb mérőműszerek csatlakoztatását, valamint tartalmazzon legalább egy betekintő ablakot optikai megfigyeléshez. Az elektródok elhelyezése a kamrán belül egyaránt lehet vízszintes vagy függőleges, és a szikraközt folyamatosan öblítő vivő gáz áramlási iránya szintén lehet keresztirányú, vagy koaxiális, lefelé, vagy felfelé irányuló. Az elektródok egymással szemben álló két vége közötti távolságot (vagyis a szikraköz méretét) egy vagy két eltolóval lehet beállítani. A kamrában atmoszferikus nyomást hoznak létre, a vivő gáz áramlási sebességét pedig általában egy tömegáram szabályozóval (mass flow controller, MFC) kontrollálják.

Kísérleteimben a szikraköz méretét a 0,5-4,0 mm tartományban szabályoztam mikrométercsavarok segítségével. Az argon vagy nitrogén vivő gáz áramlási sebességét az 1-10 l/min tartományban változtattam. Minden kísérletemet atmoszferikus nyomáson végeztem, melyet egy vákuum pumpa és egy túszelep segítségével állítottam be és egy nyomásmérő segítségével monitoroztam. Kísérleteimben 6,35 mm illetve 3,00 mm átmérőjű, henger alakú elektródokat használtam lapos, vagy hegyezett (30°-os csúcshöszöggel) végekkel. A lapos végű elrendezésnél az eróziós hatás eloszlik az elektród teljes keresztmetszetén, míg a kihegyezett elektródok esetén a csúc közelében koncentrálódik. Az elérni kívánt lehető legnagyobb részecske termelés miatt hatékony erózió kívánatos, emiatt általában a lapos geometriát alkalmazzák SDG-kben. Ugyanakkor e geometriában az egymást követő szikrák „vándorolnak” az elektród felszínén, ami a szikra plazma pozicionális instabilitását okozza, ami megnehezíti az optikai elvű vizsgálatokat. Továbbá a szikrázás elektromos stabilitását is ronthatja, a folyamatosan változó felszíni tulajdonságok és az ennek következtében változó átütési feszültség miatt. A fentiek alapján elmondható, hogy hegyezett elektródok segítségével megbízhatóbb fundamentális információkat nyerhetünk a plazmáról, míg a lapos elektródok használata közvetlenebb kapcsolatot jelent a részecske-generálás standard körülményeivel. Emiatt a nagy helyzeti stabilitást igénylő kísérletekben hegyezett elektródokat használtam, míg azokban, amelyekben a fő hangsúly az elektród erózió, vagy a keletkező részecskéken volt, lapos elektródokat alkalmaztam.

A szikraköz elektromos táplálásáról egy egyszerű kondenzátortöltő áramkör gondoskodott. Egy, a kísérleteimben tipikusan 8-29 nF kapacitású kondenzátort (vagy kondenzátor bankot) egy nagyfeszültségű kondenzátortöltő tápegység töltött maximum 10 kV körüli feszültségre, jellemzően néhány, vagy néhány tíz milliamper töltőáram mellett. Mivel a szikraköz sorba van kötve a kondenzátorral, a kisülés akkor jön létre, amikor a kondenzátor feszültsége eléri a szikraköz átütési feszültségét. Ennek hatására egy bipoláris, oszcilláló kisülés jön létre, melynek frekvenciáját és csillapodási tényezőjét az áramkör ellenállása, induktivitása és kapacitása szabja meg. A tápegység a kisülés alatt is folyamatosan tölti a kondenzátort („szabadonfutó” üzemmód), de mivel a kisülés során a

---

<sup>M1</sup> A kísérleteim túlnyomó többségében használt, a Pfeiffer Vacuum GmbH által gyártott kisülési kamra az EU FP7 keretprogramja által támogatott BUONAPART-E projekt keretein belül került kifejlesztésre.

körben folyó áram erőssége (ami tipikusan néhány száz amper) sok nagyságrenddel nagyobb, mint a töltőáram erőssége, a töltési és kisülési ciklusok függetlennek tekinthetők egymástól. A szikrák ismétlési gyakoriságát a szikra-ismétlési frekvenciával szokás megadni, ami a töltőárammal és az átütési feszültség változtatásával szabályozható, ha feltételezzük, hogy az egyéb kísérleti paraméterek állandóak.

A szikra plazma jellemzésére irányuló kísérletekben rutinszerűen mértem az elektródok közti feszültség és a szikraközben folyó áram időbeli változását egy nagyfeszültségű szondával (pl. Agilent N2771B) és egy árammérővel (Pearson 110). Ezen elektromos méréseknek a szikrára jellemző elektromos jelalakok meghatározásán túl az egyéb kísérleti eszközök szinkronizálásában is nagy szerepe volt. A szikrák vizsgálata azok szabályozatlan kialakulása és tranziens jellege miatt pontos időbeli szinkronizációt igényel, amit a szikraköz átütését kísérő éles feszültségeséshez, vagy áramugráshoz rögzítve valósítottam meg egy jelgenerátor (Stanford DG535) segítségével. A szikra morfológiájának, illetve optikai emissziójának időbontott vizsgálatát egy erősített CCD (ICCD) kamerával végeztem (Andor iStar 734-18F-03), tipikusan 50-500 ns időbeli felbontással. A morfológiai (gyors fényképezés) vizsgálatokhoz a kamerát a megfelelő objektívekkel láttam el, míg az emissziós spektroszkópiai mérésekhez a kamerát egy Andor Mechelle 5000 száloptikás spektrográffal kiegészítve használtam. Térben integrált mérések esetén a szikra fényét egy lencsével gyűjtöttem, míg a térben bontott mérésekhez a szikrát egy lencsével leképeztem, majd a kép különböző pontjaiba helyeztem a spektrográf optikai szálát. A spektroszkópiai elrendezés a 300-800 nm hullámhossztartomány vizsgálatát tette lehetővé,  $\sim 0,125$  nm (435 nm-en) felbontással. A térbeli felbontás a spektroszkópiai mérésekben  $\sim 50$   $\mu\text{m}$  volt. Az emissziós spektrumok plazma diagnosztikai felhasználása érdekében a spektroszkópiai rendszer spektrális érzékenységét egy NIST-kalibrált deutérium-halogén fényforrás (Ocean Optics Inc, DH-2000-CAL) segítségével kalibráltam. A kalibrációt minden mérési sorozat előtt ellenőriztem és szükség szerint megismételtem.

Az SDG-ben keletkező nanorészecskéket az *ex situ* elektronmikroszkópiás analízishez egy házi készítésű alacsony nyomású tehetetlenségi impaktorról, illetve elektrosztatikus úton választottam le hordozókra (tipikusan TEM gridekre). A nanorészecskék méreteloszlását a generálás után közvetlenül, *in situ* is meghatároztam, melyhez egy Grimm Aerosol Technik GmbH SMPS-C, illetve egy házi készítésű SMPS rendszert használtam.

Az elektród-felszín eróziójának vizsgálatához egy laboratóriumunkban tervezett elektromos áramkört használtunk, mely lehetővé tette kontrollált számú szikra keltését az SDG-ben. Ennek segítségével követtem a felszín morfológiájában egyetlen szikra hatására bekövetkező változásokat. A mérésekhez előre polírozott elektródokat használtunk, melyeket szikráztatás előtt és után is optikai mikroszkópiával (Nikon Optiphot 100S), lézeres pásztázó mikroszkópiával (Keyence VK-X100K) és atomerő mikroszkópiával (PSIA XE-100) jellemeztünk. Vizsgáltuk az elektródok felszínén kialakult struktúrákat hosszan

tartó szikrázás (több százezer szikra) után is, melyeket lézeres pásztázó mikroszkópiával (Keyence VK-X100K) karakterizáltunk.

A kísérletek során keletkező nagy mennyiségű mérési adat feldolgozásához, kiértékeléséhez és a plazma diagnosztikai számolásokhoz Origin szoftvert, illetve saját készítésű cél-szkripteket használtam, melyeket MATLAB illetve Python programozási nyelveken írtam.

## 5.4 Eredmények

A nanorészecskék előállítására használt elektromos szikra plazmát, valamint a szikra elektródokra gyakorolt eróziós hatását vizsgáló kísérleteim során *in situ, non-invazív* eljárásokat használtam, a nanorészecskék keletkezését előidéző folyamatok megzavarása nélkül, kiegészítve a keletkező nanorészecskék karakterizálásával. A szikra plazma tér- és időbeli változását gyors-fényképezés segítségével vizsgáltam. A néhány tíz nanoszekundumos illetve szub-mikroszekundumos időbeli felbontással készített képsorozatokból rekonstruáltam a plazma alakjának változását. Kimutattam, hogy az egy viszonylag jól körülhatárolt, hengerszerű csatornából diffúzzá, és szabálytalanná válik. A plazma csatorna átmérőjének időbeli változását és a plazma tágulási sebességét is meghatároztam, a spektrálisan integrált optikai emisszió térbeli eloszlásával együtt. Időben és térben bontott emissziós spektrumok analízisével meghatároztam a gerjesztési plazma hőmérsékletet és az elektron koncentrációt különböző térbeli és időbeli pontokban. Egy egyszerű szemi-empirikus plazma modell segítségével az egy szikra által erodált elektród anyag szikraközben jelenlévő koncentrációját is megbecsültem. Az optikai emissziós mérésekkel párhuzamosan a szikra áramát és feszültségét is folyamatosan regisztráltam, valamint meghatároztam a keletkező részecskék méreteloszlását. Korrelációt találtam az elektromos, optikai és részecske adatok között. Az egy, illetve több százezer szikra hatásának kitett elektródok eróziójának vizsgálatával megmutattam, hogy már egyetlen szikra hatására is komplex struktúrák alakulnak ki az elektródok felszínén, amelyek hosszantartó szikrázás (nagyszámú szikra) hatására ön-rendező, szabályos mintázatokká alakulnak.

Munkám legfontosabb tudományos eredményeit a következő tézispontok összegzik:

I. *Gyors-fényképezés* alkalmazásával megvizsgáltam egy szikrakisüléssel generátorban réz elektródok között, nitrogén atmoszférában keltett szikra plazma morfológiájának időbeli változását. Megmutattam, hogy a szikra csatorna megtartja viszonylag szabályos, hengeres alakját mindaddig, míg elektromos áram folyik az elektródok között. A csatorna az idővel tágul, szélessége szuperszonikus sebességgel növekszik, ami közel lineárisan skálázódik a szikra energiájával. Azt találtam, hogy a szikra által emittált fény térbeli eloszlása nem egyenletes, a szikraközben egy maximális intenzitású axiális régiót, ún. „hot spot”-ot azonosítottam. Megmutattam, hogy e régió helye szinkronban van a pillanatnyi árammal és mindig az aktuálisan negatív polaritású elektród közelében található **[T1]**.

**II.** Térben és időben bontott *emissziós spektroszkópia* alkalmazásával, a generátor működésének megzavarása nélkül jellemeztem a szikrakisüléssel nanorészecske generátorban, argon atmoszférában létrehozott, réz nanorészecskék előállítására használt szikra plazmát. Meghatároztam a szikra „ív” fázisában (arc stage) a plazma gerjesztési hőmérsékletét és az elektron koncentrációt az idő függvényében. A hőmérséklet a 16600-20000 K, az elektron koncentráció pedig a  $\sim 2 \times 10^{17}$ - $\sim 7 \times 10^{17}$  cm<sup>-3</sup> tartományban változott. A szikra „utóizzás” fázisának (afterglow stage) leírásához megalkottam egy szemiempirikus egyensúlyi plazma modellt. A modell segítségével meghatároztam a plazma hőmérsékletét és az elektron koncentrációt, valamint megbecsültem a nanorészecske generátorban előállított réz atomok és ionok számkoncentrációját, melynek értékére azt kaptam, hogy az a  $10^{14}$  cm<sup>-3</sup> nagyságrendbe esik [T2]. Az „utóizzás” (afterglow) fázisban felvett emissziós spektrumokból a plazma-hőmérséklet változásának sebességét is meghatároztam, ami a fém atomok hűlési sebességeként értelmezhető. A hűlési sebességre mind argon [T2], mind nitrogén gázban  $10^8$  Ks<sup>-1</sup> nagyságrendbe eső értéket kaptam [T3].

**III.** Megvizsgáltam egy szikrakisüléssel nanorészecske generátor *elektromos tulajdonságait*, vagyis a feszültség és áram időfüggését, a teljes ellenállást, valamint a pillanatnyi disszipált teljesítményt és energiát. Megmutattam, hogy a kondenzátorban tárolt elektromos energiának csak egy része disszipálódik a szikraközben. A pillanatnyi áramból számolt (disszipált) szikra energia és a tárolt energia aránya 80% körül volt az általam vizsgált generátorban [T1]. Eredményeim azt bizonyítják, hogy az elektródok tömegfogyása a pillanatnyi áramból számolt szikra energiával korrelál, nem pedig a kondenzátorban tárolt energiával, ahogy azt a szakirodalomban általában feltételezik. Ha a kisülési kör elektromos paraméterei (ellenállás, induktivitás, kapacitás) állandóak, az áramból számolt szikra energia arányos a tárolt energiával. Emiatt egy adott szikra-generátorban mindkét mennyiség használható az eróziós folyamat leírására, viszont csak az áramon alapuló mennyiség használható különböző generátorok összehasonlítására [T4].

**IV.** Kontrollált számú szikrakisülésnek – egytől több százezer szikráig – kitett fém elektródok (kiemelten Ni és Cu) *felületi morfológiájának* változását nyomon követve megmutattam, hogy a szikra-generátorokban alkalmazott elektródok felületi morfológiájának analízisével hasznos információk nyerhetők. Megmutattam, hogy már egyetlen oszcilláló szikra (az ún. egy-szikra) is komplex felületi morfológiát hoz létre, melyet több száz kráter dominál, és megjelennek ún. hullámos (undulált) és dendritikus struktúrák is. A kráterek mérete és száma függ a szikraközben mérhető áram erősségétől [T5]. Növelve a szikrák számát az elektródok között, szorosán elhelyezkedő, ön-rendező mintázatok kialakulását figyeltem meg nikkellel, arannyal és ezüst elektródokon [T6]. Eredményeim arra utalnak, hogy a szikra energia (vagyis a szikraközbe pumpált elektromos energia) döntően az elektródok anyagának megolvasztására és annak az elektród-felületén történő átrendeződésére fordítódik, mindössze egy kis része hasznosul anyageltávozásra és ezáltal nanorészecskék keltésére [T5].

V. Megvizsgáltam, hogy milyen hatással van a szikrakisüléssel generált nanorészecske generátor fő kontroll-paraméterei közül kettőnek (a szikraköz méretének és a töltő áram erősségének) változtatása nitrogén atmoszférában előállított réz és arany *nanorészecskék* méreteloszlására. Azt találtam, hogy a szikraköz méretének és ezáltal a szikra energiájának növelésével az előállított részecskék mérete maximumot mutat. Megmutattam, hogy ez a viselkedés korrelál a szikra plazma fém atomjai, az „utóizzás” (afterglow) fázisában mérhető, integrált emissziójának változásával. A megfigyelt tendenciák arra utalnak, hogy a szikra energia egyszerű növelésével az egyetlen szikrával létrehozható fém atomok koncentrációja nem növelhető folyamatosan egy adott szint fölé. Az eredményeket a szikra csatorna tágulásának és az elektród anyag eróziójának a szikra energia növelésével jelentkező, egymással ellentétes hatásával magyaráztam [T3].

## Publications

[T1] J. M. Palomares, **A. Kohut**, G. Galbács, R. Engeln, and Zs. Geretovszky: “A time-resolved imaging and electrical study on a high current atmospheric pressure spark discharge” *Journal of Applied Physics*, **118**, 233305 (2015).

[T2] **A. Kohut**, G. Galbács, Zs. Márton, and Zs. Geretovszky: “Characterization of a copper spark discharge plasma in argon atmosphere used for nanoparticle generation” *Plasma Sources Science and Technology*, **26** 045001 (2017).

[T3] **A. Kohut**, L. Ludvigsson, B. O. Meuller, K. Deppert, M. E. Messing, G. Galbács, and Zs. Geretovszky: “From plasma to nanoparticles: optical and particle emission of a spark discharge generator” *Nanotechnology*, DOI: 10.1088/1361-6528/aa8f84 (2017).

[T4] **A. Kohut**, L. P. Villy, T. Ajtai, G. Galbács, and Zs. Geretovszky: “The effect of circuit resistance on the particle output of a spark discharge nanoparticle generator” under review in the *Journal of Aerosol Science* (2017).

[T5] **A. Kohut**, M. Wagner, M. Seipenbusch, Zs. Geretovszky, and G. Galbács: “Surface features and energy considerations related to the electrode erosion processes in a spark discharge nanoparticle generator” under review in the *Journal of Aerosol Science* (2017).

[T6] M. Wagner, **A. Kohut**, Zs. Geretovszky, M. Seipenbusch, and G. Galbács: “Observation of fine-ordered patterns on electrode surfaces subjected to extensive erosion in a spark discharge” *Journal of Aerosol Science*, **93** 16-20 (2016).

## Acknowledgements

There are many people who directly or indirectly contributed to this dissertation. I am grateful to everyone who helped me along the way.

I am particularly thankful, both professionally and personally, to my supervisor Zsolt Geretovszky. Instead of telling me how to solve a problem, he always wanted to find solutions together, and guided me through each steps of scientific work. I believe this was the hard way (for both of us), but I wouldn't be the same researcher without his efforts, for which I will always be grateful.

I would like to express my gratitude to Gábor Galbács, whom I could also count on during my research. Besides sharing his expertise in the field of plasma spectroscopy, he was always there to bring in a different perspective when it was needed.

I am grateful to Zsuzsanna Márton for lending us her spectrograph, and also for her guidance and thoughts on emission spectroscopic measurements.

I am thankful to Tamás Szörényi for his assistance during my years in the lab, and for his kind help in finalizing this dissertation.

I had the pleasure to work with a lot of great people within the BUONAPART-E project, in which I learned a lot. I am especially thankful to Jose Maria Palomares Linares and Moritz Wagner, I really enjoyed our joint work.

I thank Anikó Metzinger and András Búzás their assistance in some of my experiments.

I would like to thank the support and assistance of the leadership and people of the Department of Optics and Quantum Electronics, I am especially thankful to Béla Hopp and Judit Kopniczky.

I cannot be grateful enough to my family for always being there for me, and for supporting and encouraging me in my whole life. I especially thank the continuous support, help, and patience of my wife. She was the one who always listened to me and encouraged me to carry on when I was disappointed, this dissertation couldn't have been done without her.

I am grateful for the financial support of the European Union's Seventh Framework Program (No. 280765; BUONAPART-E), the TÁMOP program of Hungary (No. 4.2.2.A-11/1/KONV-2012-0047, No. 4.2.2.A-11/1/KONV-2012-0060, No. TÁMOP-4.2.2/B-10/1-2010-0012), the Campus Hungary Program, the NTP-NFTÖ-17-B-0284 project, and the GINOP-2.3.2-15-2016-00036 ("Development and application of multimodal optical nanoscopy methods in life and materials sciences") project.

## References

1. K. Ulbrich, K. Holá, V. Šubr, A. Bakandritsos, J. Tuček, and R. Zbořil, *Chem. Rev.* **116**, 5338 (2016).
2. S. Cozzens, R. Cortes, O. Soumonni, and T. Woodson, *J. Nanoparticle Res.* **15**, 2001 (2013).
3. K. T. Lau and D. Hui, *Compos. Part B Eng.* **33**, 263 (2002).
4. M. Heurlin, M. H. Magnusson, D. Lindgren, M. Ek, L. R. Wallenberg, K. Deppert, and L. Samuelson, *Nature* **492**, 90 (2012).
5. V. V. Pokropivny and V. V. Skorokhod, *Mater. Sci. Eng. C* **27**, 990 (2007).
6. C. Altavilla and E. Ciliberto, *Inorganic Nanoparticles: Synthesis, Applications, and Perspectives* (CRC Press, Boca Raton, 2011).
7. A. K. Singh, *Engineered Nanoparticles: Structure, Properties and Mechanisms of Toxicity* (Elsevier, San Diego, 2015).
8. M. Pumera, A. Ambrosi, and E. L. K. Chng, *Chem. Sci.* **3**, 3347 (2012).
9. G. Biskos, V. Vons, C. U. Yurteri, and A. Schmidt-Ott, *KONA Powder Part. J.* **26**, 13 (2008).
10. K. Wegner and S. E. Pratsinis, *Chem. Eng. Sci.* **58**, 4581 (2003).
11. B. O. Meuller, M. E. Messing, D. L. J. Engberg, A. M. Jansson, L. I. M. Johansson, S. M. Norlén, N. Tureson, and K. Deppert, *Aerosol Sci. Technol.* **46**, 1256 (2012).
12. M. H. Magnusson, K. Deppert, J. O. Malm, J. O. Bovin, and L. Samuelson, *Nanostructured Mater.* **12**, 45 (1999).
13. A. Schmidt-Ott, P. Schurtenberger, and H. C. Siegmann, *Phys. Rev. Lett.* **45**, 1284 (1980).
14. M. Kim, S. Ozone, T. Kim, H. Higashi, and T. Seto, *KONA Powder Part. J.* **34**, 80 (2017).
15. S. Schwyn, E. Garwin, and A. Schmidt-Ott, *J. Aerosol Sci.* **19**, 639 (1988).
16. <http://www.buonapart-e.eu/> (accessed: 29th of September 2017)
17. T. V. Pfeiffer, J. Feng, and A. Schmidt-Ott, *Adv. Powder Technol.* **25**, 56 (2014).
18. C. Helsper, W. Mölter, F. Löffler, C. Wadenpohl, S. Kaufmann, and G. Wenninger, *Atmos. Environ. Part A, Gen. Top.* **27**, 1271 (1993).

19. M. E. Messing, R. Westerström, B. O. Meuller, S. Blomberg, J. Gustafson, J. N. Andersen, E. Lundgren, R. van Rijn, O. Balmes, H. Bluhm, and K. Deppert, *J. Phys. Chem. C* **114**, 9257 (2010).
20. M. E. Messing, K. Hillerich, J. Bolinsson, K. Storm, J. Johansson, K. A. Dick, and K. Deppert, *Nano Res.* **3**, 506 (2010).
21. S. Kala, R. Theissmann, and F. E. Kruis, *J. Nanoparticle Res.* **15**, (2013).
22. T. Pfeiffer, P. Kedia, M. Messing, M. Valvo, and A. Schmidt-Ott, *Materials (Basel)*. **8**, 1027 (2015).
23. Y. Bae, P. V. Pikhitsa, H. Cho, and M. Choi, *Adv. Mater.* **29**, 1604159 (2017).
24. A. Muntean, M. Wagner, J. Meyer, and M. Seipenbusch, *J. Nanoparticle Res.* **18**, (2016).
25. J. H. Byeon, J. H. Park, K. Y. Yoon, and J. Hwang, *Nanoscale* **1**, 339 (2009).
26. L. Ludvigsson, B. O. Meuller, and M. E. Messing, *J. Phys. D. Appl. Phys.* **48**, 314012 (2015).
27. P. Karjalainen, L. Pirjola, J. Heikkil, T. Tzamkiozis, L. Ntziachristos, and J. Keskinen, *Atmos. Environ.* **97**, 262 (2014).
28. M. C. O. Chang, J. C. Chow, J. G. Watson, P. K. Hopke, S.-M. M. Yi, and G. C. England, *J. Air Waste Manage. Assoc.* **54**, 1494 (2004).
29. P. Kumar, L. Pirjola, M. Ketzler, and R. M. Harrison, *Atmos. Environ.* **67**, 252 (2013).
30. A. Hartland, J. R. Lead, V. Slaveykova, D. O'Carroll, and E. Valsami-Jones, *Nat. Educ. Knowl.* **4**, 7 (2013).
31. R. Nagarajan and T. A. Hatton, editors , *Nanoparticles: Synthesis, Stabilization, Passivation, and Functionalization* (American Chemical Society, Washington, 2008).
32. M. Faraday, *Philos. Trans. R. Soc. London* **147**, 145 (1857).
33. M. Brust, M. Walker, D. Bethell, D. J. Schiffrin, and R. Whyman, *J. Chem. Soc., Chem. Commun.* 801 (1994).
34. S. Agnihotri, S. Mukherji, and S. Mukherji, *RSC Adv.* **4**, 3974 (2014).
35. I. A. Rahman and V. Padavettan, *J. Nanomater.* **2012**, (2012).
36. W. Y. Teoh, *Materials (Basel)*. **6**, 3194 (2013).
37. S. E. Pratsinis and S. V. R. Mastrangelo, *Chem. Eng. Prog.* **85**, 62 (1989).

38. R. Koirala, S. E. Pratsinis, and A. Baiker, *Chem. Soc. Rev.* **45**, 3053 (2016).
39. S. Salameh, J. Gómez-Hernández, A. Goulas, H. Van Bui, and J. R. van Ommen, *Particuology* **30**, 15 (2017).
40. D. Vollath and K. E. Sickafus, *Nanostructured Mater.* **1**, 427 (1992).
41. L. Jiang, Q. Li, D. Zhu, M. Attoui, Z. Deng, J. Tang, and J. Jiang, *Aerosol Sci. Technol.* **6826**, 1 (2016).
42. N. Jidenko and J. P. Borra, *J. Aerosol Sci.* **35**, 29 (2004).
43. R. Ye, J.-G. Li, and T. Ishigaki, *Thin Solid Films* **515**, 4251 (2007).
44. W. Mahoney and R. P. Andres, *Mater. Sci. Eng. A* **204**, 160 (1995).
45. M. Stein, D. Kiesler, and F. E. Kruis, *J. Nanoparticle Res.* **15**, (2013).
46. N. S. Tabrizi, M. Ullmann, V. A. Vons, U. Lafont, and A. Schmidt-Ott, *J. Nanoparticle Res.* **11**, 315 (2009).
47. J. Feng, G. Biskos, and A. Schmidt-Ott, *Sci. Rep.* **5**, 15788 (2015).
48. Y. P. Raizer, *Gas Discharge Physics* (Springer-Verlag, Berlin Heidelberg, 1991).
49. A. A. Fridman and L. A. Kennedy, *Plasma Physics and Engineering* (CRC Press, Boca Raton, 2011).
50. E. M. Bazelian and Y. P. Raizer, *Spark Discharge* (CRC Press, Boca Raton, 1997).
51. A. Scheeline and D. M. Coleman, *Anal. Chem.* **59**, 1185A (1987).
52. M. Janda, V. Martišovits, and Z. Machala, *Plasma Sources Sci. Technol.* **20**, 35015 (2011).
53. P. W. J. M. Boumans, in *Anal. Emiss. Spectrosc.*, edited by E. L. Grove (Marcel Dekker, New York, 1972).
54. D. Z. Pai, D. A. Lacoste, and C. O. Laux, *Plasma Sources Sci. Technol.* **19**, 65015 (2010).
55. M. Janda, Z. Machala, A. Niklová, and V. Martišovits, *Plasma Sources Sci. Technol.* **21**, 45006 (2012).
56. N. Aleksandrov and E. Bazelyan, *Plasma Sources Sci. Technol.* **8**, 285 (1999).
57. J. P. Walters, *Appl. Spectrosc.* **23**, 317 (1969).
58. Á. Bardócz and F. Varsanyi, *Nature* **177**, 222 (1956).

59. J. P. Walters and W. S. Eaton, *Anal. Chem.* **55**, 57 (1983).
60. Á. Bardócz, *Elektrotechnika* 130 (1941).
61. J. P. Walters and H. V. Malmstadt, *Anal. Chem.* **37**, 1484 (1965).
62. A. Scheeline, J. A. Norris, J. C. Travis, J. R. Devoe, and J. P. Walters, *Spectrochim. Acta Part B At. Spectrosc.* **36**, 373 (1981).
63. S. Mandelstam, *Spectrochim. Acta* **297**, (1959).
64. C. A. Bye and A. Scheeline, *Appl. Spectrosc.* **47**, 2022 (1993).
65. Á. Bardócz and T. Vörös, *J. Quant. Spectrosc. Radiat. Transf.* **6**, 35 (1966).
66. R. Diermeier and H. Krempl, *Spectrochim. Acta Part B* **25**, 69 (1970).
67. C. A. Bye and A. Scheeline, *Spectrochim. Acta - Part B At. Spectrosc.* **488**, (1993).
68. A. Bye and A. Scheeline, *J. Quant. Spectrosc. Radiat. Transf.* **53**, 75 (1995).
69. Scott R. H., *Spectrochim. Acta Part B At. Spectrosc.* **33**, 123 (1978).
70. H. Burtscher and A. Schmidt-Ott, *Phys. Rev. Lett.* **48**, 1734 (1982).
71. N. S. Tabrizi, Q. Xu, N. M. Van Der Pers, and A. Schmidt-Ott, *J. Nanoparticle Res.* **12**, 247 (2010).
72. E. Hontañón, J. M. Palomares, M. Stein, X. Guo, R. Engeln, H. Nirschl, and F. E. Kruis, *J. Nanoparticle Res.* **15**, (2013).
73. M. Ullmann, S. Friedlander, and A. Schmidt-Ott, *J. Nanoparticle Res.* **4**, 499 (2002).
74. T. E. Itina and A. Voloshko, *Appl. Phys. B Lasers Opt.* **113**, 473 (2013).
75. J. Feng, X. Guo, N. Ramlawi, T. V. Pfeiffer, R. Geutjens, S. Basak, H. Nirschl, G. Biskos, H. W. Zandbergen, and A. Schmidt-Ott, *J. Mater. Chem. A* **4**, 11222 (2016).
76. A. Gutsch, H. Mühlenweg, and M. Krämer, *Small* **1**, 30 (2005).
77. J. Feng, L. Huang, L. Ludvigsson, M. E. Messing, A. Maisser, G. Biskos, and A. Schmidt-Ott, *J. Phys. Chem. C* **120**, 621 (2016).
78. J.-P. Borra, *J. Phys. D. Appl. Phys.* **39**, 19 (2006).
79. J. P. Borra, A. Goldman, M. Goldman, and D. Boulaud, *J. Aerosol Sci.* **29**, 661 (1998).
80. A. Voloshko, *Formation of Nanoparticles by Means of Spark Discharge at Atmospheric Pressure* (University Jean Monnet, 2016).

81. L. Jones, Br. J. Appl. Phys. **60**, (1950).
82. J. Sun, L. He, Y.-C. Lo, T. Xu, H. Bi, L. Sun, Z. Zhang, S. X. Mao, and J. Li, Nat. Mater. **13**, 1007 (2014).
83. A. Maisser, K. Barmounis, M. B. Attoui, G. Biskos, and A. Schmidt-Ott, Aerosol Sci. Technol. **49**, 886 (2015).
84. H. Horvath and M. Gangl, J. Aerosol Sci. **34**, 1581 (2003).
85. N. S. Tabrizi, Q. Xu, N. M. Van Der Pers, U. Lafont, and A. Schmidt-Ott, J. Nanoparticle Res. **11**, 1209 (2009).
86. A. E. Berkowitz and J. L. Walter, J. Mater. Res. **2**, 277 (1987).
87. C. R. Svensson, L. Ludvigsson, B. O. Meuller, M. L. Eggersdorfer, K. Deppert, M. Bohgard, J. H. Pagels, M. E. Messing, and J. Rissler, J. Aerosol Sci. **87**, 38 (2015).
88. S. R. Boddu, V. R. Gutti, T. K. Ghosh, R. V. Tompson, and S. K. Loyalka, J. Nanoparticle Res. **13**, 6591 (2011).
89. J. H. Byeon, J. H. Park, and J. Hwang, J. Aerosol Sci. **39**, 888 (2008).
90. W. C. Hinds, *Aerosol Technology* (John Wiley & Sons, New York, 1999).
91. K. Han, W. Kim, J. Yu, J. Lee, H. Lee, C. Gyu Woo, and M. Choi, J. Aerosol Sci. **52**, 80 (2012).
92. S. Chae, D. Lee, M.-C. Kim, D. S. Kim, and M. Choi, Aerosol Sci. Technol. **49**, 463 (2015).
93. M. E. Messing, J. Green Eng. **5**, 83 (2016).
94. M. N. A. Karlsson, K. Deppert, L. S. Karlsson, M. H. Magnusson, J. O. Malm, and N. S. Srinivasan, J. Nanoparticle Res. **7**, 43 (2005).
95. S. Jang, J. Yoon, K. Ha, M.-C. Kim, D. H. Kim, S. M. Kim, S. M. Kang, S. J. Park, H. S. Jung, and M. Choi, Nano Energy **22**, 499 (2016).
96. T. V Pfeiffer, J. Ortiz-Gonzalez, R. Santbergen, H. Tan, A. Schmidt Ott, M. Zeman, and A. H. M. Smets, Energy Procedia **60**, 3 (2014).
97. M. H. Magnusson, B. J. Ohlsson, M. T. Björk, K. A. Dick, M. T. Borgström, K. Deppert, and L. Samuelson, Front. Phys. **9**, 398 (2014).
98. C. Roth, G. A. Ferron, E. Karg, B. Lentner, G. Schumann, S. Takenaka, and J. Heyder, Aerosol Sci. Technol. **38**, 228 (2004).
99. N. A. Isaac, M. Valenti, A. Schmidt-Ott, and G. Biskos, ACS Appl. Mater. Interfaces **8**,

3933 (2016).

100. A. A. Efimov, I. A. Volkov, V. V. Ivanov, A. A. Vasiliev, A. E. Varfolomeev, A. V. Pislyakov, A. S. Lagutin, and T. Maeder, *Procedia Eng.* **168**, 1036 (2016).
101. J. Feng, E. Hontañón, M. Blanes, J. Meyer, X. Guo, L. Santos, L. Paltrinieri, N. Ramlawi, L. C. P. M. de Smet, H. Nirschl, F. E. Kruis, A. Schmidt-Ott, and G. Biskos, *ACS Appl. Mater. Interfaces* **8**, 14756 (2016).
102. S. Blomberg, J. Gustafson, N. M. Martin, M. E. Messing, K. Deppert, Z. Liu, R. Chang, V. R. Fernandes, A. Borg, H. Grönbeck, and E. Lundgren, *Surf. Sci.* **616**, 186 (2013).
103. V. A. Vons, H. Leegwater, W. J. Legerstee, S. W. H. Eijt, and A. Schmidt-Ott, *Int. J. Hydrogen Energy* **35**, 5479 (2010).
104. V. A. Vons, L. C. P. M. De Smet, D. Munao, A. Evirgen, E. M. Kelder, and A. Schmidt-Ott, *J. Nanoparticle Res.* **13**, 4867 (2011).
105. D. Baumgardner, O. Popovicheva, J. Allan, V. Bernardoni, J. Cao, F. Cavalli, J. Cozic, E. Diapouli, K. Eleftheriadis, and P. J. Genberg, *Atmos. Meas. Tech. Eur. Geosci. Union* **5**, 1869 (2012).
106. C.-S. Wong and R. Mongkolkeha, *Elements of Plasma Technology* (Springer, Singapore, 2016).
107. T. G. Engel, A. L. Donaldson, and M. Kristiansen, *IEEE Trans. Plasma Sci.* **17**, 323 (1989).
108. W. D. Greason, Z. Kucerovsky, S. Bulach, and M. W. Flatley, *IEEE Trans. Ind. Appl.* **33**, 1519 (1997).
109. P. Persephonis, K. Vlachos, C. Georgiades, and J. Parthenios, *J. Appl. Phys.* **71**, 4755 (1992).
110. D. A. Myl'nikov, V. V. Ivanov, A. A. Efimov, and I. V. Beketov, *Meas. Tech.* **58**, 1367 (2016).
111. D. Pommerenke, *J. Electrostat.* **36**, 31 (1995).
112. F. Paschen, *Ann. Phys.* **273**, 69 (1889).
113. F. W. Crawford and H. Edels, *Proc. IEE Part A Power Eng.* **107**, 202 (1960).
114. Z. Machala, I. Jedlovsky, and V. Martisovits, *IEEE Trans. Plasma Sci.* **36**, 918 (2008).
115. S. Nijdam, C. G. C. Geurts, E. M. van Veldhuizen, and U. Ebert, *J. Phys. D. Appl. Phys.* **42**, 45201 (2009).

116. B. Du, S. Mohr, D. Luggenhölscher, and U. Czarnetzki, *J. Phys. D. Appl. Phys.* **44**, 125204 (2011).
117. M. Ramli and K. Wagatsuma, *ISIJ Int.* **50**, 864 (2010).
118. A. Hamdan, I. Marinov, A. Rousseau, and T. Belmonte, *J. Phys. D. Appl. Phys.* **47**, 55203 (2014).
119. P. Krehl and S. Engemann, *Shock Waves* **5**, 1 (1995).
120. S. I. Braginski, *J. Exptl. Theor. Phys.* **34**, 1548 (1958).
121. R. Reinmann and M. Akram, *J. Phys. D. Appl. Phys.* **30**, 1125 (1997).
122. K. H. Becker, K. H. Schoenbach, and J. G. Eden, *J. Phys. D Appl. Phys* **39**, 55 (2006).
123. D. Mariotti and R. M. Sankaran, *J. Phys. D. Appl. Phys.* **43**, 323001 (2010).
124. H.-J. Kunze, *Introduction to Plasma Spectroscopy* (Springer, Berlin, Heidelberg, 2009).
125. L. Blitzer, **41**, 440 (1951).
126. C. Aragón and J. A. Aguilera, *Spectrochim. Acta - Part B At. Spectrosc.* **63**, 893 (2008).
127. H. R. Griem, *Phys. Rev.* **128**, 997 (1962).
128. [https://physics.nist.gov/PhysRefData/ASD/lines\\_form.html](https://physics.nist.gov/PhysRefData/ASD/lines_form.html), (Accessed 28. 09. 2017).
129. N. Konjević, *Phys. Rep.* **316**, 339 (1999).
130. J. A. Aparicio, M. A. Gigosos, V. R. Gonzalez, C. Perez, M. I. de la Rosa, S. Mar, and U. de V. V. S. Departamento de Optica, *J. Phys. B At. Mol. Opt. Phys.* **31**, 1029 (1998).
131. B. Bachmann, R. Kozakov, G. Gött, K. Ekkert, J.-P. Bachmann, J.-L. Marques, H. Schöpp, D. Uhrlandt, and J. Schein, *J. Phys. D. Appl. Phys.* **46**, 125203 (2013).
132. J. E. Daalder, *Physica* **104**, 91 (1981).
133. B. Jüttner, *IEEE Trans. Plasma Sci.* **15**, 474 (1987).
134. A. Lasagni, F. Soldera, and F. Mücklich, *Zeitschrift Für Met.* **95**, 1 (2004).
135. B. Jüttner, *Beiträge Aus Der Plasmaphys.* **19**, 25 (1979).
136. A. Anders, *Cathodic Arcs* (Springer, New York, 2008).
137. A. E. Guile and B. Jüttner, *IEEE Trans. Plasma Sci.* **8**, 259 (1980).

138. R. L. Boxman, D. M. Sanders, and P. J. Martin, editors , *Handbook of Vacuum Arc Science and Technology* (Noyes Publications, Park Ridge, New Jersey, 1995).
139. W. Brewer and J. P. Walters, *Anal. Chem.* **41**, 1980 (1969).
140. J. D. Cobine and C. J. Gallagher, *Phys. Rev.* **74**, 1524 (1948).
141. B. D. Bleiner and A. Bogaerts, *Spectrochim. Acta - Part B* **61**, 421 (2006).
142. J. M. Fishburn, M. J. Withford, D. W. Coutts, and J. A. Piper, *Appl. Surf. Sci.* **252**, 5182 (2006).
143. M. C. Bartelt and J. W. Evans, *Surf. Sci.* **314**, (1994).
144. Y. Astrov, E. Ammelt, S. Teperick, and H.-G. Purwins, *Phys. Lett. A* **211**, 184 (1996).
145. E. L. Gurevich, A. L. Zanin, A. S. Moskalenko, and H.-G. Purwins, *Phys. Rev. Lett.* **91**, 154501 (2003).
146. J. P. Trelles, *Plasma Sources Sci. Technol.* **22**, 25017 (2013).
147. E. Hontañón, J. M. Palomares, X. Guo, R. Engeln, H. Nirschl, and F. E. Kruis, *J. Phys. D. Appl. Phys.* **47**, 415201 (2014).
148. M. C. Cross and P. C. Hohenberg, *Rev. Mod. Phys.* **65**, 851 (1993).
149. A. M. Turing, *Philos. Trans. R. Soc. B Biol. Sci.* **237**, 37 (1952).
150. P. G. C. Almeida and M. S. Benilov, *Phys. Plasmas* **20**, 101613 (2013).
151. K. G. Müller, *Phys. Rev. A* **37**, 4836 (1988).
152. J. P. Trelles, *Plasma Sources Sci. Technol.* **23**, 54002 (2014).
153. E. Ammelt, Y. A. Astrov, and H.-G. Purwins, *Phys. Rev. E* **55**, 6731 (1997).
154. M. S. Benilov, *Plasma Sources Sci. Technol.* **23**, 54019 (2014).
155. L. Wang, X. Huang, and S. Jia, **42**, 1393 (2014).
156. V. A. Nemchinsky and M. S. Showalter, *J. Phys. D. Appl. Phys.* **36**, 704 (2003).
157. V. F. Puchkarev and S. M. Chesnokov, *J. Phys. D. Appl. Phys.* **25**, 1760 (1992).
158. J. Zeleny, *Phys. Rev.* **34**, 310 (1929).
159. R. C. Flagan, *Aerosol Sci. Technol.* **28**, 301 (1998).
160. W. A. Hoppel, *J. Aerosol Sci.* **9**, 41 (1978).
161. J. K. Agarwal and G. J. Sem, *J. Aerosol Sci.* **11**, 343 (1980).

162. A. L. Donaldson, M. O. Hagler, M. Kristiansen, G. Jackson, and L. Hatfield, *IEEE Trans. Plasma Sci.* **12**, 28 (1984).
163. E. Hantzsche, *IEEE Trans. Plasma Sci.* **31**, 799 (2003).
164. N. T. Jenkins and T. W. Eagar, *JOM* **55**, 44 (2003).
165. H. Martinen and H. Tholl, *Z. Naturforschdi* **25**, 430 (1970).